

© 2012 Nghia Quang Nguyen

OBJECTIVE ASSESSMENT OF SONOGRAPHIC QUALITY FOR BREAST CANCER  
IMAGING

BY

NGHIA QUANG NGUYEN

DISSERTATION

Submitted in partial fulfillment of the requirements  
for the degree of Doctor of Philosophy in Electrical and Computer Engineering  
in the Graduate College of the  
University of Illinois at Urbana-Champaign, 2012

Urbana, Illinois

Doctoral Committee:

Professor Michael F. Insana, Chair  
Professor Zhi-Pei Liang  
Associate Professor Paul S. Carney  
Associate Professor Mark A. Hasegawa-Johnson  
Doctor Craig K. Abbey, University of California, Santa Barbara

# ABSTRACT

The purpose of any medical imaging device is to acquire timely diagnostic information in a manner that poses the lowest cost and risk to patients and society. Ideally, medical imaging systems are designed by maximizing the benefit-to-cost ratio from a set of laboratory measurements that define “image quality” in the sense that they predict diagnostic performance in clinical applications. For ionizing radiation modalities, where risks can be high, the science of image quality has been well developed since the early days in the 1970s, and these principles are now integrated throughout industry and the practice of medicine. In medical sonography, however, these methods are not as advanced for at least two reasons.

One reason is that ultrasound is a very low-risk and low unit-cost modality. Because there is no risk caused by ionizing radiation in ultrasound imaging, the motivation for building a regulatory system to integrate academic developments into industry has been low. Yet, the use of ultrasonic imaging in medical practice worldwide is second only to X-ray imaging in terms of unit sales and exams per year. Task-based optimization of any highly used technology like sonography can have a major positive effect on society through healthcare cost reduction. The second reason, found in my dissertation, is that the mechanisms of the sound-tissue interactions generating object contrast in sonography are fundamentally different than those of photon-based imaging. These differences pose profound challenges on how laboratory measurements of image quality should be applied in system design and evaluation, and have prevented the image science of medical sonography from being advanced as quickly as other modalities with respect to ideal observer analysis.

The unique contributions of my dissertation research are to develop ideal observer analysis for B-mode sonography as a design and evaluation tool. Specifically, our team developed methods for expressing common diagnostic features of tumors as statistical equations so that we could compute the test statistic of the ideal discriminator from log-likelihood ratios that are unique to each clinical exam. We then obtained mathematical approximations to the exact test statistic expressions that could be implemented in signal processing algorithms and applied to the echo signals of images. This approach was shown

to improve the information content of the data as well as human observer performance.

My contributions to the team effort were to develop and test (a) iterative adaptive filters that are applied to beamformed echo signals to add task-specific information into the image formation process; (b) several methods for measuring the spatiotemporal impulse response of commercial systems; (c) a definition for visual task information in sonography; (d) a closed-form expression that directly links task information to image quality features, which forms a basis for image quality assessments and design specifications; and (e) concepts that unite alternative approaches to array beamforming under a single analytical framework. This dissertation and associated peer-reviewed publications have helped to define the image science of medical sonography. Our applications have thus far focused on benign-malignant discrimination of breast lesions, but we believe the methods described within have much broader potential.

*To*  
*Thanh Vân, Khuê Giang,*  
*and my parents*

# ACKNOWLEDGMENTS

I would first like thank my advisor, Professor Michael F. Insana, for patiently providing the vision, encouragement, and advice necessary for me to complete my dissertation. He has enlightened me by his wide knowledge and deep intuitions about sonographic quality, and given me great freedom to pursue independent work. His support from the initial to final levels enabled me to develop an understanding of the subject. Second, I want to express my appreciation and gratitude to Dr. Craig K. Abbey of the University of California, Santa Barbara, for his creativity, contribution, and mentoring related to many aspects of the work. Discussions with him on the research have provided me valuable knowledge and enjoyable experiences. Special thanks go to members of my Ph.D. committee, Professors Zhi-Pei Liang, Paul Scott Carney, and Mark A. Hasegawa-Johnson for their service, guidance, and helpful suggestions throughout the whole extent of my dissertation. And I thank to Jamie Hutchinson and Thomas N. McGeary at ECE Publications Office for their invaluable help on tracking the writing of this dissertation.

I am also grateful to people of Ultrasound Imaging and Bioacoustics Research Labs for their friendship and support in completing this work. I would like to thank all of my friends at the University of Illinois, for sharing their glory and sadness, enjoyable moments, and paper deadlines during my stay at Urbana-Champaign, making it the most memorable time of my life.

The dissertation, as well as most of my accomplishments, would have not been possible without support from my family. My deepest gratitude goes to my parents for their endless love and encouragement, which allow me to follow my heart and pursue my goals. I would like to thank my beloved wife, Vân. Her unconditional love and sacrifices have been instrumental in achieving my goals, especially for this work. I also thank my beautiful daughter, Giang, for being the inspiration to complete the dissertation. Day-to-day learning to be her father and to receive her love makes me a better person. The dissertation is dedicated to all of them.

This research is supported by the National Institutes of Health (NIH) under award No. CA118294.

# TABLE OF CONTENTS

LIST OF ABBREVIATIONS . . . . .	viii
CHAPTER 1 INTRODUCTION . . . . .	1
1.1 Breast cancer and diagnosis . . . . .	1
1.2 Motivation . . . . .	2
1.3 Objective assessment of image quality . . . . .	3
1.4 OAIQ for ultrasound imaging modality . . . . .	4
1.5 Dissertation goals and proposal research . . . . .	6
1.6 Dissertation outline . . . . .	7
CHAPTER 2 BACKGROUND: IMAGE MODELING AND PERFORMANCE ASSESSMENTS . . . . .	10
2.1 Introduction . . . . .	10
2.2 Scattering object . . . . .	12
2.3 Signal modeling . . . . .	18
2.4 The ideal observer . . . . .	20
2.5 Human observer . . . . .	26
2.6 Wiener filter as approximation to ideal strategy . . . . .	27
2.7 Summary . . . . .	28
CHAPTER 3 OBJECTIVE ASSESSMENT OF IMAGE QUALITY IN SONOG- RAPHY . . . . .	29
3.1 Introduction . . . . .	29
3.2 Task performance and information . . . . .	36
3.3 Acquisition information spectrum . . . . .	42
3.4 Summary and discussion . . . . .	48
CHAPTER 4 POST-PROCESSING . . . . .	50
4.1 Introduction . . . . .	50
4.2 Iterative Wiener filter (IWF) . . . . .	52
4.3 Observer efficiency . . . . .	57
4.4 Experimental implementation . . . . .	63
4.5 Discussion . . . . .	65
CHAPTER 5 BEAMFORMING . . . . .	68
5.1 Introduction . . . . .	68

5.2	Ideal observer approach to beamformers . . . . .	70
5.3	Connections to other studies . . . . .	74
5.4	Simulation . . . . .	77
5.5	Discussion . . . . .	82
CHAPTER 6 MEASUREMENTS OF THE SPATIOTEMPORAL PULSE-ECHO		
	IMPULSE RESPONSE . . . . .	84
6.1	Introduction . . . . .	84
6.2	Scattering spheres . . . . .	85
6.3	Reconstruction from projections of rotating line . . . . .	88
6.4	Discussion . . . . .	102
CHAPTER 7 CONCLUSIONS . . . . . 104		
7.1	Summary . . . . .	104
7.2	Future work . . . . .	106
APPENDIX A RELATION OF $\text{SNR}_f$ TO THE IDEAL OBSERVER AUC . . . . 110		
APPENDIX B SUPPORTING MATERIAL FOR CHAPTER 3 . . . . . 112		
B.1	Proof of (3.28) . . . . .	112
B.2	Proof of (3.30) . . . . .	113
APPENDIX C WIENER FILTER FOR LINEAR SHIFT VARIANCE PULSE-ECHO IMPULSE RESPONSE . . . . . 117		
APPENDIX D SUPPORTING MATERIAL FOR CHAPTER 5 . . . . . 120		
D.1	Ideal observer analysis for ill-conditioned $\mathbf{K}_n$ . . . . .	120
D.2	Minimum variance distortionless response (MVDR) . . . . .	121
D.3	Proof of (5.23) . . . . .	122
APPENDIX E RECONSTRUCTION USING THE SVD METHOD . . . . . 123		
APPENDIX F PEER-REVIEWED PUBLICATIONS AND CONTRIBUTED TALKS . . . . . 126		
F.1	Book chapter . . . . .	126
F.2	Journal papers . . . . .	126
F.3	Conference proceedings . . . . .	127
F.4	Presentations . . . . .	128
REFERENCES . . . . . 129		

# LIST OF ABBREVIATIONS

2AFC	two alternative force choice
AIS	acquisition information spectrum
ART	algebraic reconstruction technique
AUC	area under ROC
BKE	background known exactly
BKS	background known statistically
BM	basement membrane
CT	computerized tomography
DC	ductal carcinoma
DQE	detective quantum efficiency
ECM	extracellular matrix
eSNR	echo signal to noise ratio
GNEQ	generalized noise equivalent quanta
IDC	invasive ductal carcinoma
ILC	invasive lobular carcinoma
IO	ideal observer
IWF	iterative Wiener filter
IWFB-mode	iterative Wiener filtered B-mode
LC	lobular carcinoma
LCMV	linear constrained minimum variance
LCIS	lobular carcinoma in situ

LE	luminal epithelium
LSF	line spread function
LSIV	linear shift invariant
MAP	maximum a posteriori
ME	myoepithelial
MF	matched filter
MMSE	minimum mean squared error
MRF	Markov random field
MVN	multivariate normal
MV	minimum variance
MVDR	minimum variance distortionless response
NEQ	noise equivalent quanta
OAIQ	objective assessment of image quality
pdf	probability density function
PSF	point spread function
RF	radio frequency
RHS	right hand side
ROC	receiver operating characteristic
SKE	signal known exactly
SNR	signal-to-noise ratio
SSF	spatial sensitivity function
SVD	singular value decomposition
SW	Smith-Wagner
WF	Wiener filter
WFB-mode	Wiener filtered B-mode
XRP	X-ray photography

# CHAPTER 1

## INTRODUCTION

### 1.1 Breast cancer and diagnosis

Breast cancer affects one in eight women during their lives, making it the most commonly diagnosed cancer and the second most common cause of cancer death after lung cancer in women. In the United States, it is estimated that 209,060 new cases of breast cancer (207,090 women, 1970 men) would be diagnosed in 2010, and 40,230 breast cancer deaths (39,840 women, 390 men) were expected [1]. Much research effort has been focusing on understanding the basic mechanism of the disease, and developing methods to detect it early as well as treat it effectively. Cancer is a group of many related diseases, caused by the uncontrollable division of transformed cells. They form a malignant tumor that can break through basement membranes to invade locally, and gradually spread to all parts of the body through the bloodstream or the lymph system. The growth of a cancerous tumor can be divided into several stages,

Stage 0	Non-invasive
Stage I	Up to 2 cm in size
Stage II	Spreads to lymph nodes
Stage III	Larger than 5 cm in size and locally invasive
Stage IV	Spreads to other parts of the body

Early detection and diagnosis of breast cancer are crucial to the successful treatment and cure. If a tumor is detected when it is less than 1 cm, the patient has 85% chance of cure as opposed to 10% if detected later. There are several methods for breast cancer detection. The simplest method is palpation. Typically, malignant lesions are stiffer than surrounding tissues, so one can feel by pressing finger tips into the surface skin of the patient. However, palpation cannot detect small and deep tumors. In such cases, an imaging technique is usually required. Once a breast abnormality is detected, a biopsy may be done. This procedure removes a tissue sample for examination under a microscope.

It is the standard method in present-day practice to obtain a true diagnosis [2].

X-ray mammography is the most effective scanning tool for early detection of breast cancer. Early detection and treatment have been shown to reduce the patient mortality by 30% [3]. Mammograms are 2-D projections of the breast created by ionizing radiation. They offer 50-100  $\mu\text{m}$  resolution for visualizing suspicious masses and microcalcifications. Unfortunately, the procedure is uncomfortable and even painful to many women. The ionizing radiation exposures also damage the breast tissues and these damaging effects accumulate inside the body. Therefore, other imaging techniques have been sought as an alternative modality for breast cancer diagnosis.

Recent studies have demonstrated the effectiveness of ultrasound imaging in detecting breast cancer [4–6]. Although it was explored as a breast imaging technique as early as the 1960s, its true value was not recognized until the 1980s when real-time B-scan transducers with high frequencies and electronic focusing were introduced. Since that time, breast ultrasound is routinely used to determine if a mammographic abnormality or clinically palpable mass is cystic or solid [7]. Compared to mammography, ultrasound is safer, cheaper and more comfortable to women. It offers higher object contrast for some lesion types, but has lower spatial resolution. Therefore, ultrasound is unable to image small structures such as microcalcifications, tiny calcium deposits which are often the first indications of breast cancer. Conventional ultrasound imaging is now routinely applied in clinical settings as an adjunct to mammography and physical examination.

## 1.2 Motivation

The development of computational technologies allows us to implement some complex signal processing and beamforming strategies on ultrasound instruments for improving their image resolutions. Their goal is to focus the transducer beam uniformly throughout the field of view. However, each technique is a trade-off among echo signal-to-noise ratio (eSNR), safety, cost, and contrast, spatial, and temporal resolutions. Each affects diagnostic performance for specific clinical tasks. Diagnostic performance is evaluated, often subjectively, by experts using the systems in medical practice. Yet, there is no clear and direct connection between engineering considerations and clinical diagnosis. Furthermore, there now exists greater flexibility in the ability to reconfigure system platforms for patient-specific exams, particularly in high-end commercial instruments. Such adaptability has already significantly increased the performance-to-cost ratio for general sonography over the past decade. In light of the increased capabilities of modern ul-

trasonic imaging systems to adapt to different scanning settings, it becomes important to optimize sonographic imaging designs to most effectively detect and identify signs of breast cancer.

A brute-force approach to optimization is simply to run clinical studies spanning the range of possible pulse-acquisition settings, signal-processing algorithms, and image display settings. To be most effective, these studies would need to consider different lesion and background characteristics such as lesion depth, degree of invasion, and background echo texture. However, clinical studies of such magnitude are essentially infeasible because of time and expense considerations. As a result, a rational optimization approach is favored, in which theoretical analysis and models of visual detection are used to identify a few promising configurations for investigation in clinical studies. The goal of this dissertation is to develop an analytical framework where the engineering properties listed above are related mathematically to the diagnostic performance, measured in a manner that generates metrics equivalent to receiver-operating characteristic (ROC) analysis, the industry's gold standard for evaluating imaging systems [8].

### 1.3 Objective assessment of image quality

Image quality, for scientific and medical purposes, must be defined in terms of how well desired information can be extracted from the image. The new definition leads to objective assessment of image quality (OAIQ) or a task-based approach for designing the imaging system. In this approach, the system is evaluated on the basis of observers' performance on a specific task. The approach is an application of statistical detection theory first used in radar imaging during World War II, with scientific background provided decades earlier by Hotelling, Thurstone, and Neyman and Pearson [9]. It has subsequently been applied to the evaluation of medical imaging systems by Swets and Pickett [10, 11], Wagner and Brown [12], Barrett and Myers [8], and many others.

Wagner was the first proposing the use of visual task information to evaluate the quality of a system or an image reconstruction. He described imaging systems as devices that transfer task information from the objects being examined to observers [13]. The image formation then was divided into two stages, the initial acquisition (detector) and the display. Acquisition is where information radiated or scattered from the object is recorded. The display stage involves configuration as an image, including any reconstruction or image processing algorithm, scan conversion, or gray-scale mapping for consumption by an observer. The observer can be an expert human or an algorithm evaluating criteria

based on decision theory with the performance evaluated through the ROC analysis [14]. Prominent among the latter is the *ideal observer* (IO) that adopts the log-likelihood ratio as the test statistic and combines all available information to make the best decision [8]. The ideal observer performance, therefore, is optimal and serves as a measure of the task-relevant information content of the imaging data.

In 1985, Wagner and Brown published their landmark paper on unified SNR theory [12]. They first introduced the ideal observer signal-to-noise ratio,  $\text{SNR}_I$ , as a metric to quantify the IO performance. Under the normal distribution for the test statistic,  $\text{SNR}_I$  is related to the ideal observer performance, measured by using the area under the ROC curve (AUC), through the error function [15]. In the paper, Wagner and Brown factorized  $\text{SNR}_I$  into task information at the input and the noise equivalent quanta (NEQ) of the imaging system over the spatial frequency domain. This neat factorization shows analytically that the standard performance of an imaging system depends on the task and a physical parameter of the system. NEQ is the product of the three Fourier descriptions, specifying the image contrast, spatial resolution, and noise power spectrum [12]. NEQ was first defined by Shaw as the minimum number of X-ray quanta required to produce an image at a given SNR [16]. The more efficient the system at “transferring” quanta, the closer the NEQ is to the actual number of quanta used to make the image. But in the IO approach, NEQ becomes the number of quanta or photons the image is worth to the IO who makes perfect use of each quantum. NEQ is also represented to the contribution of the system to the ideal performance. Imaging systems therefore could be compared by just simply comparing their NEQs. In fact, the NEQ curve has been used regularly by companies seeking approval from the Food and Drug Administration for their products. Later, Barrett et al. extended the concept of NEQ to generalized noise equivalent quanta (GNEQ) for the problem of signals known exactly but the background known statistically – the SKE/BKS paradigm [17]. The approach has been also generalized to include shift-varying systems, random signals and backgrounds, and non-stationary noise [18]. The SNR analysis and those extensions have greatly facilitated rigorous performance predictions for imaging systems, but primarily for photon-based modalities. It is limited to sonographic systems with much of work still remaining for general treatment [12].

## 1.4 OAIQ for ultrasound imaging modality

Sonographic systems include a demodulation in the display stage. This nonlinear process makes the statistical analysis become complicated. The IO approach was first applied to

sonography by Wagner and Smith [19, 20] in their award-winning papers of 1983. They derived the IO viewing B-mode images for the binary task of low-contrast lesion detection. To obtain the closed-form expression for the IO, however, Wagner and Smith made numerous limiting assumptions. Among them, they assumed no measurement noise, only large-area low-contrast lesions may be present, the system provided shift-invariant focal-zone impulse responses, and speckle spots rather than pixels determine statistical properties of image data. They realized that diagnostic information in a sonogram is contained in speckles, and proposed acoustic speckle spot density in the spatial domain as the analogy to radiographic photon density in the frequency domain. This is a reasonable assumption for the special case of non-diffracting Gabor pulses that generate fully developed speckle. Speckle density is related to information density since it is the number of independent signal samples presented to observers on which they base decisions. Outside the focal zone, however, speckle patterns can be correlated over very long ranges. In any case, independent sample density may be estimated from signal coherence lengths [21]. Their work provided design criteria that guided subsequent work in speckle reduction [22], beamformation [21], post-processing [23], and transducer selection [24]. However, the stringent assumptions listed above needed to achieve the closed-form expression made the analysis far from representing realistic clinical imaging conditions.

Modern ultrasound systems provide users an option for recording digitized radio-frequency (RF) or in-phase-quadrature (IQ) signals [25], allowing us to shift the framework from B-mode images to RF signals. In this domain, the signals are generated by known and linear processes that we can model for the IO analysis. Deriving the IO on RF signals avoids these limiting assumptions made when analyzing task information with B-mode images. The IO performance measures information transfer at the acquisition stage of recording; that is, up to the point of demodulating beamformed RF signals before scan conversion. Combining IO performance with measurements using the Smith-Wagner and human observers, it is possible to follow the flow of task information from the patient through each stage of image formation ultimately to the diagnostician. Extending the IO analysis on the RF domain, however, introduces new challenges. There is a fundamental difference in data statistics between the two imaging modalities of radiography and sonography. In radiography, the image was generated from medium attenuation of the incident photon field, which modifies the receive-signal amplitude. Poisson photon statistics are accurately modeled at the output elements of a detector as multivariate normal (MVN) when photon counts are sufficiently large. The imaging contrast created from the photon absorption process is encoded in nonstationary pixel means. Variations in the mean object function linearly map into variations in the mean image data, and so

the test statistic of the ideal observer is a linear function of the image data. Since the data has MVN distribution, the test statistic is normally distributed as well. Therefore it is common to conduct an observer study, compute the area under the ROC curve (AUC), and connect the AUC to  $\text{SNR}_I$ , which can be related to instrumentation properties. In sonography, however, breast lesion features were introduced into tissue scattering functions by spatially modulating the variance of acoustic impedance. Thus the diagnostic task is specified entirely by the object covariance matrix, which leads to the quadratic form of the IO. Although the distributions of the imaging data are still modeled by the MVN densities, the normal distribution, or *normality condition*, for the IO test statistic may be lost under the nonlinear form. The normality condition is also hard to be verified since the test statistic involves inverses of high dimensional covariance matrices. Computing the IO test statistic also introduces the practical challenge to the framework.

## 1.5 Dissertation goals and proposal research

The limitations stated above provide opportunities for further engineering developments. Over the last five years, I have conducted several studies for my dissertation, which include implementing an analytical framework for system designs using the IO approach, exploring the IO and translating its equations into optimal signal processing strategies to improve the sonogram quality. The specific aims of the dissertation are listed below.

1. **Objective assessment of sonographic quality.** Without the normality condition for the ideal observer test statistic, relation between  $\text{SNR}_I$  and the ideal performance is no longer as rigorous as in photon-based imaging. The interpretation of engineering metrics in terms of observer performance becomes uncertain. Thus, we need a new interpretation for the ideal performance, measured through AUC, for our sonographic tasks. The new interpretation will allow us to follow Wagner and Brown's framework and establish an ideal observer analysis for medical sonography on par with radiographic modalities.
2. **Post-filtering.** We have proposed the use of a power series expansion to meet the computational challenge in calculating the test statistic in the initial study of the research [26]. The first-order approximation of the power series reveals a Wiener filtering operator on the RF domain before taking the envelope image. Through psychophysical studies, the filter was found to help human observers improve their performance in detecting and discriminating four of five typical features in breast cancer

diagnosis using sonograms, but to reduce the performance on anechoic/hypoechoic discrimination. The reduction has guided subsequent exploration of the ideal observer. A better approximation is needed to include a greater range of practical conditions. The new filter, translated from the new approximation of the IO, may adaptively tune to the echo statistics wherever there is diagnostic information. The goal of these filters is to maximize the efficiency at which the human observer can access the diagnostic information.

3. **Beamforming.** Several beamformers have been applied in breast sonography, and they show improvements in image contrast and resolution on some demonstration images. However, a question of how diagnostic performance is improved through the implementation of the beamformers remains unanswered. Therefore, we extend the IO analysis to develop a framework for finding the optimal beamforming strategy on each specific task. In the framework, beamformers are interpreted from approximations of the ideal strategy. They are evaluated based on the conditions for which those approximations hold.
4. **Measurements/reconstructions of spatiotemporal impulse response.** This study comes from a practical challenge when implementing beamformers and filters derived from the ideal observer framework on experimental data. We found the pulse-echo spatiotemporal impulse response of the ultrasonic system plays a central role in modeling the RF signals, deriving the IO, and developing data processing strategies suggested by the ideal observer. It is crucial to accurately estimate the pulse-echo impulse response of a commercial system; otherwise, the results obtained from the framework may not be achieved on experimental data. Therefore, accurate measurements of the pulse-echo impulse response function are pursued as a part of this dissertation work.

## 1.6 Dissertation outline

The rest of this dissertation is organized as follows. Chapter 2 presents background for the research. The sonographic tasks used in the studies have been identified by isolating five typical features that physicians look for in breast cancer diagnosis using sonograms. Signals of the imaging formation inside the ultrasonic system, from the object being scanned to the final B-mode images for observation, are analyzed and modeled. At the end of the system, the image quality is evaluated through performance of some observers,

including both human and computational models. These observers are described along with the metrics quantifying their performance.

Chapter 3 establishes the rigorous framework for evaluating sonographic quality that builds on the radiographic tradition. The Kullback-Leibler divergence, a fundamental metric to quantify the discrimination information in information theory, is introduced to measure task information on the RF data. Without using the normality condition, the divergence is related to the area between the two curves representing probabilities of detection and false-alarm as functions of the threshold. It is analogous to the area between detection and false-alarm curves under the ROC curve, which also specifies the discrimination information brought by the data but in a different coordinate system. Thus the ideal performance can be interpreted as a description of the discrimination information but measured through concepts of Bayesian statistical decision theory. The new interpretation allows us to follow an example of Wagner and Brown's SNR analysis to derive an NEQ-like term for sonography. We named it the Acquisition Information Spectrum (AIS). The term quantifies the efficiency of a sonographic system for transferring diagnostic information from patients to recorded RF data [27, 28].

Chapter 4 extends the IO exploration in [26] to find a better strategy to process data before the demodulation. The new exploration leads us to an adaptive filter that better matches the optimal processing of the ideal observer. A binary segmentation is used to modify the Wiener filter to local statistics. Observer performance is enhanced for all five of the diagnostic features examined when compared with the DS beamformer but with additional computational overhead. The concepts are demonstrated on a commercial system by imaging a tissue-mimicking phantom where results include a realistic, shift-variant model for the system impulse response [29, 30].

Chapter 5 extends the IO framework to each element of the transducer for the beamforming investigation. It shows that the minimum-variance (MV), Wiener-filtered (WF), and other beamformers can be derived as approximations to the ideal observer's strategy under each discrimination task. Performance of five beamformers has been analyzed for breast lesion discrimination. Four of the five include matched filtering of receive-channel signals before summation, because there is no loss of task information in the RF signals through the matched filtering operator. Differences among beamformers occur in subsequent steps, depending on how they process RF signals for demodulation [31, 32].

Chapter 6 presents two methods to measure the spatiotemporal impulse response of ultrasonic systems. The accurate measurements are difficult to obtain or generate by some software programs because small, unknown perturbations in the linear array geometry can make significant changes in the pulse-echo field patterns. Two methods following

the linear model for pulse-echo RF data are introduced, one using scattering spheres and the other using reconstructions from projections of line scatterer echoes. While the first method mostly involves experimental implementations, the second method is similar to image reconstruction used in photon transmission or emission computed tomography [33].

Finally, Chapter 7 summarizes this research, and outlines possible future directions for this dissertation work.

# CHAPTER 2

## BACKGROUND: IMAGE MODELING AND PERFORMANCE ASSESSMENTS

### 2.1 Introduction

In medical imaging, analysis of the system is possible only by modeling each component, from the object at the input, the system used to generate image data, to the decision made by a human or computational observer. Our model for ultrasound imaging analysis is illustrated in Figure 2.1. The image formation includes the *acquisition* and *display* stages [12]. The acquisition stage produces discrete-time RF echo signals given by vector  $\mathbf{g}$  from continuous objects  $f(\mathbf{x}, t)$  via the continuous-to-discrete linear imaging operator  $\mathcal{H}$  that describes all aspects of pulse transmission, echo reception, and beamforming. The display stage is where RF echo data are mapped into B-mode image vectors  $\mathbf{b}$  through the discrete-to-discrete nonlinear display operator  $\mathcal{O}$ . This operator includes post-summation filtering, envelope detection, scan conversion, gray-scale mapping, and image processing leading to final envelope images.

The imaging data or final B-mode can be studied by some observers to extract features regarding the possible objects being scanned. In breast sonography, the features might indicate a lesion, or some characteristics that classify a detected lesion (e.g., as benign or malignant). However, those features are distorted by the acquisition and random processes inside the system before being displayed to the observers. Based on the information obtained, the observer infers the class of the object that is at the input of the imaging system [8]. In Figure 2.1, the imaging system has three observers. The first is human, whose measurements are time consuming to obtain and fraught with many sources of potential uncertainty. Human observer performance is limited by training and the internal noise of eye-brain systems. Yet it is the state-of-the-art for medical diagnosis (path [a]). The performance is measured by using the *two-alternative-force-choice* (2AFC) method and through the *receiver operating characteristic* (ROC) analysis, in which the area under ROC curve (AUC) is often considered as the overall performance for human observers. The largest AUC value is 1 for perfect discrimination performance, and the smallest is 0.5 resulting from use of a worthless diagnostic test. The same images can be read

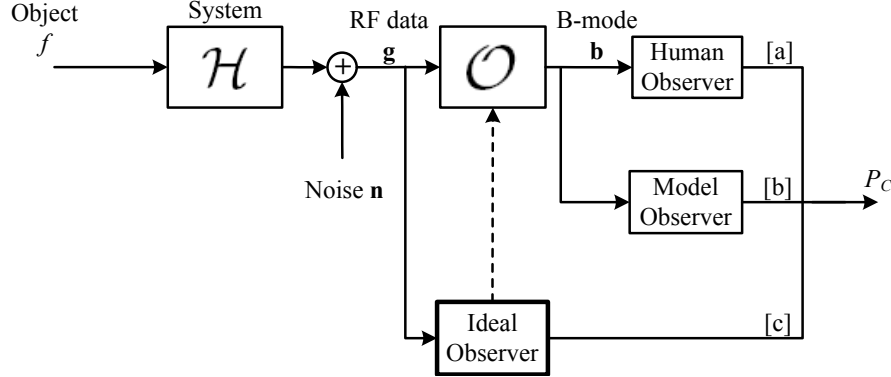


Figure 2.1: Ultrasonic image formation is diagrammed to explain task-based performance analysis. Path [a] describes image formation leading to the human observer. Path [b] indicates the same images can be viewed by model observers such as the Smith-Wagner observer [19, 20]. Path [c] indicates the ideal observer observes RF echo data, whose performance serves as an yardstick for calculating other observers' efficiency. All observer performance are measured through 2AFC observer experiments and in terms of the proportion of correct responses,  $P_C$ .

by a computational observer (also called model observer, path [b]) to minimize reader variability and to speed the reading process. Often, the performance of a model observer is related to the human observer or other observers for comparison.

The most important component of the analysis is the *ideal observer* (IO) applied to RF data (path [c]), adopting the log-likelihood ratio between the two classes of data as the test statistic. The IO combines all available information to make its decision and thus it achieves optimal task performance [8]. If the average performance from a panel of expert radiologists is significantly less than ideal, the system should be re-designed but only if it is determined that the acquisition stage of image formation (including output power, noise, transducer properties, and beamforming aspects) is limiting human performance. Sometimes task information is present in the image but difficult to observe; for example, flowing-blood echoes are found in recorded echo signal but are difficult to see without Doppler processing and color overlays. When the display stage abates human performance, image processing is often very helpful. Although the ideal observer performance is optimal, we must first obtain complete statistical knowledge of the data under consideration to compute its response. For that reason, the ideal observer analysis is limited to tasks far simpler than clinical diagnosis. It is well suited to component tasks involving specific signals that are known exactly in backgrounds known exactly (SKE/BKE tasks), or to signals known exactly where the background is known statistically (SKE/BKS tasks).

The IO approach was first applied to B-mode image data because that is what humans view for diagnosis [19, 20]. RF data contain the phase of the echo signal, which can provide

more diagnostic information even if it is not readily accessible to the human eye-brain system. RF data are usually demodulated to discard phase information in the image presented to humans for diagnosis. The ability of modern ultrasonic systems to digitize and store RF signals allows us to propose an investigation of the IO in the RF domain, which means that the IO acts on all available information. Another advantage of moving to the RF domain is that we simplify the statistical model by applying a linear system approach when computing the IO test statistic.

In subsequent sections, we describe how to model the formation of signals inside the ultrasonic system, analyze the acquisition of RF data, derive the IO on the RF, and calculate its response through a power series expansion.

## 2.2 Scattering object

### 2.2.1 Formation of malignant and benign lesions

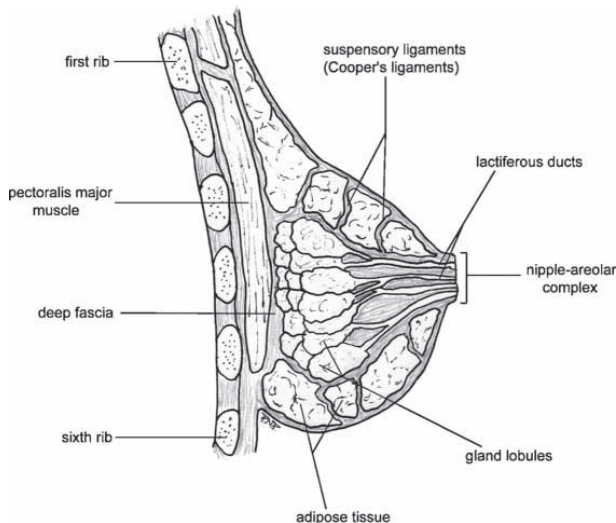


Figure 2.2: Anatomy of the female breast (Reprinted by permission of Copyright Clearance Center from Patrick Jr. [34], *Annual Review of Biomedical Engineering*, vol. 6, 109-130, © 2004 Copyright Clearance Center).

The quality of an imaging system partially depends on the task it performs; therefore, it is appropriate to review some basic background of the breast tumor being scanned inside the body. The morphology of a breast is illustrated in Figure 2.2. It is a glandular organ with the glandular tissue embedded into a stroma, which consists of fibroblast

cells, smooth muscle cells, nerve cells, and the extracellular matrix (ECM). The glandular tissue includes ductal trees that are composed of ducts and lobules. A typical tree consists of one lactiferous duct starting from one opening on the nipple, branching into segmental, subsegmental, and terminal ducts, each capped by lobules. The inner surface of ducts and lobules is covered by a single layer of luminal epithelial cells and a layer of myoepithelial cells. The main function of the epithelial cells is the secretion of milk while the myoepithelial cells are able to contract, increasing the pressure on the duct to push milk to the opening at the nipple. Figures 2.3(a),(b) diagram scanning a breast ultrason-

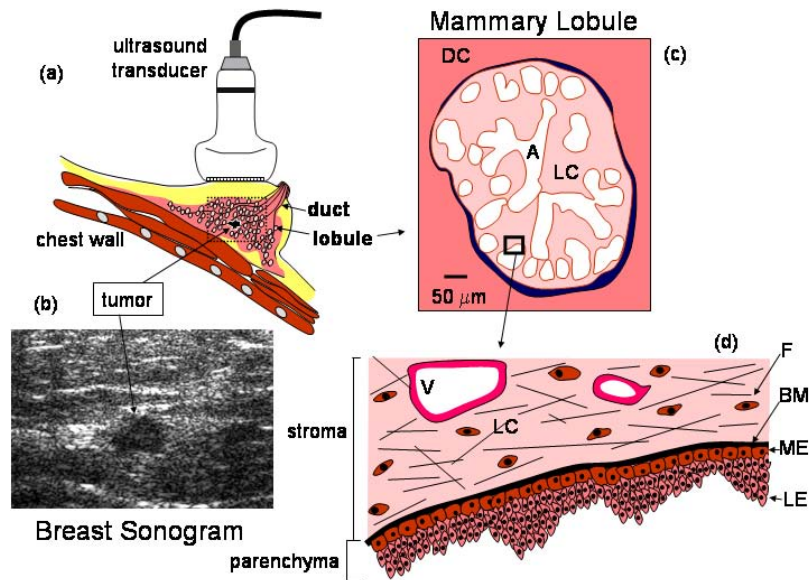


Figure 2.3: The gross and micro-anatomy of breast tissue: (a) Scanning the breast ultrasonically. (b) Sonogram. (c) The normal mammary lobule, in which A is an acini space and LC (lobular carcinoma) is the surrounding loose connective tissue stroma. (d) Basement membrane BM separating LC from parenchymal tissues; LC contains fibroblast cells F and blood vessels V; parenchymal tissues include a layer of the myoepithelial (ME) cells and the luminal epithelium (LE) (From Insana and Oelze [35], reprinted with consent of the authors, © 2008 American Scientific Publishers).

ically and give a sample sonogram showing a breast lesion. The normal mammary lobule of the breast is shown in Figures 2.3(c),(d). The epithelial cells are separated from the stroma by the basement membrane (BM), which is a layer of extracellular collagen. The signaling molecules are attached on the BM for the interaction between epithelial cells and surrounding stroma. These molecules are essential for normal breast development and cyclic monthly maintenance. In a normal condition, the organization of a breast is a balance between the tendency of the epithelium to stabilize morphometry by producing BM and the stroma that induces structural changes by selectively eroding the BM [35].

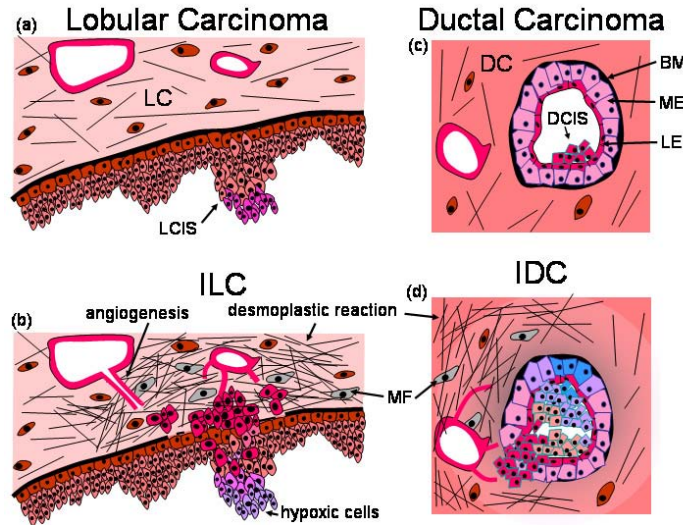


Figure 2.4: The progression of breast cancer in lobular (a,b) and ductal (c,d) (From Insana and Oelze [35], reprinted with consent of the authors, © 2008 American Scientific Publishers).

The development of breast cancer within a mammary lobule or duct is illustrated in Figure 2.4. Roughly 90% of all breast cancers begin in these tissues. Genetic alterations or regional environment changes to epithelial cells make them grow in an uncontrollable way. Cancer cells then form a mass called a tumor. The BM, serving as a barrier between the epithelial cells and stroma, is degraded and finally broken down. The loss of the BM regulation initiates neoplastic transformation, and the widespread breakdown of the BM is a histology indicator for malignant conversion. Cancer cells breaking away from tumors can be carried to other parts of the body through the bloodstream or the lymph system. They settle and grow in new locations. The process is called *metastasis*. Biochemical signaling and physical contact between the epithelial cells and surrounding connective tissues promotes neovascularization, inflammation, and a structural remodeling of the ECM. The remodeling follows the formation of myofibroblasts from normal stroma fibroblasts. Ultrasonic methods allow observation of the effects of this remodeling process even if cells cannot be resolved directly.

An ultrasonic scan of a malignant lesion is shown in Figure 2.5(a) with its boundary poorly defined and irregular. Those features are caused by the stroma surrounding the diseased duct or lobule trying to prevent the epithelial cells from expanding. The malignant lesion most often has a hypoechoic sonographic appearance. This appearance can be explained by the edema of the tissue combined with changes in the collagen that scatters ultrasound.

Lesion growths in the breast also can be benign tumors that cannot metastasize. The

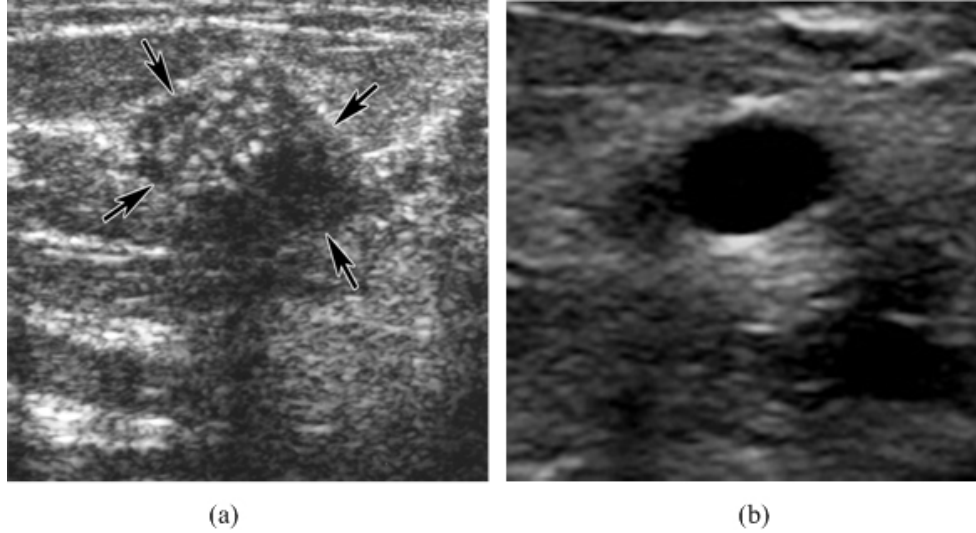


Figure 2.5: Ultrasonic scans of breast lesions that are (a) malignant, (b) a cyst (benign).

formation of a benign lesion is described in [36]. The developing, maintaining, and involution of the lobules, acini, and the smaller ducts are sensitively regulated and hormone dependent. Changes in epithelial cells that disturb the hormonal influences may lead to delay or absence of hormone-related changes, which, in turn, may lead to aberrations or variations in the breast. This process is usually associated with the accumulation of fluid, milk, mucin, or cells within the lumen of the distended lobule. The process may result in structures that are detectable with ultrasound examinations. They are recognized as benign lesions although they represent the variations and aberrations of the normal development and involution of the breast. The most common type of benign lesion is a cyst, which is illustrated in Figure 2.5(b). Since the cyst contains fluid, its sonogram has a sharply outlined round or oval mass, well-defined anterior, and anechoic interior, in contrast to the sonogram of the malignant lesion.

### 2.2.2 Discrimination tasks

By consulting with a radiologist <sup>1</sup> and combining with the BI-RADS atlas [37], five typical breast lesion features that radiologists often consider when discriminating malignant from benign lesions are selected for the study [26]. Those features are divided into five visual discrimination tasks by defining a malignant  $\mathbf{S}_1$  and benign  $\mathbf{S}_0$  matrix pair for each task. Listed in order of malignant and benign, Task 1 involves detecting a low-contrast hypoe-

---

<sup>1</sup>Dr. Karen Lindfors, UC Davis Medical Center, Sacramento, CA

choic lesion versus a no-lesion background; Task 2 requires discrimination of an elongated eccentric lesion from a circular lesion; Task 3 is discrimination of a soft, poorly defined boundary from a well-circumscribed lesion; Task 4 requires discrimination of spiculated boundary irregularities from a smooth circular boundary; and Task 5 involves discriminating a very weakly scattering hypoechoic interior from an anechoic interior. The profiles of the five tasks are illustrated in Figure 2.6 with the task difference in the bottom row. In Task 1, the observer is challenged to detect a small, low-contrast lesion; therefore, the lesion diameter is set at 3 mm and the contrast inside  $\mathbf{S}_1$  is tuned for controlling the task difficulty. In the other tasks, the discrimination information is on the boundary (Tasks 2-4) or in the interior contrast of the lesions (Task 5). In those tasks, the lesion diameter is set at 5 mm with the contrast inside  $\mathbf{S}_0$  set at 5% of the background. In Tasks 2-5, the difficulty of the tasks is controlled by systematically varying the degree of difference matrix  $\mathbf{S}_1 - \mathbf{S}_0$ . To quantify differences on a common scale, we define an *object contrast factor* as the integrated absolute value of the task difference, given by

$$C = \Delta x \Delta y \sum_i |[\mathbf{S}_1 - \mathbf{S}_0]_{ii}|, \quad (2.1)$$

where  $\Delta x, \Delta y$  are the sampling intervals on the imaging data. Observer performance is plotted as a function of the object contrast factor to observe how performance varies with task difficulties.

Another important sonographic feature discriminating between benign and malignant lesions is the prominent posterior shadow of malignant lesions as illustrated in Figure 2.5(a,b). We find this because the absorption of acoustic energy by the epithelial cells in malignant lesions is often greater than that in cystic fluid or other benign lesions. We do not consider the shadow feature in this research.

### 2.2.3 Mechanism of sonographic contrast

Solid breast tumors often appear as hypoechoic regions in sonograms. It is thought that cancerous tissue reflects sound energy less than the surrounding tissues because the effects of cellular hyperplasia, edema, and fibrosis reduce scattering. The backscattered pressure amplitude is known to generally increase with the volume density of collagen and elastin found in tissues [38]; however, fluid retention and increased cell density strongly compete with fibrosis to determine tissue echogenicity.

When incident ultrasound waves are introduced into glandular breast tissues, they are scattered by acoustic impedance heterogeneities. The tissue structures of greatest

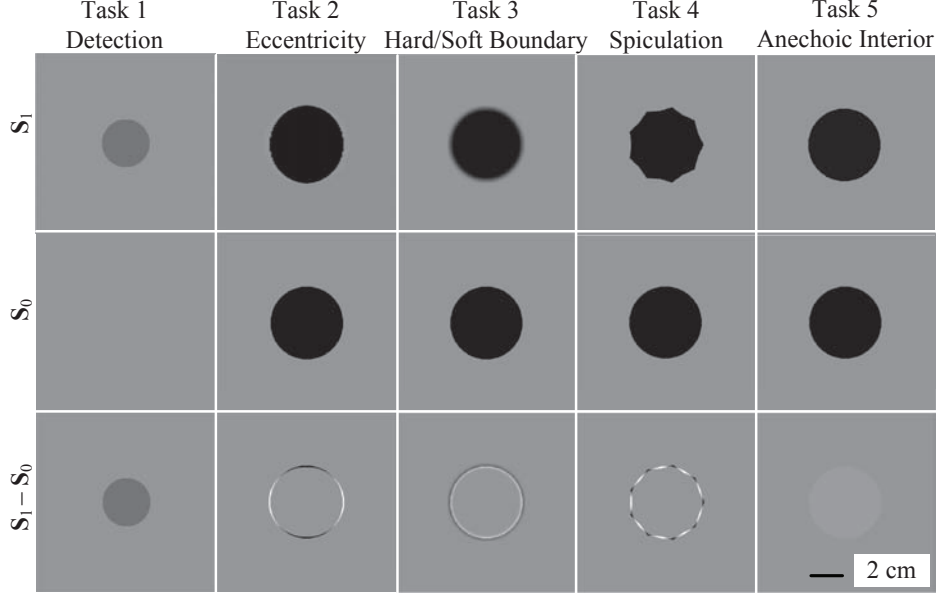


Figure 2.6: Variance profiles of “Malignant” ( $\mathbf{S}_1$ ) and “Benign” ( $\mathbf{S}_0$ ) scattering objects for five tasks. The lesion diameter is 3 mm in Task 1 and 5 mm in the other tasks. The task difference  $\mathbf{S}_1 - \mathbf{S}_0$  is shown in the bottom row of the figure [26].

interest are the sparse microvasculature and dense cell nuclei and extracellular protein-fibers, mostly collagen and elastin. These structures are randomly oriented reflectors generally smaller than the ultrasonic wavelength. Consequently, tissue reflectors are often modeled as diffuse, weakly-scattering random media (Rayleigh scatterers) that generate incoherent backscatter. As these fields are digitally received at a phase-sensitive sensor, they form spatially correlated RF echo samples that appear in B-mode images as fully developed speckle patterns [39].

These sound-tissue interactions can be understood by considering the solution to the inhomogeneous wave equation for Rayleigh scattering [40]. The scattered pressure amplitude expressed in the frequency domain is proportional to the square of spatial frequency. Transforming back to the spatial domain, scattered pressure is seen to be proportional to the second derivative (curvature) of object impedance along the direction of incident field propagation [39]. Therefore, it is the surfaces of impedance heterogeneities that scatter sound waves. For example, positioning within a Rayleigh scattering background a large disk with a different average sound speed (varying impedance mean) but equal scatterer number density (same impedance variance), we will find the sonogram will only show reflections at disk surfaces normal to the incident wave field. Ignoring coherent scattering in this study, we model tissue scatterers as a spatial distribution of surfaces represented by zero-mean random fields, where object contrast is derived from scatterer

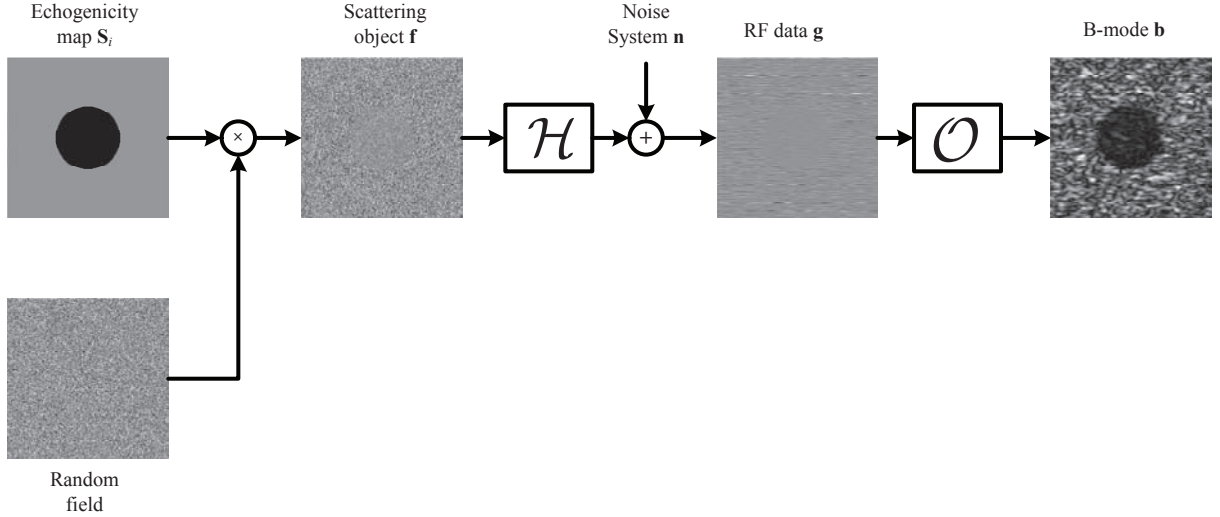


Figure 2.7: A graphical model of the sonographic process to generate standard B-mode images in an ultrasonic system.

surface density. Thus scattering is simulated by multiplying a uniform background covariance matrix by a feature template  $S$  ( $S$  shown in Figure 2.6) that defines the geometric shape of the 2-D simulated lesion. That is,  $f(x, y) = \text{WGN}(x, y) \times \sqrt{1 + S(x, y)}$ , where  $\text{WGN} \sim \mathcal{N}(0, \sigma_{\text{obj}}^2)$ . Consequently, the covariance matrix for object vector  $\mathbf{f} \sim \text{MVN}(\mathbf{0}, \Sigma_{\text{obj}})$  is  $\Sigma_{\text{obj}} = \sigma_{\text{obj}}^2(\mathbf{I} + \mathbf{S})$ , where  $\mathbf{I}$  is the identity matrix and  $\mathbf{S}$  is a diagonal matrix re-arrangement of  $S(x, y)$  with non-zero elements defining the feature geometry.

## 2.3 Signal modeling

The image formation process diagrammed in Figure 2.1 is graphically extended in Figure 2.7 without any observer. It begins with a feature template  $\mathbf{S}_i$  representing object classification  $i = 0, 1$  indicating benign or malignant, respectively. As analyzed in Section 2.2.3, the scattering object  $f(\mathbf{x})$  is formed by multiplying the template with a zero-mean, white Gaussian random field of variance  $\sigma_{\text{obj}}^2$ . The random field is stationary in time but spatially variable. The template and random field are multiplied to generate a scattering field representing amplitude-modulated, incoherent Rayleigh scattering with the spatial feature  $\mathbf{S}_i$  encoded in their spatial fluctuations (the covariance matrix) [40]. Scatterers are spatially random in an ensemble sense; however, multiplication by the feature template makes object scattering spatially nonstationary.

The interaction of pulse-echo ultrasound with the scattering media is represented by

the system operator,  $\mathcal{H}$ . It is well approximated by a linear transform under the first Born approximation [41]. By assuming the system is also shift-invariant (LSIV) and working at the focal region,  $\mathcal{H}$  can be characterized by a pulse-echo spatiotemporal impulse-response  $h(\mathbf{x}_0, t)$  given by

$$h(\mathbf{x}_0, t) = h_t(\mathbf{x}_0, t) \underset{z}{*} h_t(\mathbf{x}_0, t) ,$$

where  $h_t(\mathbf{x}_0, t)$  is the spatial impulse of the transducer due to a point scatterer at  $\mathbf{x}_0$  of the focal region, and the  $z$  axis is for the axial direction [42]. At this moment, we assume that RF data is beamformed by using the delay-and-sum (DS) strategy. The entire process is summarized by the equations for RF and B-mode data,

$$\mathbf{g} = \mathcal{H}f(\mathbf{x}) + \mathbf{n} \quad \text{and} \quad \mathbf{b} = \mathcal{O}\mathbf{g} .$$

Measurement noise is represented by the additive vector  $\mathbf{n}$ . It is modeled by an independent white Gaussian noise process  $\mathcal{N}(\mathbf{0}, \sigma_n^2 \mathbf{I})$ . Since  $\mathcal{H}$  is approximated by a linear operator, the first equation can be written in terms of a matrix multiplication by using *lexicographical reordering*, given by

$$\mathbf{g} = \mathbf{H}\mathbf{f} + \mathbf{n} . \tag{2.2}$$

The pulse-echo spatiotemporal impulse response of the system is spread over the  $m^{\text{th}}$  row of  $\mathbf{H}$  to yield RF echo sample  $g[m]$ . Under the assumption of shift invariance,  $\mathbf{H}$  is a block-Toeplitz matrix but approximated by the corresponding circulant one, which provides advantages for computation [8,26]. The spatiotemporal impulse response used to construct matrix  $\mathbf{H}$  is generated by the Field II program [43,44], with parameters extracted from a commercial system (SONOLINE Antares<sup>TM</sup> – Siemens Medical Solutions, Mountain View, CA) [30]. This impulse response makes the image generation more realistic than that of the initial study [26] which modeled the sonographic system as a Gabor pulse. Imaging system parameters were used in the echo simulations and the measurements are described below.

Beamformed RF echo waveforms are sampled at 40 MHz. This temporal sampling corresponds to a spatial sampling along the beam axis of 0.02 mm for a  $c = 1540$  m/s tissue-like sound speed. The lateral sampling interval is set at 0.2 mm, equal to the element pitch. We set a 40-mm transmit/receive focal length and a 96-element ( $\sim 20$  mm) active aperture ( $f/2$  in plane). The array has 192 total elements separated by a 0.02 mm element kerf. The elevational element length is 25 mm and it is focused at 40 mm. We applied a two-cycle excitation voltage and measured a 53% pulse-echo bandwidth about a

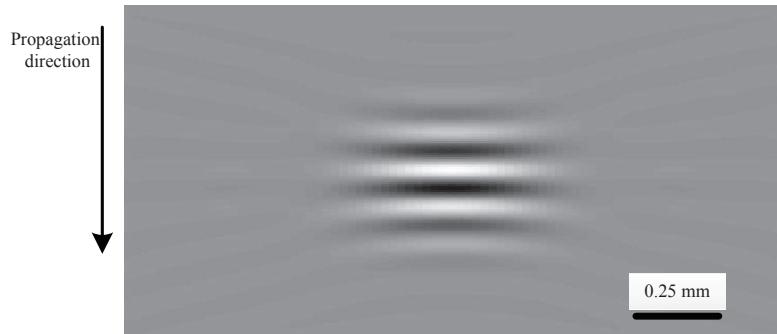


Figure 2.8: The simulated pulse-echo spatiotemporal impulse response used to generate RF data.

7.0 MHz center frequency. The beamformed, echo SNR was also measured at 32 dB near the focal length. Dynamic focusing and aperture growth features of the pulse simulator were disabled. The 2-D simulated pulse-echo spatiotemporal impulse response shown in Figure 2.8 is recorded to form a vector that becomes one row of the system matrix  $\mathbf{H}$ .

Note that because of the reordering of data into vectors, matrix  $\mathbf{S}_i$  represents the 2-D objects in Figure 2.6 as a diagonal matrix. The speckle texture on the B-mode image is similar to what is found in breast sonograms. However, the model does not include some of inhomogeneities of breast tissues such as layers of fatty tissues, ducts, Cooper’s ligaments, and fibroglandular tissue, nor have we simulated the wave front distortions that occur with heterogeneous media. Consequently, the background of the image simulation surrounding the lesions is more uniform than that in clinical sonograms.

An advantage of working in the sampled RF data domain is that the signal is well modeled by a noisy linear transformation of the object as specified by system matrix  $\mathbf{H}$  and noise variance  $\sigma_n^2$ . The ideal observer applied to the RF data is provided in the next section.

## 2.4 The ideal observer

### 2.4.1 The test statistic

This section begins by denoting hypotheses  $H_i$  for the  $i^{\text{th}}$  condition of the object ( $i = 0, 1$ ). With the generation of the scattering function described above, the object vector  $\mathbf{f}$  has a zero-mean multivariate normal distribution (MVN) under both hypotheses, with a non-

stationary and diagonal covariance matrix  $\sigma_{\text{obj}}^2(\mathbf{I} + \mathbf{S}_i)$  where  $\sigma_{\text{obj}}^2$  is background-region variance. Multivariate normal processes remain multivariate normal following linear transformations. Thus, passing the object through the noisy linear transformation in (2.2) results in another zero-mean Gaussian process for RF data  $\mathbf{g}$  under each class. The covariance matrix becomes

$$\boldsymbol{\Sigma}_i = \sigma_{\text{obj}}^2 \mathbf{H}(\mathbf{I} + \mathbf{S}_i) \mathbf{H}^t + \sigma_{\text{n}}^2 \mathbf{I}. \quad (2.3)$$

The covariance matrices for both classes still capture all the relevant statistics of the task, but they are no longer diagonal because of blurring by the imaging system via  $\mathbf{H}$ . The likelihood function of the data  $\mathbf{g}$  under each class is a zero-mean MVN given by

$$\mathbf{g} | H_i \sim \text{MVN}(\mathbf{0}, \boldsymbol{\Sigma}_i). \quad (2.4)$$

This is a *signal-known-exactly* (SKE) task with the diagnostic feature (signal) encoded in the covariance matrix  $\boldsymbol{\Sigma}_i$ . The scalar test statistic of the IO response to this discrimination task is derived from the log-likelihood ratio [15, 26],

$$\lambda(\mathbf{g}) = \ln \frac{p_1(\mathbf{g})}{p_0(\mathbf{g})}, \quad (2.5)$$

where  $p_i(\mathbf{g})$  is the probability density function under hypothesis  $H_i$ . By removing all additional terms that do not relate to the data, the test statistic  $T(\mathbf{g})$ <sup>2</sup> is simplified to

$$T(\mathbf{g}) = \frac{1}{2} \mathbf{g}^t (\boldsymbol{\Sigma}_0^{-1} - \boldsymbol{\Sigma}_1^{-1}) \mathbf{g}. \quad (2.6)$$

Decisions are made by comparing the test statistic  $T(\mathbf{g})$  to a threshold  $t$ . The performance of the IO is measured using the ROC analysis. The region of interest is the area under the ROC curve (AUC), which we will show later can be related to information theoretic measures for computing observer visual efficiency. The ideal performance also can be calculated as the proportion of correct responses  $P_C$  from a 2AFC observer experiment. This method allows us to measure the performance without determining the shape of the ROC curve.

Although the test statistic of the IO is well defined, calculating it is very challenging because of the high dimensionality of the covariance matrices. For example, if the scattering object can be represented by a  $128 \times 128$  matrix, the corresponding covariance matrix

---

<sup>2</sup>In this dissertation, both  $\lambda(\mathbf{g})$  and  $T(\mathbf{g})$  are considered as the test statistic,  $\lambda(\mathbf{g})$  is for analysis, while  $T(\mathbf{g})$  is for computation.

has the size of  $16384 \times 16384$ . Therefore inverses cannot be computed in a straightforward manner. To resolve this problem, a power-series expansion of the covariance matrices was proposed to compute matrix products involving inverse covariance matrices [26].

## 2.4.2 Power series inversion

The power series expansion for the inverse of an image covariance matrix in (2.6) relies on its decomposition into background and task-specified components, given as

$$\begin{aligned}\boldsymbol{\Sigma}_i &= \sigma_{\text{obj}}^2 \mathbf{H}(\mathbf{I} + \mathbf{S}_i)\mathbf{H}^t + \sigma_{\text{n}}^2 \mathbf{I} \\ &= \boldsymbol{\Sigma}_s + \Delta\boldsymbol{\Sigma}_i,\end{aligned}\tag{2.7}$$

where  $\boldsymbol{\Sigma}_s = \sigma_{\text{obj}}^2 \mathbf{H}\mathbf{H}^t + \sigma_{\text{n}}^2 \mathbf{I}$  is the stationary background term and  $\Delta\boldsymbol{\Sigma}_i = \sigma_{\text{obj}}^2 \mathbf{H}\mathbf{S}_i\mathbf{H}^t$  is the nonstationary task feature term. From [45], a matrix inverse can be expanded into a power series via

$$(\mathbf{I} - \mathbf{A})^{-1} = \sum_{k=0}^{\infty} \mathbf{A}^k,\tag{2.8}$$

which holds if the eigenvalues of  $\mathbf{A}$  are between  $-1$  and  $1$ . To apply (2.8), covariance matrix  $\boldsymbol{\Sigma}_i$  in (2.7) is decomposed into the form

$$\boldsymbol{\Sigma}_i = \boldsymbol{\Sigma}_s^{1/2} (\mathbf{I} + \boldsymbol{\Sigma}_s^{-1/2} \Delta\boldsymbol{\Sigma}_i \boldsymbol{\Sigma}_s^{-1/2}) \boldsymbol{\Sigma}_s^{1/2}\tag{2.9}$$

to find the inverse covariance matrix expansion

$$\begin{aligned}\boldsymbol{\Sigma}_i^{-1} &= \boldsymbol{\Sigma}_s^{-1/2} (\mathbf{I} + \boldsymbol{\Sigma}_s^{-1/2} \Delta\boldsymbol{\Sigma}_i \boldsymbol{\Sigma}_s^{-1/2})^{-1} \boldsymbol{\Sigma}_s^{-1/2} \\ &= \boldsymbol{\Sigma}_s^{-1/2} \left( \sum_{k=0}^{\infty} (-\boldsymbol{\Sigma}_s^{-1/2} \Delta\boldsymbol{\Sigma}_i \boldsymbol{\Sigma}_s^{-1/2})^k \right) \boldsymbol{\Sigma}_s^{-1/2}.\end{aligned}\tag{2.10}$$

By assuming  $\mathbf{H}$  is a circulant matrix, it can be diagonalized by a Fourier transform,

$$\mathbf{H} = \mathbf{F}^{-1} \mathbf{T} \mathbf{F},\tag{2.11}$$

where  $\mathbf{F}$  is the 2-D forward discrete Fourier transform matrix, and  $\mathbf{T}$  is a diagonal matrix whose elements are the eigenvalues of  $\mathbf{H}$  [8]. Consequently,  $\boldsymbol{\Sigma}_s$  can be decomposed as

$$\boldsymbol{\Sigma}_s = \mathbf{F}^{-1} \mathbf{N}_s \mathbf{F},\tag{2.12}$$

where  $\mathbf{N}_s$  is also diagonal with elements

$$[\mathbf{N}_s]_{ii} = \sigma_{\text{obj}}^2 |[\mathbf{T}]_{ii}|^2 + \sigma_n^2. \quad (2.13)$$

Thus the only inverse required is of the stationary component,  $\Sigma_s$ , which is quickly computed by the Fourier technique. Terms from (2.6),  $\mathbf{g}^t \Sigma_i^{-1} \mathbf{g}$ , can be written as

$$\begin{aligned} \mathbf{g}^t \Sigma_i^{-1} \mathbf{g} &= \mathbf{g}^t \Sigma_s^{-1/2} \left( \sum_{k=0}^{\infty} (-\Sigma_s^{-1/2} \Delta \Sigma_i \Sigma_s^{-1/2})^k \right) \Sigma_s^{-1/2} \mathbf{g} \\ &= \mathbf{g}^t \left( \sum_{k=0}^{\infty} (-\Sigma_s^{-1} \Delta \Sigma_i)^k \right) \Sigma_s^{-1} \mathbf{g}, \end{aligned} \quad (2.14)$$

which yields iterations for calculation, given as

$$\begin{aligned} \mathbf{q}_{k+1} &= -\Sigma_s^{-1} \Delta \Sigma_i \mathbf{q}_k \text{ and} \\ \mathbf{p}_{k+1} &= \mathbf{p}_k + \mathbf{q}_{k+1}. \end{aligned} \quad (2.15)$$

The iterative process is started with  $\mathbf{p}_0 = \mathbf{q}_0 = \Sigma_s^{-1} \mathbf{g}$ .

The rate of convergence of the test statistic depends on each task condition. For Task 1, the series converges within error specifications after just one iteration. However, it requires 50 iterations in Tasks 2-4 and up to 100 iterations in Task 5. Once the test statistic is calculated, IO performance can be measured through ROC analysis.

### 2.4.3 Performance through ROC analysis

ROC analysis is the standard method for assessing observer performance for binary classification problems [10]. The ROC curve depicts the probability of *detection*  $P_D$  as a function of the *false alarm* rate  $P_F$ .  $P_D$  is also called the *sensitivity of the test* for detecting malignant features that are present. Those curves can be generated from histograms of test statistic responses for each of the two classes of data in Figure 2.9(a). These histograms approximate probability density functions,  $q_i(\lambda)$  of the test statistic  $\lambda(\mathbf{g})$  under each hypothesis  $H_i$  ( $i = 0,1$ ). Selecting threshold  $t$  and integrating, we find the cumulative distributions  $P_D$  and  $P_F$  as we sweep through the range of  $t$  (see [8], Chapter 13),

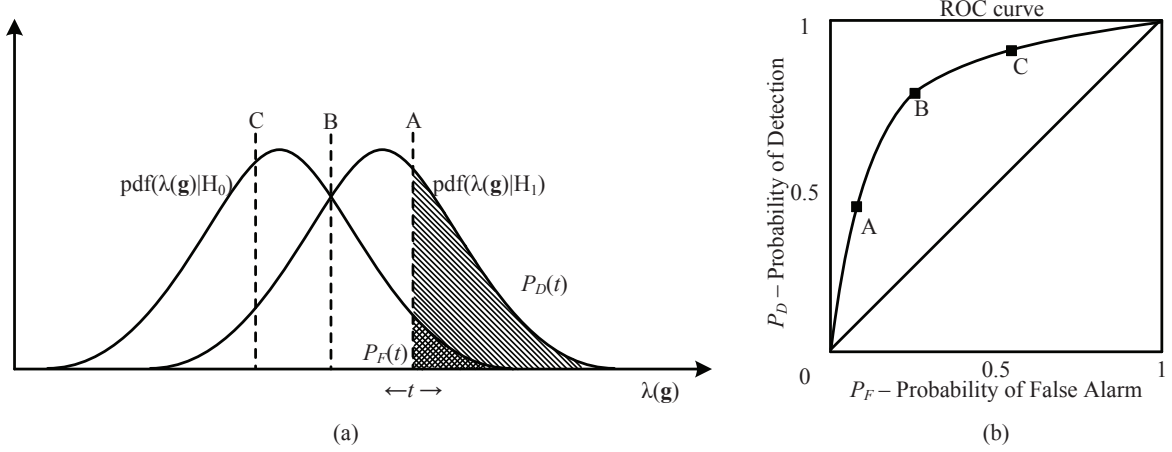


Figure 2.9: (a) The pdfs of the test statistic  $\lambda$  under two hypotheses and  $(P_D, P_F)$  at a specific threshold  $t$ . (b) An ROC curve with three threshold levels [8].

$$\begin{aligned}
 P_D(t) &= \Pr(\lambda(\mathbf{g}) > t | H_1) = \int_t^\infty d\lambda(\mathbf{g}) q_1(\lambda) \\
 P_F(t) &= \Pr(\lambda(\mathbf{g}) > t | H_0) = \int_t^\infty d\lambda(\mathbf{g}) q_0(\lambda) .
 \end{aligned} \tag{2.16}$$

With  $t$  from  $-\infty$  to  $\infty$ ,  $P_D$  and  $P_F$  range from 0 to 1. Plotting  $P_D$  against  $P_F$  the ROC curve is generated as in Figure 2.8(b). The three points labeled A, B and C represent three pairs  $(P_D, P_F)$  calculated at different thresholds  $t$ . AUC is a common figure of merit for evaluating overall observer performance; it is given by

$$\text{AUC} = \int_0^1 dP_F P_D(P_F) . \tag{2.17}$$

With the test statistics derived from the log-likelihood ratio, the IO maximizes  $P_D$  at each value of  $P_F$ , which is the *Neyman-Pearson criterion* [46]. Consequently, the ROC curve of the IO is guaranteed to have the maximum possible AUC.

#### 2.4.4 2AFC interpretations

The ideal observer performance can be calculated from the correct percentage resulting from a 2AFC experiment without determining the shape of ROC curve [15]. AUC in

(2.17) is

$$\text{AUC} = - \int_{-\infty}^{\infty} dt P_D(t) \frac{d}{dt} P_F(t) . \quad (2.18)$$

Combine with (2.16) to obtain

$$\begin{aligned} \text{AUC} &= \int_{-\infty}^{\infty} dt q_0(t) \int_t^{\infty} d\lambda q_1(\lambda) \\ &= \int_{-\infty}^{\infty} dt q_0(t) \int_{-\infty}^{\infty} d\lambda q_1(\lambda) \text{step}(\lambda - t) \\ &= \Pr[\lambda(\mathbf{g}|\mathbf{H}_1) > \lambda(\mathbf{g}|\mathbf{H}_0)] , \end{aligned} \quad (2.19)$$

where the step function equals 1 for positive arguments and 0 for negative arguments. Equation (2.19) is the basis of the numerical procedure for estimating AUC from a 2AFC experiment which is often used in human observer studies [26].

In the experiment, we normally generate 2000 pairs of RF data for the observer study to compute  $\lambda(\mathbf{g}_{i,j})$ . We define the score for trial  $j$  ( $1 \leq j \leq 2000$ ) as

$$o_j = \text{step}(\lambda(\mathbf{g}_{1,j}) - \lambda(\mathbf{g}_{0,j})) . \quad (2.20)$$

Since  $o_j = 0$  or 1 only, the net scores yield  $P_C$  and therefore AUC for the observer.

### 2.4.5 Performance metrics

By comparison with other commonly used observer performance metrics, the ideal observer AUC is converted to the *detectability index* through

$$d_A = 2\text{erf}^{-1}(2\text{AUC} - 1) . \quad (2.21)$$

As AUC varies from 0.5 to 1, the range of  $d_A$  is from 0 to infinity. Subscript  $A$  refers to a detectability computed from AUC.

The IO performance also can be quantified through the *ideal observer signal-to-noise*,  $\text{SNR}_I$ , which is calculated from moments of the test statistic  $\lambda(\mathbf{g})$ ,

$$\text{SNR}_I = \frac{\bar{\lambda}_1 - \bar{\lambda}_0}{\sqrt{(\sigma_1^2 + \sigma_0^2)/2}} , \quad (2.22)$$

where  $\bar{\lambda}_i$  and  $\sigma_i^2$  are means and variances conditioned on hypothesis  $\mathbf{H}_i$  being true. It measures the separation between the two pdfs for  $\lambda$ , illustrated in Figure 2.9(a) in units

of their common standard deviation. When  $\lambda$  is normally distributed,  $\text{SNR}_I$  is related to AUC through the error function [15] (see Appendix A)

$$\text{AUC} = \frac{1}{2} + \frac{1}{2} \text{erf} \left( \frac{\text{SNR}_I}{2} \right), \quad (2.23)$$

and therefore  $d_A = \text{SNR}_I$ .

The normality condition is usually adopted – explicitly or implicitly – in photon-based imaging modalities. Barrett and colleagues [15] have shown that if the log-likelihood ratio is normally distributed in one hypotheses, it must also be normally distributed under the other with the same variance. The normality condition has unified AUC and  $\text{SNR}_I$  for the ideal observer performance.

## 2.5 Human observer

In medical practice, the decision maker is a human observer whose performance depends on diagnostic information available from the observed images. The performance depends on the ability of the imaging device to record task information in the RF echo signal, the effects of any additional post-processing, display algorithms, and intrinsic limitations including training and internal noises inside the eye-brain system. Therefore, maximizing accessible diagnostic information in a sonogram requires an efficient transfer of task information at each step in the process. A big difference in performance between human and ideal observers provides a reason to search for a post-processing algorithm that enhances accessibility of the information to humans and reduces the performance gap.

As with IO, human observers can be evaluated using the 2AFC paradigm that also yields a proportion of correct responses ( $P_C$ ).  $P_C$  is converted to the detectability index for human observer,  $d_H = d_{A|Human}$ , to calculate the efficiency of transferring information from the RF echo signals to the human decision maker. Human and ideal observer performance difference are quantified by the *observer efficiency* [47],

$$\eta_H = \left( \frac{d_H}{d_I} \right)^2, \quad (2.24)$$

where  $d_H$  and  $d_I = d_{A|IO}$  are the detectability indices of human and ideal observers for images generated at the same object contrast factor. When efficiency is low,  $d_I$  can be so large that it is difficult to calculate accurately in the 2AFC procedure. Psychophysical studies have found that the detectability indices are usually related linearly to object

contrast factors. Hence, there are advantages to defining  $\eta$  as the ratio of squared feature contrasts for the two observers having the same detectability index; that is [26],

$$\eta_H = \left( \frac{C_I}{C_H} \right)^2, \quad (2.25)$$

where  $C_H$  and  $C_I$  are the contrast factors for human and ideal observers that generate equivalent performance,  $d_A = d_H$ . For statistical reasons, we adjust task difficulty in simulated image to achieve  $P_C \sim 0.7 - 0.8$  for human observers.

When human and ideal performance are comparable, the efficiency approaches one, and in that case, the human observer is able to use all available diagnostic information in the data to perform the visual task. If the efficiency is much less than one, either post-processing data is inappropriate or the human observer is inefficient at extracting relevant information from the data to perform the task. A low value for  $\eta_H$  is an indication that post-processing data could be beneficial.

Human observer studies are expensive, time consuming, and occasionally unstable even with training. Therefore, computational observers that mimic human performance have many advantages [14]. These observers help narrow down the list of different approaches in designing the system before performing human observer experiments as the ultimate measure of visual discrimination efficiency.

## 2.6 Wiener filter as approximation to ideal strategy

By truncating the power series expansion of (2.10) at  $k = 1$ , the inverse covariance matrix  $\Sigma_i^{-1}$  is approximately

$$\Sigma_i^{-1} \simeq \Sigma_s^{-1} - \Sigma_s^{-1} \Delta \Sigma_i \Sigma_s^{-1}. \quad (2.26)$$

Therefore

$$\begin{aligned} \Sigma_0^{-1} - \Sigma_1^{-1} &\simeq \Sigma_s^{-1} (\Delta \Sigma_1 - \Delta \Sigma_0) \Sigma_s^{-1} \\ &= \Sigma_s^{-1} \mathbf{H} \Delta \mathbf{S} \mathbf{H}^t \Sigma_s^{-1}, \end{aligned} \quad (2.27)$$

where  $\Delta \mathbf{S} = \sigma_{\text{obj}}^2 (\mathbf{S}_1 - \mathbf{S}_0)$  defines *the task information*. Substitute (2.27) into (2.6) and we find

$$T(\mathbf{g}) \approx \frac{1}{2} \mathbf{g}^t \Sigma_s^{-1} \mathbf{H} \Delta \mathbf{S} \mathbf{H}^t \Sigma_s^{-1} \mathbf{g}. \quad (2.28)$$

The matrix product  $\mathbf{H}^t \Sigma_s^{-1} \mathbf{g}$  is equivalent to applying a Wiener filter to the RF data. Hence, the strategy of the first-order approximation to the IO is to filter the RF data,

square the result, multiply it by the task information, and compare the scalar result to a threshold to make a decision. The first-order approximation only holds for low-contrast tasks. We can see that  $\mathbf{H}^t \boldsymbol{\Sigma}_s^{-1} \mathbf{g}$  is a Wiener-filtered echo signal by applying the Fourier decompositions of  $\mathbf{H}$  and  $\boldsymbol{\Sigma}_s$  from (2.11) to (2.13). We have  $\mathbf{H}^t \boldsymbol{\Sigma}_s^{-1} = \mathbf{F}^{-1} \mathbf{W} \mathbf{F}$ , where  $\mathbf{W}$  is a diagonal matrix with its elements on the main diagonal given by

$$[\mathbf{W}]_{ii} = \frac{[\mathbf{T}^t]_{ii}}{\sigma_{\text{obj}}^2 |[\mathbf{T}]_{ii}|^2 + \sigma_{\text{n}}^2}. \quad (2.29)$$

$[\mathbf{T}]_{ii}$  are eigenvalues of  $\mathbf{H}$ . Since the IO combines all information available to make the best decision, Wiener filtering of RF data may help the human observer capture some important information for the diagnosis. The first-order approximation of the ideal strategy in (2.28) suggests that the RF data be Wiener filtered before computing the B-mode images. Since the filter involves  $\boldsymbol{\Sigma}_s^{-1}$ , the stationary component of the covariance matrix, we name it the *stationary Wiener filter* to discriminate it from another filter derived in this research. In the first study [26], the stationary Wiener filter was found to improve human observer performance in the first four of the five tasks in Figure 2.6. Further details on the results are provided in Chapter 4.

## 2.7 Summary

This chapter describes the ultrasonic system as a linear model. By analyzing various features of sonograms that distinguish benign and malignant lesions, we proposed a panel of five discrimination tasks for five typical features, and classified the input signal (i.e., the scattering object) into two hypotheses in each task. Each feature is translated into conditional probabilities – likelihood function – that quantify the visual task. These scattering objects lead to RF echo-signals used to derive the ideal observer acting on data in the RF domain. Calculating the IO response involves a computational challenge of inverting high-dimensional covariance matrices. The calculation is accomplished by using a power series expansion. All observers are evaluated by using the 2AFC method and their performance is measured through the ROC analysis. We also introduce the derivation of the stationary Wiener filter in the RF domain as the first-order approximation of the ideal strategy [26]. Note that we are not measuring human detection efficiency for medical diagnostic tasks under clinical situations. We control all aspects of the tasks and provide observers with significant prior information not available clinically, so as to specifically measure the advantages of various signal processing approaches that affect performance.

## CHAPTER 3

# OBJECTIVE ASSESSMENT OF IMAGE QUALITY IN SONOGRAPHY

### 3.1 Introduction

Before continuing to describe our research, we briefly review the derivation of Wagner’s unified theory in radiography and the ideal observer of B-mode images, both developed nearly thirty years ago [12,19,20]. Our extension of the ideal observer framework to the RF echo domain for sonography introduces new challenges not experienced in photon-based imaging methods. These difference are also emphasized in Section 3.1.3.

#### 3.1.1 Wagner’s unified theory

The SNR theory published by Wagner and Brown in 1985 [12] broke new ground in medical imaging by providing an analysis for modern medical imaging system design, evaluation, and optimization. The theory was derived for low-contrast detection tasks in photon imaging with assumptions of a linear shift invariant (LSIV) system, stationary additive Gaussian noise, and SKE/BKE paradigm. We begin by considering a test statistic operating on image data that leads to the derivation of the ideal observer.

In radiography, Poisson photon statistics are accurately modeled at the output elements of a detector as multivariate normal (MVN) when photon counts are sufficiently large. The imaging contrast is created by photon absorption with important diagnostic features encoded in the object mean. Spatial variations in the mean of the object function  $\bar{f}$  map linearly into variations in the mean of the imaging data  $\bar{\mathbf{g}}$ . In the context of 2AFC studies, therefore, radiographic data  $\mathbf{g}$  under each hypothesis  $H_i$  ( $i = 0,1$ ) is given by the same linear imaging equation

$$\mathbf{g} = \mathbf{H}\mathbf{f}_i + \mathbf{n} , \tag{3.1}$$

---

Portions of this chapter are reprinted, with permission, from N.Q. Nguyen, C.K. Abbey, and M.F. Insana, “Detectability index describes the information conveyed by sonographic images,” in *Proceedings of the IEEE Ultrasonics Symposium* (in press), © 2011 IEEE.

where  $\mathbf{f}_i$  is the object function. Unlike image modeling in (2.3) and (2.4) for sonography, task contrast  $\mathbf{S}_i$  is encoded in the mean of the object functions. For the SKE/BKS task,  $\mathbf{f}_i$  becomes deterministic and  $\mathbf{f}_i = \mathbf{S}_i$ .  $\mathbf{n} \sim \text{MVN}(\mathbf{0}, \boldsymbol{\Sigma}_n)$  with  $\boldsymbol{\Sigma}_n = \sigma_n^2 \mathbf{I}$ . The pdf  $p_i(\mathbf{g})$  of data  $\mathbf{g}$  under hypothesis  $H_i$  ( $i = 0, 1$ ) is given by

$$p_i(\mathbf{g}) = (2\pi)^{-K/2} (\det(\boldsymbol{\Sigma}_n))^{-1/2} \exp\left(-\frac{1}{2}(\mathbf{g} - \mathbf{H}\mathbf{f}_i)^t \boldsymbol{\Sigma}_n^{-1} (\mathbf{g} - \mathbf{H}\mathbf{f}_i)\right), \quad (3.2)$$

where  $K$  is the dimension of  $\mathbf{g}$ . The IO test statistic is given by

$$\begin{aligned} \lambda_{\text{lin}}(\mathbf{g}) &= \log \frac{p_1(\mathbf{g})}{p_0(\mathbf{g})} \\ &= -\frac{1}{2}(\mathbf{g} - \mathbf{H}\mathbf{f}_1)^t \boldsymbol{\Sigma}_n^{-1} (\mathbf{g} - \mathbf{H}\mathbf{f}_1) + \frac{1}{2}(\mathbf{g} - \mathbf{H}\mathbf{f}_0)^t \boldsymbol{\Sigma}_n^{-1} (\mathbf{g} - \mathbf{H}\mathbf{f}_0). \end{aligned} \quad (3.3)$$

After removing terms that do not relate to data  $\mathbf{g}$ , we obtain a simpler form given by

$$T_{\text{lin}}(\mathbf{g}) = [\mathbf{H}(\mathbf{f}_1 - \mathbf{f}_0)]^t \boldsymbol{\Sigma}_n^{-1} \mathbf{g}. \quad (3.4)$$

For the SKE/BKE task,  $\Delta\mathbf{S} = \mathbf{f}_1 - \mathbf{f}_0$ , and the ideal observer test statistic derived from the log likelihood ratio is now linear in  $\mathbf{g}$ ,

$$T_{\text{lin}}(\mathbf{g}) = (\mathbf{H}\Delta\mathbf{S})^t \boldsymbol{\Sigma}_n^{-1} \mathbf{g}. \quad (3.5)$$

The lesion signal-to-noise ratio  $\text{SNR}_I^2$  is

$$\text{SNR}_I^2 = \frac{(E_1\{T_{\text{lin}}\} - E_0\{T_{\text{lin}}\})^2}{(\text{var}_1\{T_{\text{lin}}\} + \text{var}_0\{T_{\text{lin}}\})/2}, \quad (3.6)$$

where  $E_i\{T_{\text{lin}}\}$  and  $\text{var}_i\{T_{\text{lin}}\}$  are means and variances under hypothesis  $H_i$ . From (3.1) and (3.2), we have

$$E_1\{T_{\text{lin}}\} - E_0\{T_{\text{lin}}\} = (\mathbf{H}\Delta\mathbf{S})^t \boldsymbol{\Sigma}_n^{-1} (\mathbf{H}\Delta\mathbf{S}), \quad (3.7)$$

and

$$\begin{aligned} \text{var}_i\{T_{\text{lin}}\} &= \text{cov}(\mathbf{g}_i) \\ &= (\mathbf{H}\Delta\mathbf{S})^t \boldsymbol{\Sigma}_n^{-1} \text{cov}(\mathbf{n}, \mathbf{n}) \boldsymbol{\Sigma}_n^{-1} (\mathbf{H}\Delta\mathbf{S}) \\ &= (\mathbf{H}\Delta\mathbf{S})^t \boldsymbol{\Sigma}_n^{-1} (\mathbf{H}\Delta\mathbf{S}) \text{ for } i = 0, 1. \end{aligned} \quad (3.8)$$

Thus,

$$\text{SNR}_I^2 = (\mathbf{H}\Delta\mathbf{S})^t \Sigma_n^{-1} (\mathbf{H}\Delta\mathbf{S}) . \quad (3.9)$$

Under the LSIV/stationary assumption, (3.6) can be written in terms of continuous functions in the 2-D spatial frequency domain  $\mathbf{u} = (u, v)$  as

$$\text{SNR}_I^2 = \int_{\infty} d\mathbf{u} |\Delta\tilde{S}(\mathbf{u})|^2 \text{NEQ}(\mathbf{u}) , \quad (3.10)$$

where  $|\Delta\tilde{S}(\mathbf{u})|$  is the Fourier transform of  $\Delta\mathbf{S}$  and  $\text{NEQ}(\mathbf{u})$  is the noise equivalent quanta, given by

$$\text{NEQ}(\mathbf{u}) = \frac{|\tilde{H}(\mathbf{u})|^2}{\sigma_n^2} = \frac{\tilde{H}^2(\mathbf{0}) \text{MTF}^2(\mathbf{u})}{\text{NPS}(\mathbf{u})} , \quad (3.11)$$

in which  $\tilde{H}(\mathbf{0})$  is the gray-scale large-area transfer function specifying the contrast resolution, MTF is the modulation transfer function related to the spatial resolution,  $\text{MTF}(\mathbf{u}) = \tilde{H}(\mathbf{u})/\tilde{H}(\mathbf{0})$ , and NPS is the noise power spectrum of the system. Thus, NEQ is a product of three Fourier descriptions of the imaging system performance.

Because  $T_{\text{in}}(\mathbf{g})$  is a linear combination of normally distributed data, it is also normally distributed. Under this condition, the ideal observer performance as quantified by AUC is related to  $\text{SNR}_I$  through the error function (Appendix A). In summary, the Wagner-Brown SNR theory factorizes the diagnostic performance to separate the influences of the engineering metrics of the system via NEQ and task information at the system input via  $\Delta\mathbf{S}$  in the frequency domain. The factorization in (3.10) is the basis for relating laboratory measurements of the system responses to task-dependent observer performance.

Barrett et al. [17] have extended NEQ to include a lumpy background by introducing the generalized NEQ (GNEQ) for objects with a background modeled by a Gaussian random field – the the SKE/BKS task. Particularly,  $\mathbf{f}_i = \bar{\mathbf{f}}_i + \mathbf{f}_b$ , where  $\bar{\mathbf{f}}_i$  is the mean including the task, and  $\mathbf{f}_b$  is the random Gaussian background,  $\mathbf{f}_b \sim \mathcal{N}(0, \sigma_{\text{obj}}^2)$ . Task information is  $\Delta\mathbf{S} = \bar{\mathbf{f}}_1 - \bar{\mathbf{f}}_0$ , and GNEQ is given by

$$\text{GNEQ}(\mathbf{u}) = \frac{|\tilde{H}(\mathbf{u})|^2}{\sigma_{\text{obj}}^2 |\tilde{H}(\mathbf{u})|^2 + \sigma_n^2} . \quad (3.12)$$

Writing in terms of MTF,  $\tilde{H}(\mathbf{0})$ , and noise power spectrum, we have

$$\text{GNEQ}(\mathbf{u}) = \frac{\text{SNR}_0 \times \text{MTF}^2(\mathbf{u})}{\sigma_{\text{obj}}^2 (\text{SNR}_0 \times \text{MTF}^2(\mathbf{u}) + 1)} , \quad (3.13)$$

where  $\text{SNR}_0 \triangleq |\tilde{H}(\mathbf{0})|^2 \sigma_{\text{obj}}^2 / \sigma_n^2$  is the pixel SNR outside the target area.

It appears from (3.11) and (3.12) that the system can be optimized via maximization of NEQ (or GNEQ). The expression, however, is derived under strict assumptions of the system and noise, as well as for low-contrast detection tasks. For more complicated tasks or imaging systems where LSIV/stationary assumptions are violated, the system and task properties cannot be factorized. In spite of those limitations, the theory has great utility for predicting performance and was applied to many photon imaging modalities, including X-ray radiography, computerized tomography (CT), positron emission tomography (PET), and nuclear magnetic resonance (NMR) [8, 18]. The work, however, is still limited to sonographic modalities. This approach must be adapted for use in sonography because of fundamental differences in the physics of sonographic contrast compared to radiographic contrast.

### 3.1.2 Ideal observer of B-mode images

Smith, Wagner, and their co-workers were the first to derive the ideal observer acting on B-mode images [19, 20]. Besides the LSIV assumptions for the imaging system and low-contrast detection task, however, they further restricted assumptions to exclude acquisition noise and they sampled speckle spots rather than pixels to avoid pixel correlations when specifying statistical properties of data. A 2AFC psychophysics study was applied under the SKE/BKE task assumption. For each task, an observer must decide between two hypotheses:

$H_0$  : the lesion in image 0 is malignant and the lesion in image 1 is benign or

$H_1$  : the lesion in image 0 is benign and the lesion in image 1 is malignant.

Denoting  $\mathbf{b}_i$  as the B-mode image under the  $i^{\text{th}}$  hypothesis, a decision function for the ideal observer is the ratio of a likelihood function, given as

$$\Lambda_B(\mathbf{b}_0, \mathbf{b}_1) = \frac{p(\mathbf{b}_0, \mathbf{b}_1 | H_1)}{p(\mathbf{b}_0, \mathbf{b}_1 | H_0)}, \quad (3.14)$$

where  $p(\mathbf{b}_0, \mathbf{b}_1 | H_i)$  is the joint conditional pdf of the data of images  $\mathbf{b}_0$  and  $\mathbf{b}_1$  under  $H_i$ . With the assumption of complex, multivariate Gaussian random process for RF data, the

B-mode image data have a Rayleigh distribution [19], given by

$$\begin{aligned}
p(\mathbf{b}_0, \mathbf{b}_1 | H_0) &= \prod_{i=1}^M \frac{b_{0i}}{\psi_m} \exp\left(\frac{-b_{0i}^2}{2\psi_m}\right) \prod_{j=1}^M \frac{b_{1j}}{\psi_b} \exp\left(\frac{-b_{1j}^2}{2\psi_b}\right) \\
p(\mathbf{b}_0, \mathbf{b}_1 | H_1) &= \prod_{i=1}^M \frac{b_{0i}}{\psi_b} \exp\left(\frac{-b_{0i}^2}{2\psi_b}\right) \prod_{j=1}^M \frac{b_{1j}}{\psi_m} \exp\left(\frac{-b_{1j}^2}{2\psi_m}\right),
\end{aligned} \tag{3.15}$$

where the parameters  $2\psi_m$  and  $2\psi_b$  are the mean backscattering intensities, respectively, for the malignant and the benign lesion images.  $M$  is the number of independent data samples in the target area available for the decision maker. This number is smaller than  $K$ , the dimension of data column vectors  $\mathbf{g}$  and  $\mathbf{b}$  [19].

Substituting (3.15) into (3.14), we find

$$\Lambda_B(\mathbf{b}_0, \mathbf{b}_1) = \prod_{i=1}^M \exp\left[\frac{b_{0i}^2}{2} \left(\frac{1}{\psi_m} - \frac{1}{\psi_b}\right)\right] \prod_{j=1}^M \exp\left[\frac{-b_{1j}^2}{2} \left(\frac{1}{\psi_m} - \frac{1}{\psi_b}\right)\right]. \tag{3.16}$$

Taking the log of the likelihood ratio we obtain

$$\begin{aligned}
\lambda_B(\mathbf{b}_1, \mathbf{b}_2) &= \left(\frac{\psi_b - \psi_m}{2\psi_m\psi_b}\right) \left(\sum_{i=1}^M b_{0i}^2 - \sum_{j=1}^M b_{1j}^2\right) \\
&= \mathbf{a}^t \mathbf{b}_0^2 - \mathbf{a}^t \mathbf{b}_1^2,
\end{aligned} \tag{3.17}$$

where the sums in the first equation in (3.17) are taken over all independent image samples inside the lesion area. The second equation represents the log-likelihood in terms of energies of whole images, in which  $\mathbf{a}$  is a vector of weights;  $a_i = 0$  for pixel  $i$  outside the lesion, and  $a_i = (\psi_b - \psi_m)/(2\psi_m\psi_b)$  for pixel  $i$  inside the lesion.

The decision then is made based on the comparison

$$\lambda_B(\mathbf{b}_0, \mathbf{b}_1) = \mathbf{a}^t \mathbf{b}_0^2 - \mathbf{a}^t \mathbf{b}_1^2 \geq 0. \tag{3.18}$$

The decision favors hypothesis  $H_1$  for positive values and  $H_0$  otherwise. A sufficient test statistic is therefore

$$\lambda_B(\mathbf{b}) = \sum_{i=1}^M b_i^2. \tag{3.19}$$

So instead of calculating the test statistic decision variable as in (3.18), we calculate each sum separately for each image and compare the two. The moments of the test statistic

under each hypothesis are [20]

$$\begin{aligned} E[\lambda_B|H_1] &= 2M\psi_m; & E[\lambda_B|H_0] &= 2M\psi_b \\ \text{var}[\lambda_B|H_1] &= 4M\psi_m^2; & \text{var}[\lambda_B|H_0] &= 4M\psi_b^2. \end{aligned} \quad (3.20)$$

The lesion SNR on B-mode images is given by

$$\begin{aligned} \text{SNR}_B &= \frac{E[\lambda_B|H_1] - E[\lambda_B|H_0]}{\sqrt{(\text{var}[\lambda_B|H_1] + \text{var}[\lambda_B|H_0])/2}} \\ &= M^{1/2} \frac{\psi_m - \psi_b}{\sqrt{\psi_m^2 + \psi_b^2}} = M^{1/2} C_\psi \\ &= \sqrt{\frac{A}{S_c}} C_\psi, \end{aligned} \quad (3.21)$$

where  $A$  is the area of the lesion,  $S_c$  is the speckle correlation size [19, 20], and  $C_\psi$  is a signal-to-noise ratio.  $C_\psi$  is a function of the contrast for a small signal difference. Therefore,

$$\text{SNR}_B^2 = \frac{A}{S_c} \text{SNR}_0 C, \quad (3.22)$$

where  $C$  is the lesion contrast need to be detected and  $\text{SNR}_0$  is the speckle signal-to-noise ratio, whose inverse is the speckle contrast. For Rayleigh distributed envelope data,  $\text{SNR}_0 = 1.91$  is a constant [19].

Thus, the detection  $\text{SNR}_B$  is factorized into the task information ( $A, C$ ) and a system dependent effect ( $S_c$ ) in the spatial domain, which is analogous to radiographic photon density in the frequency domain. The Rayleigh distribution also requires the assumption of the fully developed speckle, which holds for a medium composed of randomly positioned point scatterer with a density greater than about 10 scatterers per pulse volume. Speckle density in the image data is related to information density in the object data since the speckle density is the number of independent signal samples presented to observers on which they base decisions. Outside the focal zone of the transducer, however, speckle patterns can be correlated over very long ranges. In any case, independent sample density may be estimated from signal coherence lengths [21].

Although the closed-form expression for the detection  $\text{SNR}_B$  was achieved for special cases, the assumptions are rarely held under clinical imaging conditions. If these limiting assumptions could be reduced, a more general form would be found, and we would have a valuable analysis tool for task-based system design decisions.

### 3.1.3 Challenges in assessment of sonographic quality

Extending the objective assessment of sonographic visual discrimination performance to the RF data allows us to relax some of the stringent assumptions because the RF data are well modeled by a linear transformation of the scattering object. However, the analysis of RF data introduces new analytical challenges. First, the test statistic involves inverses of high-dimensional covariance matrices that could not be calculated straightforwardly. This computational issue has been resolved in our initial study by applying a power series expansion to approximate each of the matrix inverses [26]. Second, the quadratic form of the test statistic for RF data may diverge significantly from a normal distribution, and therefore AUC is not clearly related to detectability in the  $\text{SNR}_I$  measure. Under MVN distribution for  $\mathbf{g}$ , the test statistic follows a  $\chi^2$  distribution [48]. A normal distribution can be adopted for  $T$  or  $\lambda$  under some conditions, but validity is difficult to verify because of the high dimensionality of the covariance matrices. Test statistic normality is very important if we are to separate ideal performance into task information and engineering metrics of the imaging system, which is very convenient for system evaluation and optimization [12]. Even if it is reasonable to assume normality, the quadratic form of the ideal observer test statistic still prevents Wagner’s SNR theory from being applied directly to sonographic modalities.

In the next sections, we show that the connection in (2.23) between the ideal AUC and the  $\text{SNR}_I$  adopted for radiographic data becomes uncertain in our sonographic tasks. We also establish a rigorous relationship between the ideal observer performance, task information, and engineering metrics to evaluate sonographic quality. We first focus on how the measurement of ideal performance describes task information conveyed in the RF data. By setting the ideal observer analysis in a broader approach that involves optimizing metrics rooted from information theory [49], we introduce the Kullback-Leibler divergence ( $J$ ) to the framework as the primary metric and relate it to existing metrics of AUC and  $\text{SNR}_I$ .  $J$  is a fundamental metric in information theory that measures the divergence between the two distributions of data [50]. The relation is found analytically under the normal distribution of the test statistic. Without the normality condition, Monte Carlo studies must be used to evaluate relations among those metrics. From the connection between AUC and  $J$ , we are able to separate the diagnostic performance into task and imaging instrument properties by developing the *Acquisition Information Spectrum* (AIS) quantity for sonographic systems, which is equivalent to NEQ in photon imaging. AIS describes the effectiveness of the system in transferring diagnostic task information from the object to the RF data of the acquisition stage in sonographic imaging process.

## 3.2 Task performance and information

### 3.2.1 Kullback-Leibler divergence

A broader approach to image evaluation relies on performance metrics that are rooted in information theory. These metrics include divergence, discrimination, and entropy with the likelihood ratio playing a central role in their measurements [49]. Describing an imaging system as a device that transfers task information from object to observer, channel capacity, based on *Shannon entropy* [51], is a figure of merit that can be used. Shaw [16] considered imaging devices as a communication channel and computed the channel capacity based on Shannon entropy to show that the information stored in data resulting from the imaging process is given by the detective quantum efficiency (DQE), a quantity related to  $\text{SNR}_I^2$  through integration. In the context of the 2AFC experiments in this research, we find that the *Kullback-Leibler entropy* is more appropriate [52]. To see this, we start with Bayes's theorem for two class discrimination

$$P(H_i|\mathbf{g}) = \frac{P(H_i)p_i(\mathbf{g})}{P(H_0)p_0(\mathbf{g}) + P(H_1)p_1(\mathbf{g})}, \quad i = 0, 1, \quad (3.23)$$

in which  $P(H_i|\mathbf{g})$  and  $P(H_i)$  are the probabilities of  $H_i$  with and without knowledge of  $\mathbf{g}$ , respectively. Applying (3.23) to the log-likelihood ratio yields

$$\ln \frac{p_1(\mathbf{g})}{p_0(\mathbf{g})} = \ln \frac{P(H_1|\mathbf{g})}{P(H_0|\mathbf{g})} - \ln \frac{P(H_1)}{P(H_0)}. \quad (3.24)$$

The first and second terms in the right-hand side of (3.24) are discrimination information supporting  $H_1$  with and without knowledge of  $\mathbf{g}$ . Thus, the difference in the left-hand side  $\ln [p_1(\mathbf{g})/p_0(\mathbf{g})]$  is the information brought by  $\mathbf{g}$  for discrimination in favor of  $H_1$  against  $H_0$  [50]. Average information is given by

$$\bar{\lambda}_{1:0} = \int d\mathbf{g} p_1(\mathbf{g}) \ln \frac{p_1(\mathbf{g})}{p_0(\mathbf{g})}, \quad (3.25)$$

where integration is over the data sample space. Similarly, the average information in favor of  $H_0$  against  $H_1$  is specified by

$$\bar{\lambda}_{0:1} = \int d\mathbf{g} p_0(\mathbf{g}) \ln \frac{p_0(\mathbf{g})}{p_1(\mathbf{g})}. \quad (3.26)$$

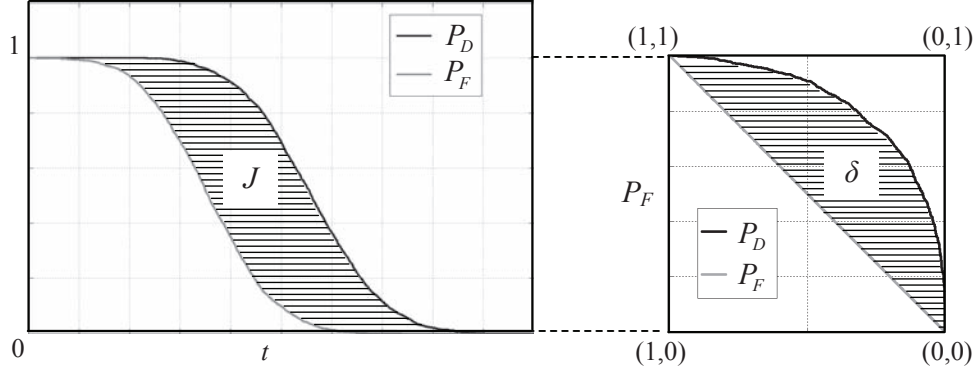


Figure 3.1: (Left) Plots of  $P_D$  and  $P_F$  as functions of the decision threshold  $t$ . The area between the two curves equals the Kullback-Leibler divergence,  $J$ . (Right) The corresponding ROC curve (in reverse).

The two quantities,  $\bar{\lambda}_{1:0}$  and  $\bar{\lambda}_{0:1}$ , are summed together to form  $J$  as a net measure of the *divergence of information* contained in  $\mathbf{g}$  for discriminating between the two hypotheses,

$$J = \bar{\lambda}_{1:0} + \bar{\lambda}_{0:1} = \int d\mathbf{g} (p_1(\mathbf{g}) - p_0(\mathbf{g})) \ln \frac{p_1(\mathbf{g})}{p_0(\mathbf{g})}. \quad (3.27)$$

$J$  is a unitless scalar that quantifies the difficulty of discriminating between distributions  $p_0(\mathbf{g})$  and  $p_1(\mathbf{g})$  based on the information contained in the data.

To establish a connection between  $J$  and the ideal observer AUC, we first relate  $J$  to probabilities of detection  $P_D(t)$  and  $P_F(t)$  in (2.16) by

$$J = \int_{-\infty}^{\infty} dt [P_D(t) - P_F(t)]. \quad (3.28)$$

See Section B.1, Appendix B for the proof.

Equation (3.28) is illustrated in Figure. 3.1(left) by showing  $J$  as the area between the two curves  $P_D$  and  $P_F$  over the range of  $t$ . The corresponding ROC curve is plotted on the right with a reversed abscissa. While the ROC curve depicts  $P_D$  as a function of  $P_F$ , the main diagonal (from (0,0) to (1,1)) depicts  $P_F$  as a function of itself, and the area under it equals 0.5. If the data provide no information,  $AUC = 0.5$  and  $P_D$  becomes identical to  $P_F$ . Therefore,  $\delta$  (the area between  $P_D$  and  $P_F$ ) can also be considered as information brought by data but measured through the ideal observer performance. It

can be calculated as

$$\begin{aligned} \delta &= \int_0^1 dP_F [P_D - P_F] \\ &= \int_{-\infty}^{\infty} dt q_0(t) [P_D(t) - P_F(t)] . \end{aligned} \quad (3.29)$$

Comparing to (3.28), we find the relation between  $J$  and AUC depends on the distribution of the test statistic  $q_0(t)$  underlying hypothesis  $H_0$ . Under the normality condition, we can prove

$$J = \frac{(\bar{\lambda}_1 - \bar{\lambda}_0)^2}{(\sigma_1^2 + \sigma_0^2)/2} . \quad (3.30)$$

See the proof in Section B.2, Appendix B.

Combining (3.30) with (2.22) and (2.23), we obtain

$$\text{AUC} = \frac{1}{2} + \frac{1}{2} \text{erf} \left( \frac{\sqrt{J}}{2} \right) , \quad (3.31)$$

or  $J = d_A^2 = \text{SNR}_I^2$ . Thus, the relation between  $J$  and AUC then reduces to the error function, in a manner similar to the radiography situation. Without the normality condition, the AUC cannot be computed in a closed form, although it can be measured experimentally. Therefore, Monte Carlo studies are used to evaluate numerically the relations among those metrics.

### 3.2.2 Monte Carlo studies

The main challenge in calculating  $J$  from (3.27) is computing the matrix determinants in the likelihood ratio. However, (3.28) allows us to calculate  $J$  without first calculating determinants since they act to shift both curves on Figure 3.1(left) along  $t$  by the same interval, and do not affect the area measured between the two probability distribution curves. Consequently,  $J$  can be found by plotting  $P_F$  and  $P_D$  based on the test statistic  $T(\mathbf{g})$  instead of  $\lambda(\mathbf{g})$ , which is already calculated through a power series expansion.

We investigate the relation among performance metrics over the five tasks of breast sonography, given in Figure 2.6. First, we computed figures of merit  $d_A^2$ ,  $\text{SNR}_I^2$ , and  $J$  as a function of object contrast by using (2.21), (2.22), and (3.28). The numerical calculations began with 2AFC observer studies involving simulations of 2000 RF echo data pairs of  $\mathbf{g}$  for each feature contrast in each task.  $d_A$  was computed from AUC by applying (2.21).  $\text{SNR}_I^2$  was computed from the moments of  $T(\mathbf{g})$ . The test statistic is considered to have

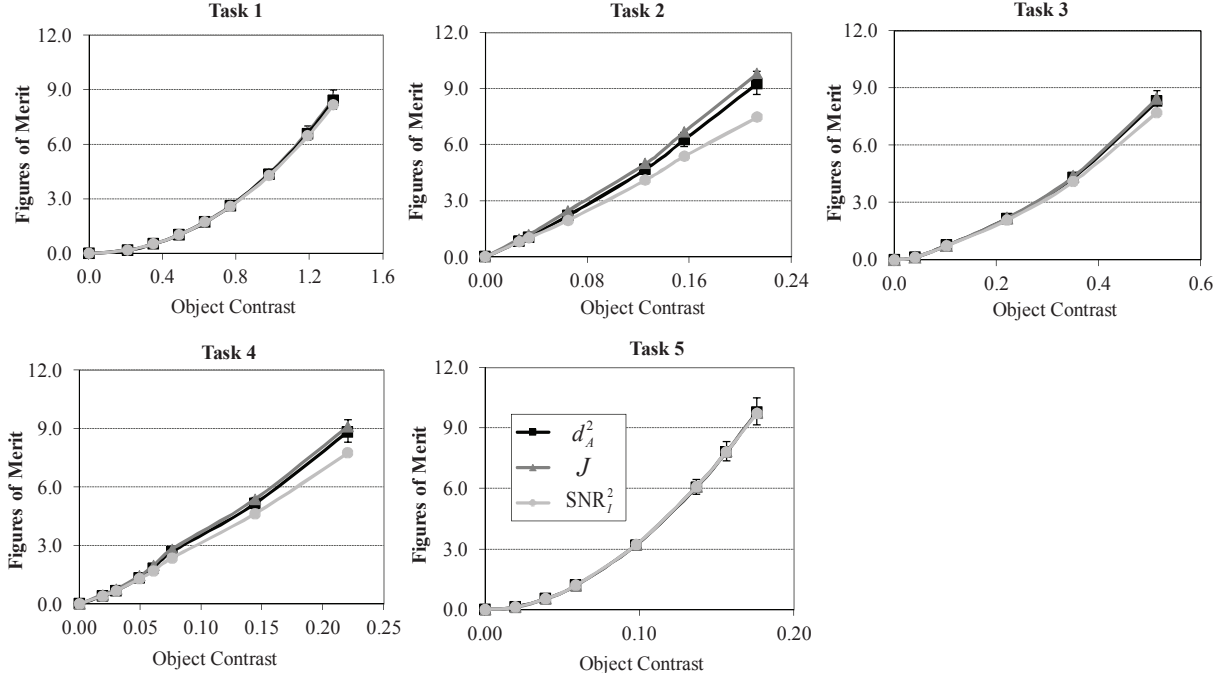


Figure 3.2: Comparison of detectability index  $d_A^2$ ,  $J$ , and  $\text{SNR}_I^2$  for the five visual tasks considered. Each of the three curves in a graph is plotted as a function of the object contrast factor. The legend in the plot of Task 5 applies to all plots [32].

converged when the increment changes less than 0.001% after each iteration.  $J$  was found numerically from plots of  $P_D(t)$  and  $P_F(t)$  was computed from histograms of  $T$  values. To control for case variability, we used the same RF echo data pairs to calculate these three figures of merit at each object contrast. Plots of the results for the five tasks are found in Figure 3.2.

The confidence intervals for  $d_A^2$  values are calculated by considering AUC as a binomial variance. For each task, feature contrast ranges from  $\text{AUC} = 50\%$  to  $\text{AUC} \simeq 99\%$ ; the latter value corresponds to  $d_A^2 \simeq 10$ . Above this range, AUC reaches 100% and comparisons are inaccurate.

Figure 3.2 shows that all three metrics are identical for the large area of signal difference in Tasks 1, 3, and 5. The test statistic may be considered normally distributed in those tasks. However, there are some differences among metrics in Tasks 2 and 4, indicating that the normality condition may not be satisfied. There are bigger difference between  $d_A^2$  and  $\text{SNR}_I^2$ , up to 14.5% for Task 2. In all tasks, the  $J$  values are equivalent to  $d_A^2$ . The greatest difference between  $J$  and  $d_A^2$  is in Task 2, approximately 5%, and still within the confidence intervals of  $d_A^2$ .

Thus, over the five discrimination tasks investigated, the standard detectability index

$d_A^2$  is better approximated by  $J$  than  $\text{SNR}_I^2$ . Consequently, AUC for the ideal observer describes the information of divergence conveyed in the RF data. Estimates of the ideal performance from  $\text{SNR}_I^2$ , measuring the distance of the ideal observer response, can be affected by small deviations from normal of the test statistic, which may happen in sonographic tasks.

### 3.2.3 Normal log likelihood ratio

The differences among three metrics  $d_A^2$ ,  $\text{SNR}_I^2$ , and  $J$  vary over the five tasks. The observation leads us to a conjecture that the normality condition depends on the task information. In Tasks 1, 3, and 5, where the task difference  $\mathbf{S}_1 - \mathbf{S}_0$  (see Figure 2.6) is large and spans the whole lesion, the test statistic is assumed to be normally distributed, or the normality condition is satisfied, since those performance metrics of the ideal observer are nearly identical to each other. However, in Tasks 2 and 4, where the task difference is small and limited to areas near the edges of lesions, the normality condition is questionable since there is a big gap between  $d_A^2$  and  $\text{SNR}_I^2$ .

This conjecture on the normality condition in sonographic tasks can be validated by changing the average of lesion brightness in variance masks for Tasks 2 and 4, and by doing so, the signal areas are changed to keep the ideal performance at comparable levels. First, we set the lesion brightness at 90% of the background, making those tasks low contrast. The object contrast factor is reduced and the signal area  $\Delta\mathbf{S}$  needs to be expanded to maintain the observer performance. The three metrics for those tasks are shown in Figure 3.3(a,b). In those tasks,  $d_A^2$ ,  $J$ , and  $\text{SNR}_I^2$  are identical, indicating the normality condition holds. The normality condition is also illustrated through a histogram of the test statistic for Task 4 with benign data shown in Figure 3.3(c). The histogram fits well to the Gaussian curve plotted with the same mean and variance estimated from the histogram.

In the other direction, the average brightness lesion is reduced to 1% of the background, making those tasks very high contrast. The task difference becomes even smaller when ideal performance reaches 100%. The performance metrics are shown in Figure 3.4(a,b). In those tasks,  $d_A^2$ ,  $J$ , and  $\text{SNR}_I^2$  become more divergent from each other. In Task 4,  $J$  is slightly out of the confidence interval  $d_A^2$ . The biggest divergence is still between  $d_A^2$  and  $\text{SNR}_I^2$  in Task 2, up to 30%. An example of the test statistic histogram for Task 4 with benign data is shown in Figure 3.4(c). Its shape has a deviation from the Gaussian curve drawn with the same mean and variance. Visual tasks with such a high contrast resolution, however, do not create much challenge in breast cancer diagnosis. Such anechoic regions

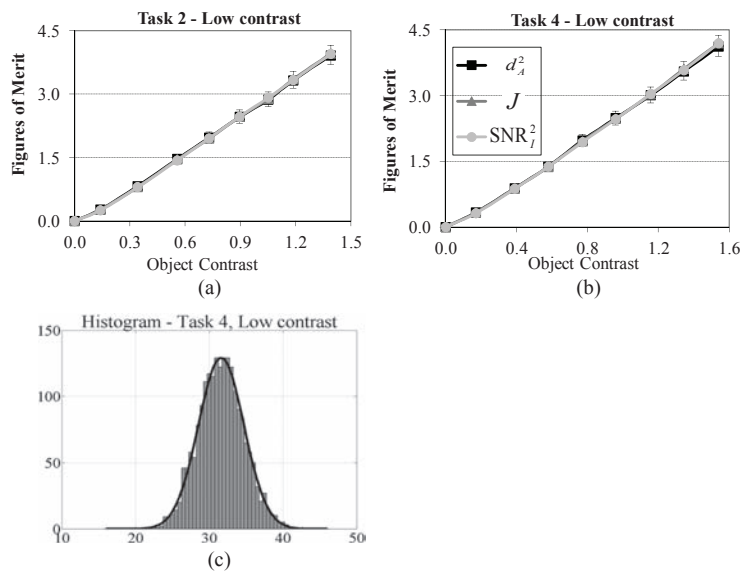


Figure 3.3: Comparisons of detectability indices  $d_A^2$ ,  $J$ , and  $SNR_I^2$  for Tasks 2 (a) and Task 4 (b) with low contrast. Legend in Task 4 applies to Task 2. The contrast inside the lesion is set to be 90% of the background. (c) An example of the test statistic histogram in Task 4 and the Gaussian curve with the same mean and variance for low contrast.

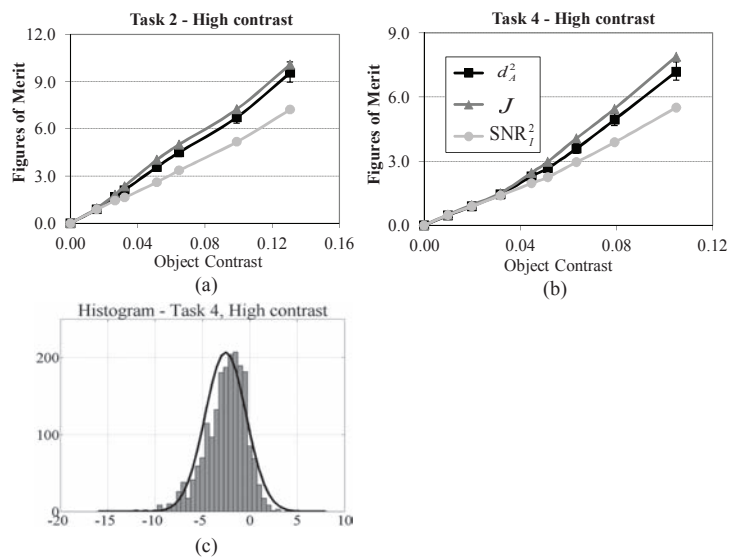


Figure 3.4: Comparisons of detectability indices  $d_A^2$ ,  $J$ , and  $SNR_I^2$  for Tasks 2 (a) and 4 (b) with higher contrast. Legend in Task 4 applies to Task 2. The contrast inside the lesion is set to be 1% of the background. (c) An example of the test statistic histogram in Task 4 and the Gaussian curve with the same mean and variance.

usually indicate a cyst with fluid and are easily detected as benign by physicians. Solid breast tumors often appear as hypoechoic regions in sonograms; therefore, low-contrast tasks have received more attention in breast cancer diagnosis using sonograms.

### 3.3 Acquisition information spectrum

#### 3.3.1 Information analysis

In this section, we derive an equivalent factorization for the ideal performance on RF signals. The derivation must be adapted to the model that encodes features in second-order statistics of data, e.g. the covariance matrix. Numerically, results in Section 3.2.2 show that for the quadratic form of the test statistic, the ideal observer AUC or its detectability index  $d_A^2$  better describe the divergence between the two classes of data  $J$  than the divergence between the two class of the ideal observer response  $\text{SNR}_I^2$ . We derive the NEQ-like quantity for the sonographic system on the basic of this new relation. Like Wagner and Brown [12], we assume LSIV/stationary assumptions for the system with detecting a low-contrast lesion task (Task 1).

From (3.27), we can write

$$\begin{aligned} J &= E_1\{\lambda(\mathbf{g})\} - E_0\{\lambda(\mathbf{g})\} \\ &= E_1\{T(\mathbf{g})\} - E_0\{T(\mathbf{g})\}, \end{aligned} \quad (3.32)$$

where  $E_i\{\cdot\}$  is the mean underlying hypothesis  $H_i$  ( $i = 0,1$ ),  $\lambda(\mathbf{g})$  and  $T(\mathbf{g})$  are given in (2.5) and (2.6), respectively. By replacing the expression of  $T(\mathbf{g})$  into  $E_i\{\cdot\}$ , one can obtain

$$\begin{aligned} E_i\{T(\mathbf{g})\} &= \frac{1}{2}E_i\{\mathbf{g}^t(\boldsymbol{\Sigma}_0^{-1} - \boldsymbol{\Sigma}_1^{-1})\mathbf{g}\} \\ &= \frac{1}{2}E_i\{\text{Tr}[(\boldsymbol{\Sigma}_0^{-1} - \boldsymbol{\Sigma}_1^{-1})\mathbf{g}\mathbf{g}^t]\}, \end{aligned} \quad (3.33)$$

for  $i = 0, 1$ . Switching between  $E_i\{\cdot\}$  and  $\text{Tr}[\cdot]$  and recalling that  $\mathbf{g}|H_i \sim \text{MVN}(\mathbf{0}, \boldsymbol{\Sigma}_i)$ , we obtain

$$E_i\{T(\mathbf{g})\} = \frac{1}{2}\text{Tr}[(\boldsymbol{\Sigma}_0^{-1} - \boldsymbol{\Sigma}_1^{-1})\boldsymbol{\Sigma}_i] \text{ for } i = 0, 1. \quad (3.34)$$

Replacing (3.34) into (3.32), the Kullback-Leibler divergence  $J$  can be expressed in alge-

braic form as [53]

$$J = \frac{1}{2} \text{Tr} [(\boldsymbol{\Sigma}_0^{-1} - \boldsymbol{\Sigma}_1^{-1}) (\boldsymbol{\Sigma}_1 - \boldsymbol{\Sigma}_0)] , \quad (3.35)$$

where  $\text{Tr}(\cdot)$  is the trace of the matrix. As usual, the challenge to computing  $J$  in this form is the inversion of covariance matrices. In [26], each inverse is expanded in a power series, which allows them to be computed precisely. It is shown numerically that the power series expansion effectively converges after one iteration in detecting low-contrast feature tasks. Therefore, we can substitute the first-order approximation form of (2.26) into (3.35) and obtain

$$J \simeq \frac{1}{2} \text{Tr} [\boldsymbol{\Sigma}_s^{-1} (\Delta \boldsymbol{\Sigma}_1 - \Delta \boldsymbol{\Sigma}_0) \boldsymbol{\Sigma}_s^{-1} (\boldsymbol{\Sigma}_1 - \boldsymbol{\Sigma}_0)] , \quad (3.36)$$

where  $\boldsymbol{\Sigma}_s$  and  $\Delta \boldsymbol{\Sigma}_{0,1}$  are given in (2.7). The only matrix to be inverted in this approximation is  $\boldsymbol{\Sigma}_s$  which is stationary, and therefore efficiently computed using Fourier methods.

From the numerical result in Section 3.2.2, we can substitute the standard detectability index  $d_A^2$  for  $J$  in low-contrast tasks to be consistent with the literature on ideal observer analysis. With  $\boldsymbol{\Sigma}_s$  and  $\Delta \boldsymbol{\Sigma}_i$  from (2.7), (3.28) becomes

$$d_A^2 \simeq \frac{1}{2} \text{Tr} [\mathbf{K}_s \Delta \mathbf{S} \mathbf{K}_s \Delta \mathbf{S}] . \quad (3.37)$$

where  $\mathbf{K}_s = \mathbf{H}^t \boldsymbol{\Sigma}_s^{-1} \mathbf{H}$  and  $\Delta \mathbf{S} = \sigma_{\text{obj}}^2 (\mathbf{S}_1 - \mathbf{S}_0)$ , which is the task information.

Under the LSIV/stationary assumptions,  $\mathbf{K}_s$  is stationary and can be diagonalized using Fourier techniques, given by

$$\mathbf{K}_s = \mathbf{F}^{-1} \tilde{\mathbf{K}}_s \mathbf{F}, \quad (3.38)$$

where  $\mathbf{F}$  is the 2-D forward DFT matrix [8]. Since  $\tilde{\mathbf{K}}_s$  is diagonal, its elements can be represented by a single index,  $\tilde{\mathbf{K}}_s(k, k) = \tilde{K}_s(k)$ . Similarly,  $\Delta \mathbf{S} = \mathbf{F}^{-1} \tilde{\Delta \mathbf{S}} \mathbf{F}$ , and therefore (3.37) may be expressed as a double sum over frequency indices

$$\begin{aligned} d_A^2 &\simeq \frac{1}{2} \text{Tr} [\tilde{\mathbf{K}}_s \tilde{\Delta \mathbf{S}} \tilde{\mathbf{K}}_s \tilde{\Delta \mathbf{S}}] \\ &= \frac{1}{2} \sum_k \sum_l \tilde{K}_s(k) \Delta \tilde{S}(k, l) \Delta \tilde{S}(l, k) \tilde{K}_s(l). \end{aligned} \quad (3.39)$$

Because  $\Delta \mathbf{S}$  is nonstationary,  $\tilde{\Delta \mathbf{S}}$  is not diagonal but spread over the 2-D spatial frequency domain. However,  $\Delta \mathbf{S}$  is real and diagonal, so  $\tilde{\Delta \mathbf{S}}$  is Hermitian and circulant, i.e.  $\Delta \tilde{S}(l, k) = \Delta \tilde{S}^*(k, l) = \Delta \tilde{S}(l - k)$ , in which  $\Delta \tilde{S}(k)$  is the Fourier transform of  $\Delta \mathbf{S}$  but re-arranged into a column vector before taking the transform.

Expressing (3.39) as a continuous function of the 2-D spatial frequency variable,  $\mathbf{u} =$

$(u, v)$ , we have

$$\begin{aligned}
d_A^2 &\simeq \frac{1}{2} \int_{\infty} d\mathbf{u} \int_{\infty} d\mathbf{u}' \tilde{K}_s(\mathbf{u}') \left| \Delta\tilde{S}(\mathbf{u} - \mathbf{u}') \right|^2 \tilde{K}_s(\mathbf{u}) \\
&= \int_{\infty} d\mathbf{u} \left| \Delta\tilde{S}(\mathbf{u}) \right|^2 \left\{ \frac{1}{2} \tilde{K}_s(\mathbf{u}') * \tilde{K}_s(-\mathbf{u}') \right\} (\mathbf{u}) \\
&= \int_{\infty} d\mathbf{u} \left| \Delta\tilde{S}(\mathbf{u}) \right|^2 \text{AIS}(\mathbf{u}) \triangleq d_{K_s}^2.
\end{aligned} \tag{3.40}$$

where  $d_{K_s}$  is a detectability index based on  $\tilde{K}_s$  given by

$$\tilde{K}_s(u, v) = \frac{\left| \tilde{H}(u, v) \right|^2}{\left| \tilde{H}(u, v) \right|^2 \sigma_{\text{obj}}^2 + \sigma_n^2}. \tag{3.41}$$

$|\tilde{H}(u, v)|$  is the magnitude of the system transfer function and  $\sigma_{\text{obj}}^2$  and  $\sigma_n^2$  are, respectively, the variance of the object background and noise processes.

Comparing (3.40) with (3.10) derived by Wagner et. al., we find there is an object contrast factor  $|\Delta\tilde{S}(\mathbf{u})|^2$  in both equations, and that NEQ in radiography is replaced by the autocorrelation function (ACF) of  $\tilde{K}_s(u, v)$  for sonography. We name the sonographic quantity *Acquisition Information Spectrum*, or  $\text{AIS}(u, v) = \frac{1}{2} \text{ACF}\{\tilde{K}_s(u, v)\}$ . When AIS is multiplied by  $|\Delta\tilde{S}|^2$  and integrated, we have measured the task information found in the RF data  $\mathbf{g}$  at the acquisition stage of image formation.

### 3.3.2 Properties of AIS

The differences in contrast mechanisms between sonography and radiography are found by comparing  $|\Delta\tilde{S}(\mathbf{u})|^2$  for the two modalities as well as NEQ and AIS. To illustrate the differences, we turn to dimensional analysis, and label the units of object function  $f$  as [obj] and the units for measurement data  $g$  and  $n$  as [data]. For 2-D radiography, the units of NEQ are [obj-mm]<sup>-2</sup> and for  $|\Delta\tilde{S}|^2$  they are [obj-mm<sup>2</sup>]<sup>2</sup>, so that integration of the product over 2-D frequency as in (3.16) yields a unitless  $\text{SNR}_f^2$ . However, for sonography, the units of AIS are [obj<sup>2</sup>-mm]<sup>-2</sup> and for  $|\Delta\tilde{S}|^2$  they are [obj<sup>2</sup>-mm<sup>2</sup>]<sup>2</sup>. Modality differences in  $|\Delta\tilde{S}|^2$  units are reflected in feature contrast mechanisms that are in the covariance rather than the mean of the object function. Thus AIS is dimensionally different from NEQ because the information for performing the task is embedded in the second-order structure of the data.

$\tilde{K}_s(u, v)$  is analogous to GNEQ in (3.12) [17] but here are two important differences.

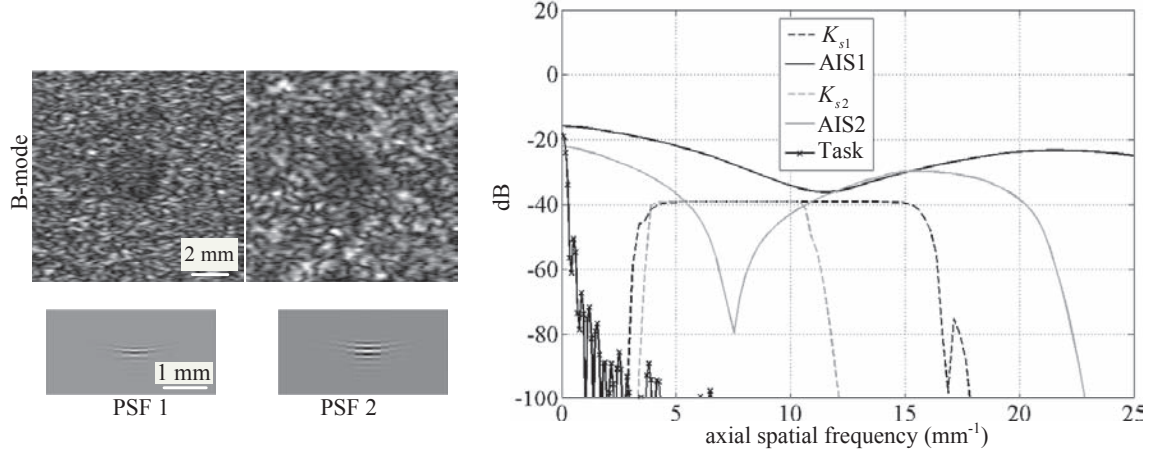


Figure 3.5: (Right) One-dimensional AIS( $u$ ) and  $K_s(u)$  curves are plotted versus spatial frequency along the beam axis for Task 1. We show results from two system configurations: the center frequency and percentage bandwidth of the two system are PSF 1 = 7.2 MHz/69.3% and PSF 2 = 6.3 MHz/38%. The pulses are measured from the SONOLINE Antares system generated by varying the excitation voltage waveform. (Left) B-mode images (top row) for the two images are shown (in linear scale) along with scaled images of the pulses (bottom row).

First, the background randomness described in (3.41) is always present in sonography because it is due to coherent speckle present in the RF echo signal. Second, since  $\text{AIS} = \frac{1}{2} \text{ACF}(\tilde{K}_s)$  for sonography and not  $\tilde{K}_s$ , there is a broader system responsiveness to object contrast than one expects from  $\text{MTF}(\mathbf{u}) = |H(\mathbf{u})|/|H(\mathbf{0})|$  alone. Also the bandpass nature of the RF echoes means that AIS always has three lobes centered at zero frequency. Examples of AIS are shown in Figure 3.5 for spatial frequencies from 0 to 25  $\text{mm}^{-1}$ . The shape of the AIS is different from that of the NEQ in photon imaging plotted in Figure 3.6. NEQ has a peak at the origin and is monotonically decreased with the increments of the spatial frequency [13]. The difference may come from the phase component presented in RF sonographic data. The AIS shape will be validated in Chapter 4.

In 2-D radiography,  $\text{NEQ}(\mathbf{u})$  measures the number of photons per unit area of the image that convey task information over the spatial frequency  $\mathbf{u}$ .  $\text{NEQ}(\mathbf{u})$  is a task-independent measure of how well the imaging system transfers information from the object to the recorded data. In sonography,  $\text{AIS}(\mathbf{u})$  measures the number of “independent RF data samples” that convey information over  $\mathbf{u}$ . It describes the transfer of information from object to RF echo data. Because it does not include display-stage processing, AIS only partially addresses image information for the acquisition stage.

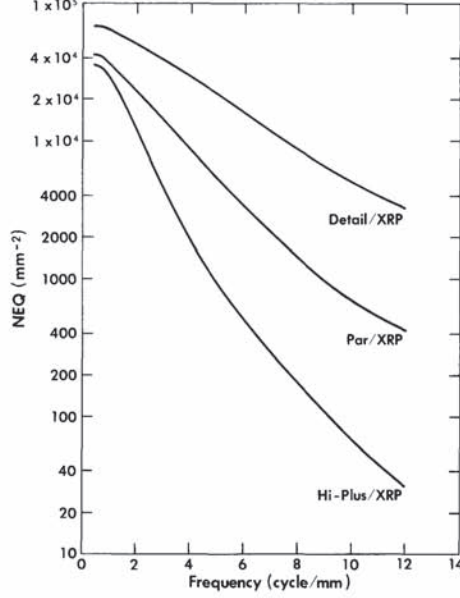


Figure 3.6: Examples of NEQ for three X-ray photographic (XRP) systems (Reprinted by permission of IEEE from Wagner [13], *IEEE Transactions on Medical Imaging*, vol. MI-2, no. 3, pp. 105-121, © 1983 IEEE).

It may be easier to interpret the results by writing (3.41) as

$$\tilde{K}_s(u, v) = \frac{\text{SNR}_0 \times \text{MTF}^2(u, v)}{\sigma_{\text{obj}}^2 (\text{SNR}_0 \times \text{MTF}^2(u, v) + 1)}, \quad (3.42)$$

where  $\text{SNR}_0 \triangleq |H(0, 0)|^2 \sigma_{\text{obj}}^2 / \sigma_n^2$  is the pixel SNR outside the target area, and  $0 \leq \text{MTF} \leq 1$ . When  $\text{MTF}^2 \simeq 1$  and  $\text{SNR}_0 \gg 1$  within measurement bandwidth  $B$ ,  $\tilde{K}_s = 1/\sigma_{\text{obj}}^2$  over  $B$ , and Wiener filtering is maximally effective at decorrelating data. AIS is maximum under these conditions, meaning the system transfers information with maximum efficiency, and there is a peak at the origin  $\text{AIS}(\mathbf{0}) = B/\sigma_{\text{obj}}^4$ .

Under conditions where the product  $\text{SNR}_0 \times \text{MTF}^2 \sim 1$ ,  $\tilde{K}_s$  is more narrow band and  $B$  is smaller. The amount of task information transferred by the system is then reduced overall. Figure 3.5 gives two examples of  $K_s$  and AIS functions for configurations measured from a commercial imaging system along with the Task 1 spectrum,  $|\Delta\tilde{S}(\mathbf{u})|^2$ . The  $K_s$  functions are nearly constant over spatial frequencies corresponding to the temporal bandwidth of the transducer because the scattering function is modeled as a white-Gaussian noise process. Detection of large low-contrast lesions is a low spatial-frequency task, so it might seem that high temporal bandwidth imaging systems might not aid in this detection task. However, the autocorrelation function within AIS means that detectability at all

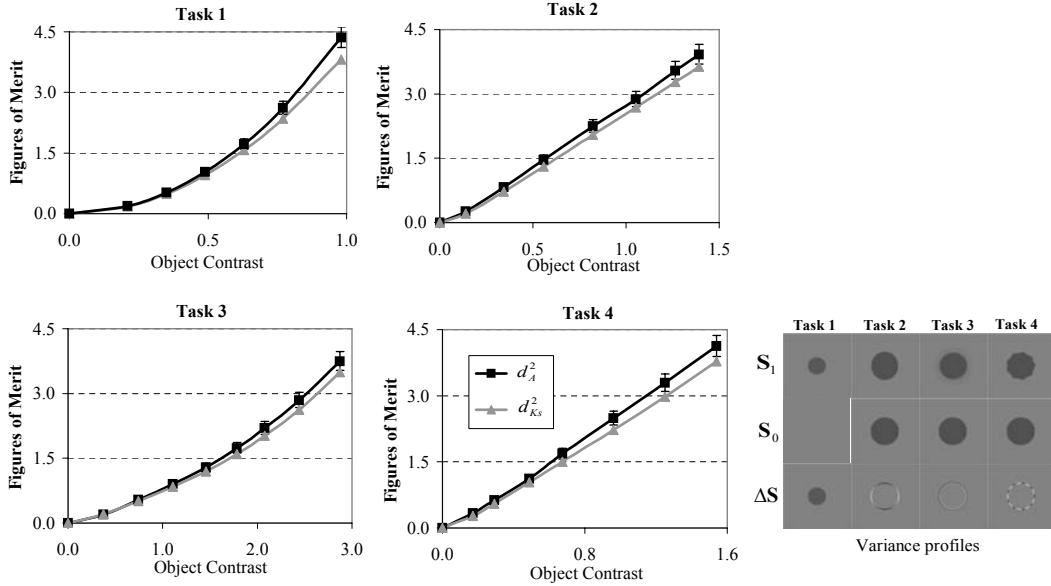


Figure 3.7: Comparison of detectability indices  $d_A^2$  and  $d_{K_s}^2$  can be made for four low-contrast tasks.  $d_{K_s}^2$  is computed using (3.32) while  $d_A$  is converted from AUC through Monte Carlo studies. All values are plotted as functions of object contrast. The legend in Task 4 applies to all plots. The lower-right corner shows variance profiles for four low-contrast tasks, including detection (Task 1), eccentricity (Task 2), hard/soft boundary (Task 3), spiculation (Task 4).

frequencies increases approximately linearly with bandwidth under high  $\text{SNR}_0$  conditions.

The temporal-frequency parameters of ultrasonic transducers are implicitly described by (3.42). Acquisition-stage variables related to center frequency, bandwidth, and beam focusing properties enter the analysis through MTF and  $\text{SNR}_0$  in well-known ways [54]. Large-area contrast resolution [12], as described in  $|H(\mathbf{0})|^2$ , is also embedded in the MTF and  $\text{SNR}_0$ . Thus (3.40) describes the information available to form a diagnostic image for low-contrast lesion detection.

### 3.3.3 Predicting performance

Equation (3.40) provides a fast computation for ideal observer detectability index without using Monte Carlo studies. The validity of assumptions made in the derivation was tested by comparing in Figure 3.7 the predicted performance from  $d_{K_s}^2$  to the ROC-based performance  $d_A^2$  measured from Monte Carlo simulations.  $d_{K_s}^2$  predicts performance at low-contrast tasks where the first-order approximation to matrix inverses holds. It is compared to  $d_A^2$  over four low-contrast tasks modified from the panel of the five typical tasks in Figure 2.6. Among those four tasks, Task 1 (low-contrast detection) is repeated,

Tasks 2-4 are from combinations between low-contrast detection and edge discrimination tasks. In those tasks, the lesion brightness is set to be 90% of the background. In Task 1, the lesion contrast is varied from 0 to  $-1.8$  dB for AUC ranging from 0.5 to 0.93 (corresponding to  $d_A^2$  from 0 to 4.5). Numerical results show that  $d_{K_s}^2$  is within the confidence interval of  $d_A^2$  in Tasks 2-4, while it begins to be out of the range in Task 1 when the contrast resolution is around  $-1.8$  dB, indicating the condition for which the first-order approximation starts being violated.

### 3.4 Summary and discussion

Using an information metric developed by Kullback and Leibler [52] and the 2AFC experimental paradigm, we have connected the information ( $J$ ) to commonly used observer performance metrics in medical imaging: area under the ROC curve (AUC), detectability index ( $d_A$ ), and lesion signal-to-noise ratio for the ideal observer ( $\text{SNR}_I$ ). The connections are all derivable in closed form when the decision variable is normally distributed.

When the distribution of the ideal observer test statistic is non-normal, Monte Carlo studies were used to compare  $J$ ,  $d_A^2$ , and  $\text{SNR}_I^2$  numerically. We first developed a method for estimating  $J$  from forced-choice image pairs that enabled us to relate the various figures of merit. We measured disagreements between  $J$  and  $\text{SNR}_I^2$  not explained by computational error when the latter is estimated from moments of the test statistic. Numerical results show agreement between  $J$  and  $d_A^2$  for each task and all contrasts considered, which establishes the equivalence between ideal observer performance and task information.

The results show that in some visual tasks where the signal area is large compared with the echo-signal coherence area imposed by the coherent imaging system, the normality condition may be assumed regardless of underlying distributions. However, for tasks requiring discrimination of boundary features, the signal area may be too small and the condition is lost. The failure of the normal assumption means that  $\text{SNR}_I^2$  calculated from moments of the ideal observer response underestimates information transfer. It is recommended that AUC or  $d_A$  should be used as the primary figure of merit for evaluating and optimizing sonographic systems.

The equivalence of  $J$  and  $d_A^2$  follows the example of Wagner and Brown in radiography [12] when seeking connections between instrument properties and ideal performance. This approach is a significant advance over our previous study [55], where we began searching for NEQ-like quantities. The AIS quantity describes the efficiency of the imaging system

at transferring information from the object to the RF echo data, and importantly it provides a rigorous link to laboratory metrics for assessing image quality. It can be combined with the task spectrum to predict task-dependent information transfer. Thus we have established an objective assessment of sonographic quality in the context of a common analysis framework used by many throughout the radiography literature. And similarly to NEQ, the AIS also provides a convenient way to report the ideal observer performance without using the Monte Carlo studies.

# CHAPTER 4

## POST-PROCESSING

### 4.1 Introduction

The ability of modern ultrasonic systems to digitize and store RF data increases the opportunity to explore post-recording processing of data before obtaining the final envelope image. The image formation process in Figure 2.7 is extended in Figure 4.1 to include operator  $\mathcal{W}$  as a supplemental filtering step applied to data in the RF domain. Several research groups have applied signal processing techniques to RF data to reduce speckle size and enhance B-mode image resolution [56–59]. However, diagnostic information cannot be increased by further processing. Therefore, any image processing algorithm applied post-detection must be evaluated in the context of how effectively the technique removes irrelevant information and enhances the observer’s accessibility to diagnostic information. The assessment should emerge from the exploration of the ideal observer, which is the appropriate measure of diagnostic information.

By analyzing the ideal observer equations, we can interpret them as the signal processing strategies the observer uses to extract information from data to make the best decision. In the initial study [26], it was found that the first-order power series approximation to the ideal strategy was equivalent to a stationary Wiener filter applied to the beamformed RF signals. The resulting envelope images yielded a measurable improvement in performance when the task was discriminating low-contrast lesion features. However, performance was reduced for high-contrast lesions, even if the discrimination task is itself low contrast, specifically when observers were asked to discriminate anechoic and hypoechoic lesions (Task 5). These previous findings suggested that, for imaging situations where there are large signal heterogeneities, filters must adaptively tune to the echo statistics wherever there is diagnostic information.

In this chapter, we extend the analysis to include a greater range of practical conditions

---

Portions of this chapter are reprinted, with permission, from N.Q. Nguyen, C.K. Abbey, and M.F. Insana, “An adaptive filter to approximate the Bayesian strategy for sonographic beamforming,” *IEEE Transactions on Medical Imaging*, vol. 30, no. 1, pp. 28-37, © 2011 IEEE.

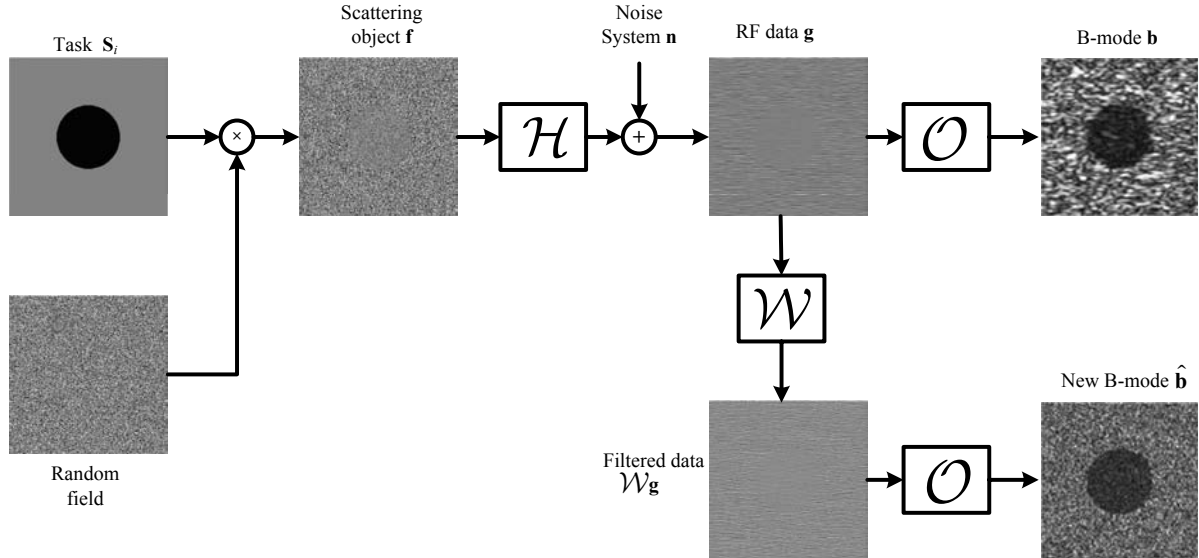


Figure 4.1: A graphical representation of the imaging process to generate sonographic images extended to include an additional filtering step applied to RF data before envelope detection (bottom row). The standard B-mode images are beamformed using conventional delay-and-sum beamforming (top row) [30].

by improving the first-order approximation. The proposed method addresses deficiencies in the application of the power series expansion to calculate the inverse of the covariance matrices, which in return yields a better approximation. The new approximation leads to an iterative Wiener filtering (IWF) approach that re-tunes the filter in regions of variable echo SNR to generate IWFB-mode images. Iteration increases task information, thus enabling the filter to adapt to variable tissue scattering conditions, but it requires a segmentation algorithm beforehand to identify regions that can benefit from iterative filtering. Most segmentations of medical ultrasound images are performed on B-mode images [60, 61]. However, our segmentation is performed on the WFB-mode images because of the reduced speckle correlation length. This modification allows us to more accurately segment lesions and with less computation time. The results show that the new filter makes an improvement in visual performance for diagnostic information contained within the lesion interior, the task where we find a reduction in performance after Wiener filtering, while keeping the performance on par with that of the Wiener filter in other tasks. The concepts are demonstrated on a commercial system by imaging a tissue-mimicking phantom where results include a realistic, shift-variant model for the system impulse response.

## 4.2 Iterative Wiener filter (IWF)

### 4.2.1 IWF as an approximation of the ideal strategy

By analyzing the power series expansion of the IO, it is found that the ability of the stationary Wiener filter to improve human observer performance depends on the accuracy of the first-order approximation. The first-order approximation to matrix inverses  $(\mathbf{I} + \mathbf{S}_i)^{-1} \simeq \mathbf{I} - \mathbf{S}_i$  is a good one when  $\mathbf{S}_i \ll \mathbf{I}$ , which is true for low-contrast features. When that is not the case, as in Task 5, the covariance matrix cannot be separated into stationary and non-stationary components. Instead we form *average* and *difference* components,

$$\boldsymbol{\Sigma}_a = \mathbf{H}(\sigma_{\text{obj}}^2 \mathbf{I} + \mathbf{S}_a) \mathbf{H}^t + \sigma_n^2 \mathbf{I} \quad \text{and} \quad \Delta \boldsymbol{\Sigma} = 0.5 \mathbf{H} \Delta \mathbf{S} \mathbf{H}^t \quad (4.1)$$

where

$$\mathbf{S}_a = 0.5 \sigma_{\text{obj}}^2 (\mathbf{S}_1 + \mathbf{S}_0) \quad \text{and} \quad \Delta \mathbf{S} = \sigma_{\text{obj}}^2 (\mathbf{S}_1 - \mathbf{S}_0) .$$

As with the stationary Wiener filter, we expand the matrices in a power series and truncate after the first term to find

$$\boldsymbol{\Sigma}_0^{-1} - \boldsymbol{\Sigma}_1^{-1} \approx 2 \boldsymbol{\Sigma}_a^{-1} \Delta \boldsymbol{\Sigma} \boldsymbol{\Sigma}_a^{-1} . \quad (4.2)$$

The new first-order approximation of test statistic  $\lambda$  becomes

$$\lambda(\mathbf{g}) \approx \frac{1}{2} \mathbf{g}^t \boldsymbol{\Sigma}_a^{-1} \mathbf{H} \Delta \mathbf{S} \mathbf{H}^t \boldsymbol{\Sigma}_a^{-1} \mathbf{g} . \quad (4.3)$$

Similarly to the derivation of the stationary Wiener filter, the first-order approximation of (4.3) provides insights into ideal strategies for discrimination. The factor  $\mathbf{H}^t \boldsymbol{\Sigma}_a^{-1} \mathbf{g} = (\mathbf{g}^t \boldsymbol{\Sigma}_a^{-1} \mathbf{H})^t$  is recognized as the new filtering strategy acting on RF echo signals. To compare with the stationary Wiener filter  $\mathbf{H}^t \boldsymbol{\Sigma}_s^{-1}$  derived from (2.28), the average covariance between two states is applied instead of the stationary background covariance. The advantage of this change is to allow the signal strength to vary significantly within any one image, provided the difference between the two images remains small. The disadvantage of the new filter is that  $\boldsymbol{\Sigma}_a$  is the covariance matrix of a non-stationary process, so we cannot use Fourier techniques to quickly compute its inverse.

The power series approach may be applied to decompose  $\boldsymbol{\Sigma}_a$  into stationary and non-stationary components,  $\boldsymbol{\Sigma}_a = \boldsymbol{\Sigma}_s + \sigma_{\text{obj}}^2 \mathbf{H} \mathbf{S}_a \mathbf{H}^t$ , yielding an iterative formula for  $\mathbf{H}^t \boldsymbol{\Sigma}_a^{-1} \mathbf{g}$

given by

$$\begin{aligned}\mathbf{q}_{i+1} &= -\sigma_{\text{obj}}^2 \mathbf{H}' \boldsymbol{\Sigma}_s^{-1} \mathbf{H} \mathbf{S}_a \mathbf{q}_i \text{ and} \\ \mathbf{p}_{i+1} &= \mathbf{p}_i + \mathbf{q}_{i+1} .\end{aligned}\tag{4.4}$$

The iterative scheme is initialized by  $\mathbf{q}_0 = \mathbf{p}_0 = \sigma_{\text{obj}}^2 \mathbf{H}' \boldsymbol{\Sigma}_s^{-1} \mathbf{g}$ . Equation (4.4) begins with the stationary Wiener filter, and iteratively converges to  $\mathbf{p}_{i+1} = \sigma_{\text{obj}}^2 \mathbf{H}' \boldsymbol{\Sigma}_a^{-1} \mathbf{g}$  using the power series inverse approximation for  $\boldsymbol{\Sigma}_a$ . We refer to the result as the *adaptive or iterative Wiener filter* and the corresponding envelope as the IWFB-mode image [30]. To compare with the stationary Wiener filter, the iterative Wiener filter is combined with the average task information  $\mathbf{S}_a$  through the iterations. Thus IWFB-mode images can adapt to the task as specified by  $\mathbf{S}_a$ , provided that  $\mathbf{S}_a$  is known. To make this filter practical in the clinical environment where  $\mathbf{S}_a$  is not known a priori, we propose a method to find it from  $\mathbf{S}_0$  and  $\mathbf{S}_1$ , which are estimated after image segmentation.

#### 4.2.2 Segmentation to introduce task information

We adopted a segmentation algorithm that makes use of a Markov random field (MRF) model to segment images into two grayscale levels. The core of the method is the adaptive clustering algorithm proposed by Papas, which was applied for images consisting of very few levels [62]. The algorithm begins from development of a model for the posterior probability density function  $p(x|y)$ , where  $y$  is the observed image segmented into regions  $x$ . At the site  $s$  of the image,  $x_s = i$  means that the site belongs to region  $i$ . By Bayes's theorem, we have

$$p(x|y) = p(y|x)p(x),\tag{4.5}$$

where  $p(x)$  is a prior density of the region process, which imposes spatial continuity, and  $p(y|x)$  is the conditional density of the observed image, given the distribution of the regions. It constrains the region magnitude to be close to that of the data. By using MRF, the density of  $x$  is given by a Gibbs density [63,64], while the conditional density is modeled as a white Gaussian process with mean  $\mu_i$  and variance  $\sigma_i^2$  characterizing region  $i$ . The decision is made by MAP rule based on the combined probability density function  $p(x|y)$ . This is done pixel-by-pixel in the whole image and in many iterations until we converge on  $x$ . “*Adaptive*” means parameters  $\mu_i$  and  $\sigma_i^2$  are updated after each iteration.

The algorithm was first used to segment the ultrasound B-mode images by Ashton and Parker [65]. However, the magnitude of conventional B-mode images has a Rayleigh distribution, which does not allow use of this method directly. Therefore, in their work,

Ashton and Parker first decomposed B-mode images into multiple layers (wavelet decomposition), and based on the central limit theorem, they assumed the intensity of pixels at the lowest level has a Gaussian distribution. Segmentation is then applied for each layer from the lowest to the highest resolution. This process is computationally intensive. In our application, we modified the process by segmenting the WFB-mode image instead. There are some advantages to using the Wiener filtered image despite any errors due to variable echo SNR. First, the Wiener filtered data approximates a deconvolution of RF data followed by B-mode rendering. The WFB-mode image has reduced pixel correlation and provides greater region delineation compared with B-mode images. Also, the logarithm of image values is approximately Gaussian distributed as required for segmentation purposes with an acceptable error. Thus, performing segmentation on WFB-mode images simplifies the complexity and shortens computation time. Figure 4.2(a) shows an example of the estimated shape of the variance profile obtained from segmentation and Figure 4.2(b) shows the errors incurred when comparing the segmented image with the exact signal. Segmentation errors reduce the effectiveness of IWFB-mode processing and therefore will adversely affect human observer performance.

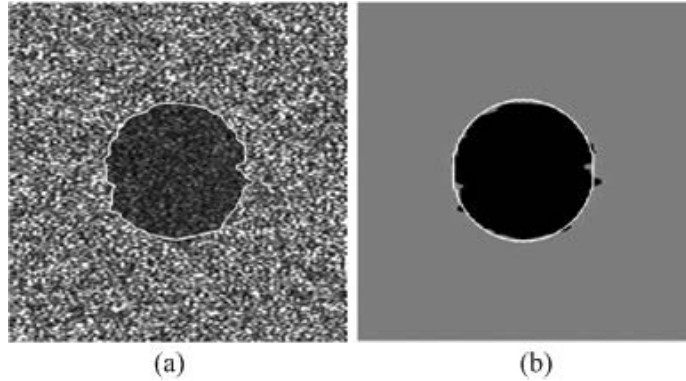


Figure 4.2: Segmentation of the variance profile from the Wiener filtered envelope (a) and its error to compare to the exact signal (b).

The pixel whitening effects of the Wiener filter enable us to consider WFB-mode images as a coarse estimate of the scattering object,  $f(\mathbf{x})$ , so that we can roughly estimate  $\sigma_{\text{obj}}^2$  from the mean square pixel value of the background region.  $\mathbf{S}_i$  may be estimated by measuring the mean-square image value inside the lesion and dividing it by the estimated  $\hat{\sigma}_{\text{obj}}^2$ . However, we modify the process slightly by just dividing the squared magnitude of each pixel inside the lesion by  $\hat{\sigma}_{\text{obj}}^2$ . This modification is made to adapt to the statistical properties of speckled image data inside the lesion region.

Figure. 4.3 shows example images processed three different ways: the standard B-

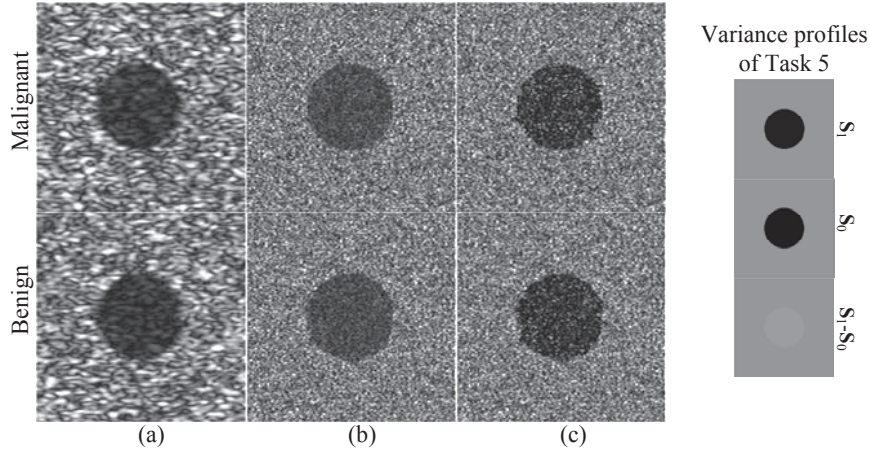


Figure 4.3: Examples of (a) standard B-mode, (b) WFB-mode, and (c) IWFB-mode images of benign and malignant pairs of Task 5 (linear scale) [30].

mode, applying the stationary Wiener filter, and applying the iterative Wiener filter with segmentation before taking the envelope. The main effect of the stationary Wiener filter is to clarify lesion edges, while that of the iterative Wiener filter is to clarify lesion contrast. While the effects apparent in these sample images are subtle, the overall performance improvement for train human observers was significant, as we show below. The disadvantage of the iterative Wiener filter is that it is computational expensive because of segmentation and iterations.

### 4.2.3 Human observer studies

Human observer studies are conducted at the Visual & Image Understanding Laboratory, University of California, Santa Barbara. Humans are shown pairs of standard B-mode images in one study and pairs of Wiener filtered (WFB-mode) or iterative Wiener filtered (IWFB-mode) images in other studies. They are asked to identify the one image with malignant features using the 2AFC testing paradigm [9,26]. Examples of these images are shown in Figure 4.3. Observers also view the signal template in a separate image showing them the malignant feature they are asked to identify.

The goal of this human observer study is to compare different imaging methods to evaluate the effectiveness of post-beamforming spatial filtering of the RF echo signals that is applied before envelope detection. Observers were informed of all feature parameters such as target amplitude and location. After a training period, each observer viewed 400 randomized image pairs per study and the proportion of correct responses,  $P_C$ , was

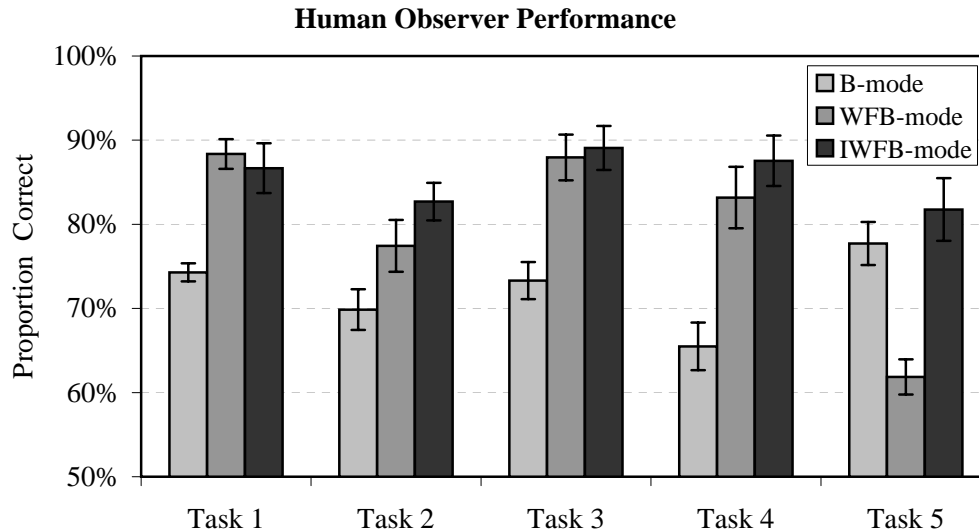


Figure 4.4: Average proportion correct for five human observer studies involving three forms of signal processing as illustrated in Fig. 4.3 and the five diagnostic tasks described in Section 2.1.2. Error bars indicate standard errors [30].

measured. From  $P_C$  we can compute  $d_A$  and AUC metrics. The correctness of each response was immediately indicated. The background-region echo SNR was 32 dB for all simulated images, which was measured experimentally using tissue-like phantoms. Five observers each participated in 15 studies involving five tasks under three imaging conditions labeled B-mode, WFB-mode, and IWFB-mode. Although all images in this study are statistically independent, we controlled for case variability by applying different filters to the same RF data.

Human observer results are summarized in Figure 4.4. We find humans viewing B-mode images for Tasks 1-4 yield the lowest performance compared with images where filtering was applied. Filtering before envelope detection preserves more of the task information that is normally lost at the display stage. Both filters increased human performance about the same amount except for Task 5 where Wiener filtering reduced  $P_C$  substantially from 79% for B-mode images to 63% for WFB-mode images. Task 5 results are examples of what occurs when the linear approximation to the covariance matrix inverse fails to hold. The Wiener filter formed in this way is well matched to the background but not to the interior of the lesion area where the discriminating signal was located. The Wiener filter inappropriately amplified lesion noise, where  $eSNR < 0$  dB (signal is dominated by noise). Because this stationary Wiener filter does not take the task into consideration, it can be expected to enhance human performance only when specific properties of the task are not very important. Meanwhile, the iterative WF significantly improved perfor-

mance for Task 5 because it includes task information estimated from the images in the filter. The IWF performance improvement comes at the cost of approximately fivefold increase in computational load. Variations of the degree of improvements over the five tasks just underscore the task-dependent nature of performance. As designers, we need to understand which clinical exam conditions warrant the extra effort.

## 4.3 Observer efficiency

### 4.3.1 Smith-Wagner observer

The test statistic  $\lambda_B$  derived in (3.19) by Smith and Wagner can be considered as the exact test statistic for the ideal observer on B-mode images for Task 1 [66]. Applying this observer as the ideal observer on B-mode images to other tasks forces us to ignore the violations of the assumptions. Acknowledging these violations, we refer it as the Smith-Wagner (SW) observer. To adapt the SW observer to other tasks, we modify the test statistic to become [26]

$$\lambda_{\text{SW}}(\mathbf{b}) = \mathbf{b}^t(\mathbf{S}_1 - \mathbf{S}_0)\mathbf{b} . \quad (4.6)$$

This model is used to quickly evaluate human observer performance [14]. This observer is similar to the first-order approximation of the IO when it matches the observed data with the task information. In photon imaging [14], it is shown that the observer performance is highly correlated to the human observer. We apply it to all five tasks of breast sonographic diagnosis while acknowledging it is an approximation, albeit the best we have today.

Assuming the utility of the SW observer,  $\eta_H$  defined in (2.24) can be decomposed into

$$\eta_H = \eta_{\text{SW}} \times \eta_{H|\text{SW}} , \quad (4.7)$$

where  $\eta_{\text{SW}}$  is the efficiency of the SW observer acting on envelope images with respect to the ideal observer acting on RF data, and  $\eta_{H|\text{SW}}$  is the efficiency of the human observer with respect to the SW observer, with both acting on B-mode images. Separating efficiency in this manner enables us to identify sources of information loss.  $\eta_{\text{SW}}$  is a measure of information lost by the demodulation process, and  $\eta_{H|\text{SW}}$  is a measurement of information lost by the human-observer system.

### 4.3.2 Post-filtering

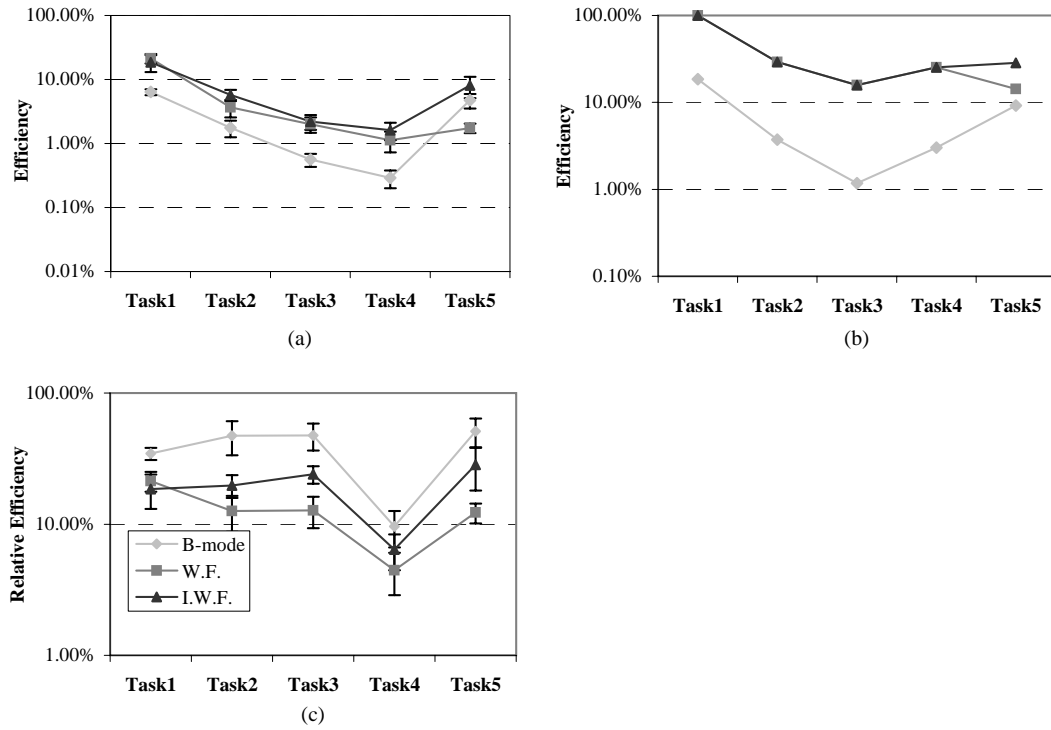


Figure 4.5: (a) Human observer efficiencies measured on B-mode, WFB-mode, and IWFB-mode images,  $\eta_H$  from (2.25). (b) SW observer efficiency,  $\eta_{SW}$ . (c) Human efficiency relative to the SW observer,  $\eta_{H|SW}$ . Values in (a) equal the product of corresponding values from (b) and (c). Note that the ordinate scaling of the relative efficiency axis is changed among the figures [30].

The three efficiencies obtained from the human and ideal observer performance measurements above and that from applying the SW observer to the same data are plotted in Figure 4.5. Part (a) is the efficiency of human observers relative to the ideal observer. It is the product of results in parts (b) and (c) that describe the component efficiencies on the right-hand side of (4.7). Part (a) shows that humans are between 0.2% and 40% efficient at discrimination for the five tasks. Discrimination performance is better for the large-area contrast tasks (1,5) than for the edge-detection tasks (2-4), but there seems to be room for improvement overall. Except for Task 4, where humans struggle to see the spiculated boundary (part (c)), it appears that most of the information is lost in B-mode images during the envelope detection process (part (b)). RF-echo filtering greatly improves the passage of task information through the envelope detection process. Surprisingly, filtering seems to hamper accessibility of task information by humans, but the net effect is that filtering improves human performance for all five tasks. These results

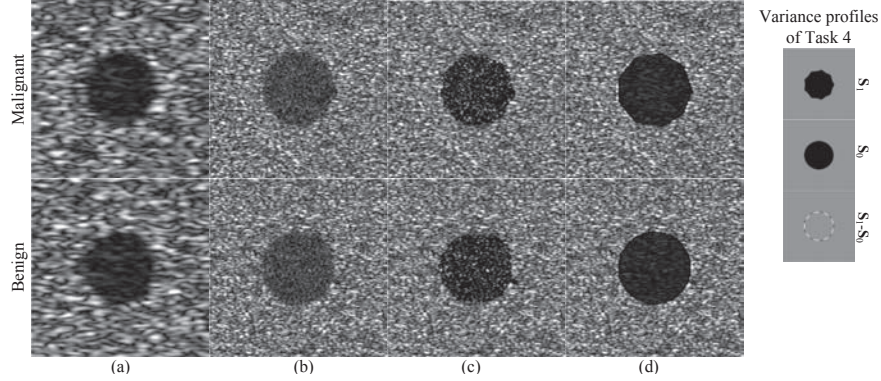


Figure 4.6: Examples of B-mode images for Task 4, including (a) Standard B-mode images; (b) WFB-mode images; (c) IWFB-mode images; and (d) SKEB-mode images.

are very enlightening from a designer’s perspective, because it points to the stage where information is lost and therefore possible solutions.

An example of common lesion segmentation errors is shown in Figure 4.2. The errors can have a large effect on human observer performance. To analyze how the information is lost due to segmentation, we test the iterative Wiener filter under the assumption that we know the underlying variance profiles (SKE paradigm); that is, segmentation is perfect. We name the new envelope as SKEB-mode images. Figure 4.6 shows examples of B-mode images for Task 4, in which (a) is for standard B-mode; (b) is for the the WFB-mode; (c) is for IWFB-mode; and (d) is for SKEB-mode. To compare with the stationary Wiener filter, the iterative Wiener filter reduces the speckle size and enhances the contrast inside the lesion as well. However, it does not improve the shapes of lesions much. The shapes, however, becomes much clearer on the SKEB-mode images.

By using the SW observer, we can quickly evaluate the observer efficiency for the SKEB-mode, and plot it along with other efficiencies on Figure 4.7. The numerical results show that the SW observer performance on SKEB-mode images is comparable to that of the ideal observer over the five tasks. The SW observer efficiency on SKEB-mode images is almost perfect over the five tasks ( $\eta_{SW} \simeq 100\%$ ), reflecting that the error in segmentation is the only source of loss when transferring diagnostic information from RF data to IWFB-mode. Although the SKEB-mode is computed under unrealistic conditions, the substantial increase in efficiency over Tasks 2-5 suggests that the observer performance will be increased with a better segmentation.

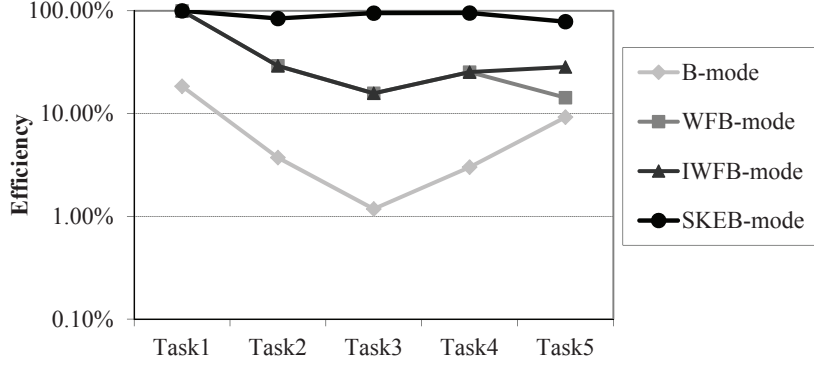


Figure 4.7: The SW observer efficiency over the five tasks on the envelope images, including SKEB-mode.

### 4.3.3 Interpretation of the ideal response

The equivalence of the SW observer performance on SKEB-mode images to the ideal performance shows that the power series expansion in (4.1) effectively converges after one iteration in all five tasks. Or the first-order approximation of the test statistic in (4.3) can be used to make the decision for the ideal observer. Denoting  $\hat{\mathbf{f}} \triangleq \mathbf{H}'\Sigma_a^{-1}\mathbf{g}$  as the iterative Wiener filtered RF data under SKE paradigm, (4.3) can be written as

$$\lambda(\mathbf{g}) \approx \frac{1}{2} \hat{\mathbf{f}}^t \Delta \mathbf{S} \hat{\mathbf{f}}. \quad (4.8)$$

By denoting  $\hat{f}_j = b_{SKE,j} e^{i\phi_j}$  as the  $j^{\text{th}}$  element of column vector  $\hat{\mathbf{f}}$ ,  $\phi_j$  is the phase component of  $\hat{\mathbf{f}}$  at element  $j$ , and  $\mathbf{b}_{SKE}$  is column vector of the IWFB-mode image with SKE, we have

$$\begin{aligned} \lambda(\mathbf{g}) &\approx \frac{1}{2} \hat{\mathbf{f}}^t \Delta \mathbf{S} \hat{\mathbf{f}} = \frac{1}{2} \sum_j \hat{f}_j^* [\Delta \mathbf{S}]_{jj} \hat{f}_j \\ &= \frac{1}{2} \sum_j [\Delta \mathbf{S}]_{jj} b_{SKE,j}^2 = \mathbf{b}_{SKE}^t \Delta \mathbf{S} \mathbf{b}_{SKE}. \end{aligned} \quad (4.9)$$

Thus, the test statistic does not change if the filtered RF data  $\hat{\mathbf{f}}$  is replaced with its envelope  $\mathbf{b}_{SKE}$ . This equivalence provides us an interpretation of the ideal observer response as it counts the speckle spots on SKEB-mode images within the signal difference area  $\mathbf{S}_1 - \mathbf{S}_0$ , which is vital to decision making. By assuming speckles have identical probability distributions, the test statistic follows a normal distribution if the number of those speckles is large enough. This conclusion verifies the conjecture in Chapter 3 on the normality condition of sonographic tasks. In Tasks 1, 3, and 5, where the task difference

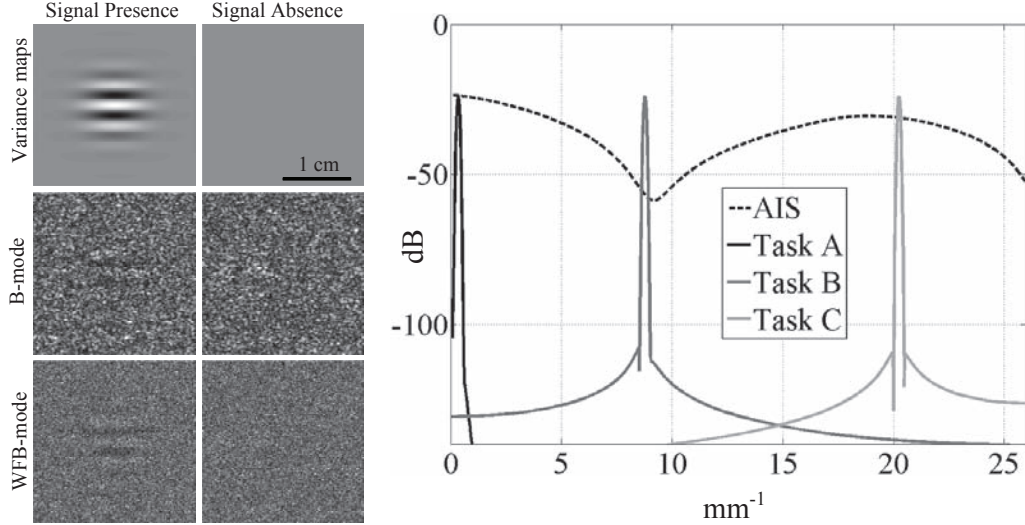


Figure 4.8: (Left) Variance maps of the sine-wave detection task (Top); the B-mode images generated from the variance maps (middle); and the corresponding WFB-mode (bottom) images. (Right) The AIS with task information over the axial spatial frequency. Task A is at  $0.35 \text{ mm}^{-1}$  corresponding to the map variance in the left; Task B is at  $8.77 \text{ mm}^{-1}$ ; and Task C is at  $20.24 \text{ mm}^{-1}$ .

is large, the test statistic is normally distributed (central limit theorem). However, the condition is lost in Tasks 2 and 4 where the signal difference is small. The number of speckles that falls into the task difference area is not big enough to invoke the central limit theorem.

#### 4.3.4 Information spectrum on B-mode images

The AIS curve developed in Chapter 3 only addresses the information conveyed in the RF data at the acquisition stage. It does not include the display stage where RF signals are demodulated to form B-mode images. In this section, we investigate how information is lost through the demodulation process as a function of spatial frequency. The only computational tool we have to assess the B-mode image quality is the Smith-Wagner observer. Yet, its response is not the exact log-likelihood ratio on B-mode images; therefore, we only can analyze the information loss in terms of task information. Specifically, we challenge the observers with sine-wave detection tasks. Those tasks were originally designed to determine the ability of the human observer to access phase information [67].

The sine-wave signal is generated by using the Gabor pulse and its detection task is set in the context of 2AFC experiments. The variance map is shown in Figure 4.8(left,top). From those maps, the task spectrum is generated and plotted in Figure 4.8(right) as Task

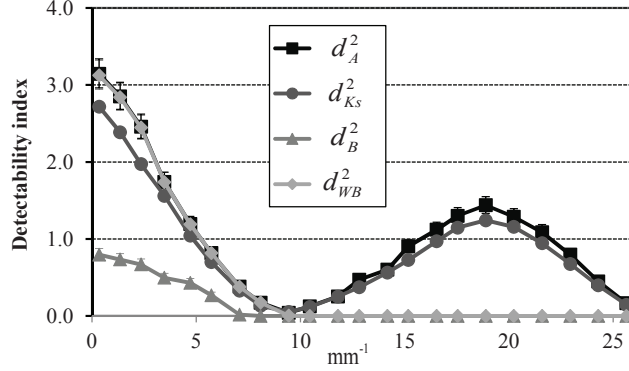


Figure 4.9: Comparison detectability indices of  $d_A^2$  converted from area under ROC of the ideal observer,  $d_{K_s}^2$  calculated from (3.32), and  $d_B^2$  and  $d_{WB}^2$  calculated from the performance of the Smith-Wagner observer.

A. The AIS curve is also plotted in the figure (the dashed line). With a narrow band response, the task information is similar to a Dirac delta function. Multiplying it by the AIS and integrating over frequency as in (3.32) is similar to sampling AIS at the spatial frequency associated with Task A. By increasing the frequency of the Gabor pulse in the variance map, we can sample AIS at different values of the spatial frequency (Tasks B and C). Those tasks allow us to map AIS discretely in terms of  $d_{K_s}^2$ .

From each pair of variance maps, we generate 2000 pairs of RF signals for calculating the ideal observer performance in Monte Carlo studies. The ideal performance is then converted to  $d_A^2$  for comparison with  $d_{K_s}^2$ . Since the AIS curve is derived for low-contrast detection, the amplitude of the Gabor pulse is set to be  $-25$  dB relative to the background so that the first-order approximation of (3.36) is not violated with variations of the pulse magnitude. Both  $d_A^2$  and  $d_{K_s}^2$  are plotted in Figure 4.9 for comparison. Both curves have two peaks and one valley at the same locations. The first peak is at origin while the second one is at  $18.89 \text{ mm}^{-1}$ . The detectability index minimum is nearly at a spatial frequency of  $9.44 \text{ mm}^{-1}$ . The frequency at the minimum depends on the bandwidth and center frequency of the ultrasound pulse.  $d_{K_s}^2$  is usually 7-9% lower than  $d_A^2$ , relative to its magnitude. This corresponds to an error of 1-2% in ideal observer performance. The consistency between  $d_A^2$  and  $d_{K_s}^2$  validates the shape of AIS plotted in Figure 4.8.

To understand the information lost through demodulation, we take the envelope of RF data to form B-mode images. Performance over the envelope images is evaluated by using the Smith-Wagner observer. The performance is then converted to  $d_B^2$  for comparison with  $d_A^2$ . The Wiener filter has been applied to RF data to evaluate its ability to recover the information loss over the frequency. Since the tasks are all low-contrast detections, we do

not need to use the iterative Wiener filter. The SW observer is also applied to WFB-mode images and its performance is converted to  $d_{WB}^2$ . Examples of B-mode and WFB-mode images are shown in Figure 4.8(middle and bottom). The detectability indices  $d_B^2$  and  $d_{WB}^2$  are plotted in Figure 4.9.

From the figure,  $d_B^2$  is only about 25% of  $d_A^2$ , suggesting that 75% of information is lost through demodulation. The shape of  $d_B^2$  is similar to that of NEQ in photon imaging (Figure 3.6). It goes to zero for all frequencies greater than  $7 \text{ mm}^{-1}$ . We explain this result by noting the spatial resolution of B-mode images is limited by the size of the speckle. And the speckle size prevents all information at a spatial resolution less than  $7 \text{ mm}^{-1}$  from being visualized. By Wiener filtering, we can recover the information at the first lobe of the AIS curve.  $d_{WB}^2$  is identical to  $d_A^2$  and they go to zero at  $9 \text{ mm}^{-1}$ . The Wiener filter is very effective on low-contrast detection tasks; but even so, the information content in WFB-mode cannot be higher than that in the raw RF data. Once  $d_{WB}^2$  reaches zero, it cannot increase, because the spatial resolution of WFB-mode images is limited by the speckle size (after decorrelation), just as it is with B-mode images. Thus, the Wiener filter only can recover information in the first lobe of AIS. How to recover information in the second lobe of the AIS remains a topic for future investigation.

## 4.4 Experimental implementation

In this section, we demonstrate the concepts of Wiener and iterative Wiener filters on a commercial system and experimental data by imaging a tissue-mimicking phantom. Those filters include a realistic, shift-variant model for the system impulse response.

### 4.4.1 Line spread function

Filtering was applied to echo data acquired from the SONOLINE Antares system with a VF10-5 transducer. System parameters were nominally the same as those applied to the simulations. Data are recorded without applying time-gain-compensation. We still use a fixed-focused beam for both transmitting and receiving with a focal length of 40 mm and no apodization. The configuration helps show the dependence of the speckle area on image depth and the improvement that is seen when Wiener filtering is applied. The system was used to image a cyst phantom (Model #539, ATS Laboratories, Bridgeport, CT). The manufacturer-reported speed of sound in the phantom is  $1450 \text{ m/s}$  and the attenuation coefficient slope is  $0.5 \text{ dB cm}^{-1} \text{ MHz}^{-1}$ . The delay and sum beamformed

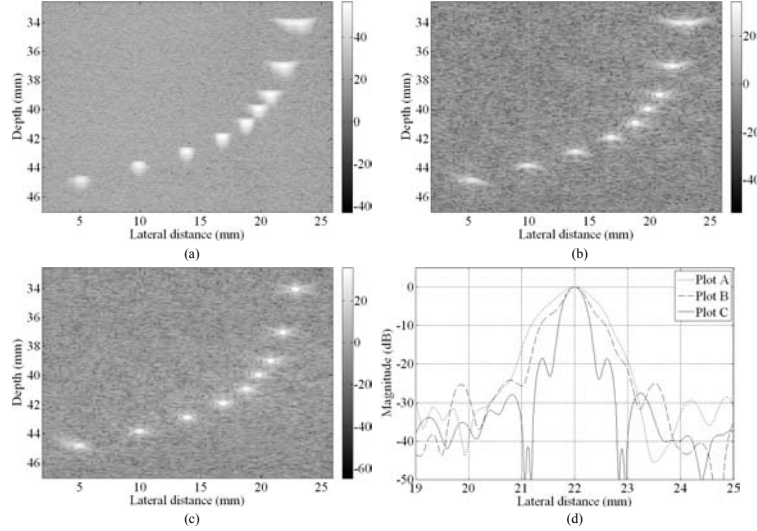


Figure 4.10: Log-compressed images for a line target phantom measured using the SONOLINE Antares system at 7 MHz. (a) B-mode image, (b) WFB-mode image with shift-invariant impulse response assumed, (c) WFB-mode image with shift-variant impulse response assumed and the multi-LSF filter applied, and (d) the plots of three lateral lines (normalized) across the target at the depth of 37 mm, in which plot A is for the B-mode image in (a), plot B is for the WFB-mode image in (b) with shift-invariant impulse response, and plot C is for the WFB-mode image in (c) with shift-variant impulse response [30].

echo SNR in the phantom was measured to be 32 dB near the 40-mm focal length.

The Wiener filter was developed using the measured line-spread function (LSF), which is the pulse-echo impulse response integrated over the elevational axis. The line scatterers are of 0.12 mm diameter nylon monofilament. Since phantom objects are two dimensional (line and cylinder inclusions oriented to give point and circular targets in the scan plane), the LSF is most appropriate to use in the system matrix  $\mathbf{H}$  of the Wiener filter.

The LSF varied with depth as shown in the B-mode image of Figure 4.10(a), which is used to investigate the shift-variant impulse responses for Wiener filtering. For the shift-invariant impulse response,  $\mathbf{H}$  is assumed to be a circulant matrix for experiment data and composed from a single LSF recorded from a line scatterer positioned at the 40-mm focal length. For the shift-variant impulse response,  $\mathbf{H}$  is composed from five LSFs recorded at regular 2 mm intervals between 34 and 45 mm distances (2 mm *isoplanatic* patches). Applying the method described in Appendix C, a Wiener filter for a shift-variant system was formed. To reduce LSF noise to negligible levels for filter development, we recorded and time-averaged 1000 frames from stationary line scatterers.

Figures 4.10(b,c) show WFB-mode images for filters made assuming shift-invariant and shift-variant systems, respectively. While the impulse response of the B-mode image

in Figure 4.10(a) is strongly depth-dependent, the WFB-mode image in Fig. 4.10(b) shows improved spatial resolution near the 40 mm focal length. However, the shift-variant filter used in the image of Figure 4.10(c) demonstrates a more uniform and improved spatial resolution. Nevertheless, deconvolution remains incomplete because of low-level side-lobe energy.

#### 4.4.2 Cyst Phantom Experiment

The same two Wiener filters were applied to an 8 mm diameter, anechoic, circular target in the phantom that was positioned at a depth of 40 mm. The B-mode image is shown in the upper left corner of Figure 4.11, where speckle correlation area is large and nonuniform over the plane. Average speckle size is reduced in the WFB-mode image (upper right) filtered by only one LSF recorded at 40 mm depth. However, speckle is not spatially uniform, and the cyst boundary is distorted because the RF data is filtered with an unmatched LSF. The WFB-mode image generated with multiple shift-variant LSFs (bottom left) has a more circular boundary and uniform small speckle, but at the cost of increased computation (see Appendix C). Finally, the corresponding IWFB-mode image (bottom right) has enhanced contrast and is able to most clearly represent a cyst-like target. Segmentation errors tend to erode the margin and suggest a more complicated boundary than the simple circle we know is present.

### 4.5 Discussion

The ideal observer approximation is extended to improve visual discrimination for high-contrast features by introducing an iterative Wiener filter. IWFB-mode images decorrelate speckle, as do WFB-mode images, but are able to better preserve contrast resolution for contrast-limited tasks, e.g., Task 5. The human-observer performance studies show that the IWF provides the same high discrimination level as the stationary WF for a low-contrast large-area detection task (Task 1), and three boundary discrimination tasks (Tasks 2-4). However, the IWF significantly improves visual discrimination efficiency for a high-contrast large-area task (Task 5), where echo non-stationarity from object heterogeneity degrades the stationary WF. The improvement in performance comes at the cost of approximately fivefold increase in computational load (the IWFB-modes require 20 s on a dual-core PC, 2.13 GHz Processor, 2G RAM). The performance of the IWF depends solely on the error in the segmentation to extract the breast lesion from the

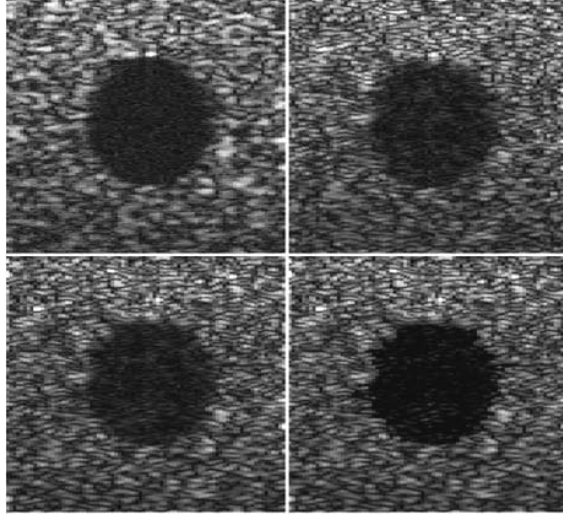


Figure 4.11: Images of a cyst-like, 8 mm circular target centered at a 40 mm depth for a commercial system (linear scale). Standard B-mode image (upper-left), WFB-mode image with shift invariant  $\mathbf{H}$  (upper right), WFB-mode image with shift variant  $\mathbf{H}$  (lower left), and IWFB-mode image (lower right) [30].

background.

The deconvolution methods improve feature discriminations because the density of independent image samples available to observers increases as the average speckle area is reduced. The additional information is helpful for contrast-limited large-area Tasks 1 and 5 as well as those involving resolution-limited edge discrimination, Tasks 2-4. The Wiener filter produces significant improvements when the impulse response is known exactly and the image data are from a wide-sense stationary distribution. The Wiener filter fails when the assumptions are violated, as occurred with the Wiener filter in Task 5, and yet it is robust enough for use with commercial systems. Performance improves across all five tasks for IWFB-mode images because we added task-specific information in filter development when it was necessary. We strive to develop beamformers that are fast and robust across the wide spectrum of clinical features, and yet can adapt when necessary to special conditions. The ideal observer approach provides a framework for that development.

Human visual discrimination efficiency for the five lesion features considered is less than 10% for B-mode imaging. Spatial filtering was found to improve the transfer of object information into the image data, but it reduces somewhat the ability of humans to access the information. Thus there is a potential role for image processing of the final envelope image to increase accessibility. Note that the Smith-Wagner observer [20] was

developed as the ideal observer for Task 1 but is unlikely to perform optimally for other tasks.

In combination with sine-wave detection tasks, the SW observer also allows us to observe the loss of information on the AIS curve when data is demodulated through the final B-mode image. The demodulation reduces the squared detectability index to 25% relative to those of the ideal observer on the main lobe of the AIS while disabling all information in the other lobe. By Wiener filtering before demodulation, we can fully recover the information at the main lobe, but could not obtain any information in the other two side-lobes of the curve.

Task performance of spatial-filter beamformers is improved significantly by including any shift variance in the pulse-echo impulse response in the filter as seen in the phantom experiments. The greatest challenge when applying this method in the clinical environment is to estimate accurately the pulse-echo impulse response for the Wiener filter. However, it is very difficult to measure the impulse response function for commercial systems, because this function is affected by phase aberrations, imperfection of transducers, and undesirable artifacts inside the systems. In this research, we found that a line-spread function can be used to develop Wiener filters in place of the impulse response when imaging cylindrical objects. Accurate estimation of point-spread functions throughout the field will be needed to improve clinical imaging. Loss of visual discrimination from an inaccurate point-spread function is also an interesting topic and motivates further study.

For any pulse-echo experiment, the most effective processing – from the perspectives of both an optimal Bayesian observer (information transfer) and from psychophysically measured human observer performance – requires detailed knowledge of the system impulse response to decorrelate RF signals and thereby reduce the effects of speckle in the resulting image.

# CHAPTER 5

## BEAMFORMING

### 5.1 Introduction

Currently, the delay-and-sum (DS) beamformer is a standard method used by most commercial ultrasound imaging systems. Signals from received channels in the array aperture are delayed and summed to form an A-scan line. The beamformer is optimal, provided that RF signals are sampled on those channels without any distortion or blurring [68]. With the presence of the pulse-echo spatiotemporal impulse responses at transducer elements, however, ultrasonic systems fail to meet this ideal condition. The image quality achievable with the DS beamformer, therefore, is fundamentally limited by loss of coherence among RF signals, which lowers eSNR and degrades spatial and contrast resolutions. In such a case, filtering operators can be incorporated into the DS to improve performance [69].

Advances in computational speed make it realistic to consider applying complex filtering operators in real-time in combination with the DS [56]. Among them, the minimum-variance (MV) beamformer is prominent as applied to breast sonography. Several investigations have found improvements in spatial and contrast resolutions using the MV approach [70–77]. This method was pioneered by Capon for seismic applications as a high-resolution method for estimating the frequency-wavenumber power spectral density [78]. The goal of the MV beamformer is to select receive-channel filters that minimize the weighted array power output in all directions except along the beam axis. The MV beamformer can be derived using several approaches, and the results have many names, including linear constrained minimum variance (LCMV), minimum variance distortionless response (MVDR), minimum power distortionless response (MPDR), and adaptive beamforming [68, 76]. However, if physical parameters of the system are known exactly, they all lead us to the same solution.

---

Portions of this chapter are reprinted, with permission, from N.Q. Nguyen, C.K. Abbey, and M.F. Insana, “Analysis of minimum-variance and Wiener-Filtered beamforming strategies,” in *Proceedings of the IEEE Ultrasonics Symposium* (in press), © 2011 IEEE.

The MV beamformer can be followed by a scalar filter to form the minimum mean square error (MMSE) beamformer, which generates the MMSE estimate of the input signal. The MMSE beamformer is derived as an optimal linear processor. If both signal and noise vectors are Gaussian processes, it becomes the best processor, surpassing even nonlinear ones [68, 79]. Recently, the MMSE was applied to sonography in terms of a Wiener beamformer, and found to improve contrast resolution compared with the MV approach, especially under low echo-signal-to-noise (eSNR) conditions [80].

Although both MMSE and MV beamformer were shown to improve image quality metrics, there remains a larger question of how to predict and compare their performance for achieving diagnostic objectives. In this chapter, we propose using ideal Bayesian observer analysis as a basis for beamformer design and evaluation, which builds upon our initial development in [31]. One advantage of the ideal observer methodology is its ability to relate sonographic instrument properties (resolution and noise figures) directly to observer performance for features that can be specified exactly [26, 30] (see Chapter 3). Observers are trained humans or algorithms that evaluate criteria according to the rules of decision theory. Another advantage of this approach is the ability to track task information flow through the image formation and diagnostic processes. Since the ideal observer provides an upper bound for task performance, comparisons with practical-observer performance define the efficiency of each beamformer to maximize the information content in the image accessible by observers.

In subsequent sections, the MV beamformer is expressed as a first-order approximation to the ideal observer strategy. It is decomposed into two operators. The first operator applies a matched filter (MF) to each receive-channel signal that is composed of the channel's pulse-echo impulse response. This operator helps compress data without losing any diagnostic information. After summation, the compressed RF echoes are applied by the second operator, which actually is an inverse filter, prior to envelope detection. The goal of the second operator is to preserve the diagnostic information through demodulation. In efforts to improve upon the first-order approximation, the MMSE beamformer has emerged. Since it has the form of the Wiener filter, we name it the Wiener filtered (WF) beamformer. Through our framework, the performance of each beamformer can be predicted and compared with others based on the conditions of the tasks and system properties, for which the first-order approximations hold. Their performances are then measured for over five discrimination tasks involving breast lesion features. The results varied predictably depending on the nature of the task and on how well each beamformer was able to approximate the strategy of the ideal observer for the task.

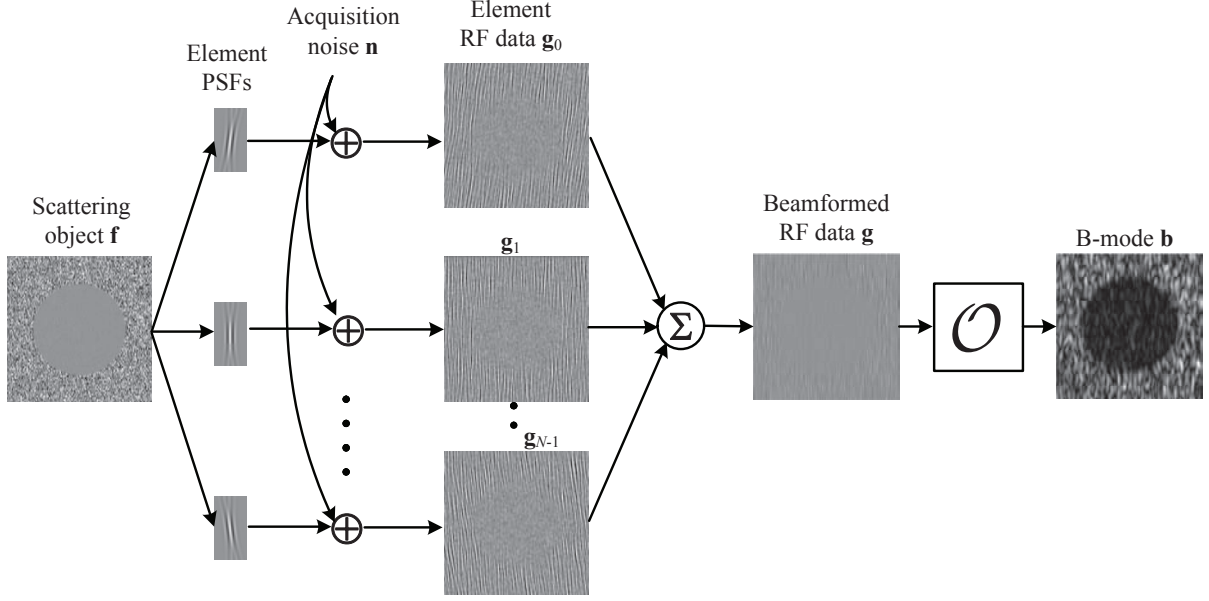


Figure 5.1: A graphical model for image formation that includes beamforming. The acquisition stage is extended to each element of the transducer where the data are initially acquired [31].

## 5.2 Ideal observer approach to beamformers

### 5.2.1 System model for transducer element signals

The image formation model for beamforming is graphically illustrated in Figure 5.1, where the acquisition operator  $\mathcal{H}$  in Figure 2.7 is extended to describe individual received elements of the linear array transducer. Consequently, the imaging equation in (2.2) becomes

$$\mathbf{g}_T = \begin{bmatrix} \mathbf{g}_0 \\ \mathbf{g}_1 \\ \vdots \\ \mathbf{g}_{N-1} \end{bmatrix} = \begin{bmatrix} \mathbf{H}_0 \\ \mathbf{H}_1 \\ \vdots \\ \mathbf{H}_{N-1} \end{bmatrix} \mathbf{f} + \begin{bmatrix} \mathbf{n}_0 \\ \mathbf{n}_1 \\ \vdots \\ \mathbf{n}_{N-1} \end{bmatrix} = \mathbf{H}_T \mathbf{f} + \mathbf{n}_T, \quad (5.1)$$

where  $\mathbf{g}_T$  is a vector of RF echo signals from all receive channels before delay and summation.  $\mathbf{H}_i$  is the multiplication matrix at element  $i$  and  $\mathbf{H}_T$  is a combination of multiplication matrices from all transducer elements for generating pre-beamformed RF data  $\mathbf{g}_T$ .  $\mathbf{n}_T$  is the acquisition noise. Assuming noise on the  $i^{\text{th}}$  channel is an independent and identical WGN process with variance  $\sigma_{n,T}^2$ , the variance of the beamformed noise signal is  $\sigma_n^2 = N\sigma_{n,T}^2$ , where  $N$  is the number of elements in the receive aperture. Denoting  $\mathcal{B}$

as a beamforming operator, we can write

$$\mathbf{g} = \mathcal{B}\mathbf{g}_T \quad \text{and} \quad \mathbf{H} = \mathcal{B}\mathbf{H}_T ,$$

where  $\mathbf{g}$  and  $\mathbf{H}$  are the RF data and system matrix after beamforming, respectively. If  $\mathcal{B}$  is a linear operator, we can write the beamforming process in terms of matrix multiplications as

$$\mathbf{g} = \mathbf{H}\mathbf{f} + \mathbf{n} , \quad \text{where} \quad \mathbf{g} = \mathbf{B}^t\mathbf{g}_t , \quad \mathbf{H} = \mathbf{B}^t\mathbf{H}_T , \quad \text{and} \quad \mathbf{n} = \mathbf{B}^t\mathbf{n}_T . \quad (5.2)$$

In (5.2),  $\mathbf{B}^t$  is used instead of  $\mathbf{B}$  to be consistent with notations used in the beamforming literature.

Each lesion feature has a unique benign-malignant signature pair that are labeled  $i = 0$  or 1, respectively. The probability density function (pdf) of object scattering for the  $i^{\text{th}}$  class of data is still modeled by a zero-mean, uncorrelated, nonstationary, multivariate normal process:

$$p_i(\mathbf{f}) = \text{MVN}(\mathbf{0}, \sigma_{\text{obj}}^2(\mathbf{I} + \mathbf{S}_i)) \quad \text{for } i = 0, 1 . \quad (5.3)$$

$\sigma_{\text{obj}}^2(\mathbf{I} + \mathbf{S}_i)$  is the covariance matrix,  $\mathbf{I}$  is the identity matrix, and diagonal matrix  $\mathbf{S}_i$  defines deviations in uniform background tissue scattering that specify features of the  $i^{\text{th}}$  class. The pdf for pre-beamformed RF data  $\mathbf{g}_T$  underlying  $H_i$  is given by

$$p_i(\mathbf{g}_T) = \text{MVN}(\mathbf{0}, \boldsymbol{\Sigma}_{T,i}) \quad \text{for } i = 0, 1 , \quad (5.4)$$

where

$$\boldsymbol{\Sigma}_{T,i} = \sigma_{\text{obj}}^2 \mathbf{H}_T (\mathbf{I} + \mathbf{S}_i) \mathbf{H}_T^t + \boldsymbol{\Sigma}_n , \quad (5.5)$$

which is the covariance matrix of the pre-beamformed echo RF signals.  $\boldsymbol{\Sigma}_n = \sigma_{T,n}^2 \mathbf{I}$ , but the size of  $\mathbf{I}$  is much larger to accommodate the size of  $\mathbf{g}_T$ .

The ideal observer's strategy for distinguishing the two classes of data is described by a test statistic given as the log-likelihood ratio,

$$\lambda(\mathbf{g}_T) = \ln \frac{p_1(\mathbf{g}_T)}{p_0(\mathbf{g}_T)} \longrightarrow \frac{1}{2} \mathbf{g}_T^t (\boldsymbol{\Sigma}_{T,0}^{-1} - \boldsymbol{\Sigma}_{T,1}^{-1}) \mathbf{g}_T . \quad (5.6)$$

The right side of (5.6) is formed by eliminating additional terms that do not depend on  $\mathbf{g}_T$ . In following sections, the ideal observer test statistic is explored to find beamforming strategies for  $\mathbf{g}_T$ .

## 5.2.2 Ideal observer exploration

The beamforming strategy of the ideal observer is hidden within the compact expression of (5.6). We can obtain insights by applying the *Woodbury matrix inverse identity* [8] to the inverse of covariance matrices as given by

$$(\mathbf{A} + \mathbf{BCD})^{-1} = \mathbf{A}^{-1} - \mathbf{A}^{-1}\mathbf{B}(\mathbf{C}^{-1} + \mathbf{DA}^{-1}\mathbf{B})^{-1}\mathbf{DA}^{-1}, \quad (5.7)$$

provided matrices  $\mathbf{A}$  and  $\mathbf{C}$  are invertible.

Applying (5.7) to the expression for  $\Sigma_{T,i}^{-1}$  in (5.5) ( $i = 0,1$ ), we obtain

$$\Sigma_{T,i}^{-1} = \Sigma_n^{-1} - \sigma_{\text{obj}}^2 \Sigma_n^{-1} \mathbf{H}_T \left( (\mathbf{I} + \mathbf{S}_i)^{-1} + \sigma_{\text{obj}}^2 \mathbf{H}_T^t \Sigma_n^{-1} \mathbf{H}_T \right)^{-1} \mathbf{H}_T^t \Sigma_n^{-1}. \quad (5.8)$$

By setting  $\mathbf{K}_n \triangleq \sigma_{\text{obj}}^2 \mathbf{H}_T^t \Sigma_n^{-1} \mathbf{H}_T$  and  $\Psi_i = (\mathbf{I} + \mathbf{S}_i)^{-1} + \mathbf{K}_n$ , the test statistic becomes

$$\lambda(\mathbf{g}_T) = \frac{\sigma_{\text{obj}}^2}{2} \mathbf{g}_T^t \Sigma_n^{-1} \mathbf{H}_T (\Psi_1^{-1} - \Psi_0^{-1}) \mathbf{H}_T^t \Sigma_n^{-1} \mathbf{g}_T. \quad (5.9)$$

The expanded expression for  $\lambda(\mathbf{g}_T)$  in (5.9) reveals the first strategy of the ideal observer for beamforming. The term  $\mathbf{H}_T^t \Sigma_n^{-1} \mathbf{g}_T$  is recognized as the matched filtering of  $\mathbf{g}_T$  provided the acquisition noise is stationary and uniform,  $\Sigma_n = \sigma_{n,T}^2 \mathbf{I}$ . For the highly rectangular shape of  $\mathbf{H}_T$ , multiplying pre-beamformed RF data by its transpose allows us to compress the volume data into a column vector of the A-scan line's dimension. Besides, we realize in (5.9) that  $\mathbf{g}_T^t \Sigma_n^{-1} \mathbf{H}_T = (\mathbf{H}_T^t \Sigma_n^{-1} \mathbf{g}_T)^t$ , thus, the IO test statistic can be computed through the matched filtered RF data  $\mathbf{g}_T$ . The form of  $\lambda(\mathbf{g}_T)$  in (5.9) reveals that the ideal performance is preserved through the matched filtering operator, although it is an irreversible process which compresses the data. Matched filtering, however, only preserves the information up to the end of the acquisition stage. There is no guarantee that information will survive demodulation to arrive intact in the B-mode image in a form accessible by observers. In fact, there is a significant loss of task performance if the envelope image is computed immediately after matched filtering. In our initial development, numerical studies for matched filtered (MF) beamformed RF data over five discrimination tasks show that the information left after demodulation range from 10% in Task 1 to 1.6% in Task 2 [31].

We showed in (4.9) that if the ideal observer response can be factorized in terms of a filtered RF signal squared and the task information, the response remains unchanged if the RF is replaced by its envelope. This equation means that ideal performance is preserved through demodulation. Therefore, in the following step, we decompose the

matrix coefficient  $\Psi_1^{-1} - \Psi_0^{-1}$  in (5.9) into the task information and an operator applying to MF beamformed RF data. The decomposition usually requires some approximations due to the acquisition noise in RF data.

### 5.2.3 Approximations to the ideal strategy

By assuming the columns of  $\mathbf{H}_T$  are linearly independent or  $\mathbf{K}_n$  is invertible, we apply (5.7) to  $\Psi_i$  in (5.9) and find

$$\Psi_i^{-1} = \mathbf{K}_n^{-1} - \mathbf{K}_n^{-1} (\mathbf{K}_n^{-1} + \mathbf{I} + \mathbf{S}_i)^{-1} \mathbf{K}_n^{-1} . \quad (5.10)$$

Substituting (5.10) into (5.9), we have

$$\lambda(\mathbf{g}_T) = \frac{\sigma_{\text{obj}}^2}{2} \mathbf{g}_T^t \mathbf{H}_T \Sigma_n^{-1} \mathbf{K}_n^{-1} (\Phi_0^{-1} - \Phi_1^{-1}) \mathbf{K}_n^{-1} \mathbf{H}_T^t \Sigma_n^{-1} \mathbf{g}_T , \quad (5.11)$$

where  $\Phi_i = \mathbf{I} + \mathbf{K}_n^{-1} + \mathbf{S}_i$  and  $i = 0$  or  $1$ .

The ideal observer test statistic in (5.11) can be explored further by adopting the first-order approximation  $(\mathbf{I} + \mathbf{A})^{-1} \simeq \mathbf{I} - \mathbf{A}$  to calculate  $\Phi_i^{-1}$  [26], where  $\mathbf{A} \triangleq \mathbf{K}_n^{-1} + \mathbf{S}_i$ . By doing so, we obtain

$$\Phi_i^{-1} \simeq \mathbf{I} - (\mathbf{K}_n^{-1} + \mathbf{S}_i) , \quad (5.12)$$

and

$$\begin{aligned} \lambda(\mathbf{g}_T) &\simeq \frac{\sigma_{\text{obj}}^{-2}}{2} \mathbf{g}_T^t \mathbf{H}_T \Sigma_n^{-1} (\mathbf{H}_T^t \Sigma_n^{-1} \mathbf{H}_T)^{-1} (\mathbf{S}_1 - \mathbf{S}_0) (\mathbf{H}_T^t \Sigma_n^{-1} \mathbf{H}_T)^{-1} \mathbf{H}_T^t \Sigma_n^{-1} \mathbf{g}_T \\ &= \frac{\sigma_{\text{obj}}^{-4}}{2} \mathbf{g}_T^t \mathbf{B}_{MV} \Delta \mathbf{S} \mathbf{B}_{MV}^t \mathbf{g}_T , \end{aligned} \quad (5.13)$$

where  $\Delta \mathbf{S} = \sigma_{\text{obj}}^2 (\mathbf{S}_1 - \mathbf{S}_0)$  is the task information and  $\mathbf{B}_{MV} = \Sigma_n^{-1} \mathbf{H}_T (\mathbf{H}_T^t \Sigma_n^{-1} \mathbf{H}_T)^{-1}$  is recognized as the MV beamformer [68]. Details on the form of this beamformer are discussed in the next section. The first-order approximation in (5.13) describes MV beamformed echo signals  $\mathbf{B}_{MV}^t \mathbf{g}_T$  that are squared and multiplied by the task information. Equation (5.13) suggests an MV beamformer should be applied to RF data  $\mathbf{g}_T$  for maximizing diagnostic information through demodulation provided the first-order approximation in (5.12) is valid.

The approximation can be improved with a new decomposition of  $\Phi_i = (\mathbf{K}_n^{-1} + \mathbf{I}) + \mathbf{S}_i$ . Consequently,

$$\Phi_i^{-1} \approx (\mathbf{K}_n^{-1} + \mathbf{I})^{-1} - (\mathbf{K}_n^{-1} + \mathbf{I})^{-1} \mathbf{S}_i (\mathbf{K}_n^{-1} + \mathbf{I})^{-1} , \quad (5.14)$$

and

$$\Phi_0^{-1} - \Phi_1^{-1} \approx (\mathbf{K}_n^{-1} + \mathbf{I})^{-1}(\mathbf{S}_1 - \mathbf{S}_0)(\mathbf{K}_n^{-1} + \mathbf{I})^{-1}. \quad (5.15)$$

Substituting (5.15) into (5.11), we obtain

$$\begin{aligned} \lambda(\mathbf{g}_T) &\approx \frac{\sigma_{\text{obj}}^2}{2} \mathbf{g}_T^t \Sigma_n^{-1} \mathbf{H}_T \mathbf{K}_n^{-1} (\mathbf{K}_n^{-1} + \mathbf{I})^{-1} (\mathbf{S}_1 - \mathbf{S}_0) (\mathbf{K}_n^{-1} + \mathbf{I})^{-1} \mathbf{K}_n^{-1} \mathbf{H}_T^t \Sigma_n^{-1} \mathbf{g}_T \\ &= \frac{\sigma_{\text{obj}}^2}{2} \mathbf{g}_T^t \mathbf{H}_T (\sigma_{\text{obj}}^2 \mathbf{H}_T^t \mathbf{H}_T + \sigma_n^2 \mathbf{I})^{-1} (\mathbf{S}_1 - \mathbf{S}_0) (\sigma_{\text{obj}}^2 \mathbf{H}_T^t \mathbf{H}_T + \sigma_n^2 \mathbf{I})^{-1} \mathbf{H}_T^t \mathbf{g}_T \\ &= \frac{1}{2} \mathbf{g}_T^t \mathbf{B}_{WF} \Delta \mathbf{S} \mathbf{B}_{WF}^t \mathbf{g}_T, \end{aligned} \quad (5.16)$$

in which the second expression is obtained by using  $\Sigma_n = \sigma_n^2 \mathbf{I}$  and  $\mathbf{K}_n = \sigma_{\text{obj}}^2 \mathbf{H}_T^t \mathbf{H}_T / \sigma_n^2$ .

In (5.16),  $\mathbf{B}_{WF}^t = (\sigma_{\text{obj}}^2 \mathbf{H}_T^t \mathbf{H}_T + \sigma_n^2 \mathbf{I})^{-1} \mathbf{H}_T^t$  has the form of the Wiener filter. We name it Wiener-filtered (WF) beamformer. Similarly to the case of the MV beamformer, (5.16) suggests a WF beamformer should be applied to the RF data provided the first-order approximation in (5.14) is valid.

Thus, we have shown that MV and WF beamformers are both approximations of the ideal strategy. In both cases, they spatially decorrelate the RF echo signals before demodulation, which preserves more task information as compared to the delay-and-sum (DS) and matched filter (MF) beamformers. Based on the analysis, we predict that the WF beamformer outperforms the MV beamformer if the eigenvalues of  $\mathbf{K}_n^{-1}$  are large. The requirement that the inverse of  $\mathbf{K}_n$  exist and be well conditioned challenges the experimental validation of our analysis. A full treatment is provided in Appendix D, Section D.1.

## 5.3 Connections to other studies

### 5.3.1 Minimum variance beamformer

$\mathbf{B}_{MV}$  in (5.13) can be derived as the minimum variance distortionless response (MVDR) beamformer [68]. To see that, we combine the matrix  $\mathbf{B}^t$  into the imaging equation to obtain

$$\mathbf{B}^t \mathbf{g}_T = \mathbf{B}^t \mathbf{H}_T \mathbf{f} + \mathbf{B}^t \mathbf{n}_T. \quad (5.17)$$

The constraint of no distortion implies  $\mathbf{B}^t \mathbf{H}_T = \mathbf{I}$ , the identity matrix, while the interference from noise after beamforming,  $E[|\mathbf{B}^t \mathbf{n}_T|^2]$ , needs to be minimized. Since  $E[|\mathbf{B}^t \mathbf{n}_T|^2] = E[\mathbf{n}_T^t \mathbf{B} \mathbf{B}^t \mathbf{n}_T] = \text{Tr}(\mathbf{B}^t \Sigma_n \mathbf{B})$ , the problem of MVDR beamforming can be

summarized as

$$\begin{aligned} & \underset{\mathbf{B}}{\text{minimize}} && \text{Tr}(\mathbf{B}^t \boldsymbol{\Sigma}_n \mathbf{B}) \\ & \text{subject to} && \mathbf{B}^t \mathbf{H} = \mathbf{I}, \end{aligned} \quad (5.18)$$

which gives  $\mathbf{B}_{opt} = \boldsymbol{\Sigma}_n^{-1} \mathbf{H}_T (\mathbf{H}_T^t \boldsymbol{\Sigma}_n^{-1} \mathbf{H}_T)^{-1}$  (see Appendix D, Section D.2).

The solution of (5.18) is recognized as the *Frost* beamformer [81]. It is the same as the Capon beamformer when the impulse responses from received elements are known. In our analysis, known impulse responses were required to model the ideal observer when the signals are known statistically. In much literature, the MV beamformer is implemented from Capon beamforming without knowledge of the impulse responses [70–73]. For the Capon beamformer, the RF data is modeled at an instant of time  $t$ ,

$$\mathbf{x}(t) = \begin{bmatrix} x_0(t) \\ x_1(t) \\ \vdots \\ x_{N-1}(t) \end{bmatrix}, \quad (5.19)$$

where  $x_i(t)$  is the RF signal at element  $i$  of the transducer. The beamformer output  $y(t)$  and its energy is given by

$$\begin{aligned} g(t) &= \mathbf{w}(t)^t \mathbf{x}(t) \quad \text{and} \\ P(t) &= E[|g(t)|^2] = \mathbf{w}(t)^t \mathbf{R}_{xx}(t) \mathbf{w}(t), \end{aligned} \quad (5.20)$$

where  $\mathbf{w}(t) = [w_0(t), w_1(t), \dots, w_{N-1}(t)]^t$  and  $w_i(t)$  is the aperture weight of element  $i$ , and  $\mathbf{R}_{xx}(t) = E[\mathbf{x}(t)\mathbf{x}(t)^t]$  is the spatial covariance matrix of RF data. The beamforming problem is formulated as

$$\begin{aligned} & \underset{\mathbf{w}}{\text{minimize}} && \mathbf{w}(t)^t \mathbf{R}_{xx}(t) \mathbf{w}(t) \\ & \text{subject to} && \mathbf{w}(t)^t \mathbf{a} = 1, \end{aligned} \quad (5.21)$$

where  $\mathbf{a}$  is a steering vector. For ultrasound beamforming,  $\mathbf{a}$  is usually a vector of ones, equivalent to focusing beam energy only at a steering angle of  $0^\circ$ . The optimal  $\mathbf{w}(t)$  for (5.21) is given by [71]

$$\mathbf{w}_{opt}(t) = \frac{\mathbf{R}_{xx}^{-1}(t) \mathbf{a}}{\mathbf{a}^t \mathbf{R}_{xx}^{-1}(t) \mathbf{a}}. \quad (5.22)$$

The solution in (5.22) is sometimes called *adaptive* beamforming because the calculation

of  $\mathbf{w}(t)$  is adapted to the incoming RF data  $\mathbf{x}$ .

To see the similarity between  $\mathbf{B}_{MV}$  and  $\mathbf{w}_{opt}$ , we first re-write  $\mathbf{B}_{MV}$  as

$$\mathbf{B}_{MV} = \Sigma_n^{-1} \mathbf{H}_T (\mathbf{H}_T^t \Sigma_n^{-1} \mathbf{H}_T)^{-1} = \Sigma_{T,i}^{-1} \mathbf{H}_T (\mathbf{H}_T^t \Sigma_{T,i}^{-1} \mathbf{H}_T)^{-1}, \quad (5.23)$$

for  $i = 0$  or  $1$  (see Appendix D, Section D.3). Thus,  $\mathbf{B}_{MV}$  can also be calculated from RF data underlying either hypothesis  $H_i$ . Another concern is whether  $\mathbf{w}_{opt}$  includes an inverse operator like  $\mathbf{B}_{MV}$  does, even though it was derived without knowing the impulse responses of transducer elements. The question can be answered intuitively as follows: Assuming that  $\mathbf{w}_{opt}$  in (5.22) works perfectly, the impulse response of the system after beamforming will be one at  $0^\circ$  and zero elsewhere, which forms a direct delta function for the pulse-echo impulse response. Because the input object is modeled as a set of independent scatterers and scanned by the ideal system, the output RF data is not blurred and the spatial covariance matrix of  $\mathbf{w}(t)^t \mathbf{x}(t)$  is diagonal. Since  $\mathbf{R}_{xx}(t)$  is a covariance matrix of correlated data,  $\mathbf{w}(t)^t$  must include an inverse operator to de-correlate the data.

Although both (5.18) and (5.21) are set to the same solution, their implementations may provide different answers. In (5.18), the covariance matrix is known from the signal modeling. A low-rank approximation may be required to handle the poor condition of matrix  $\mathbf{H}_T^t \mathbf{H}_T$ . In (5.21), the covariance matrix is estimated from output data, using the *sample matrix inversion* (SMI) method. The convergence of the SMI method, and the distributions of the largest eigenvalues in SMI as well, are very open problems and beyond the scope of this research [82, 83].

### 5.3.2 Wiener filtered beamformer

The second beamformer  $\mathbf{B}_{WF}^t = (\sigma_{obj}^2 \mathbf{H}_T^t \mathbf{H}_T + \sigma_n^2 \mathbf{I})^{-1} \mathbf{H}_T^t$  has the form of a Wiener filter. However, it differs from the Wiener filter derived in our initial study [26], in which  $(\sigma_{obj}^2 \mathbf{H}_T^t \mathbf{H}_T + \sigma_n^2 \mathbf{I})^{-1}$  and  $\mathbf{H}_T^t$  are swapped. This difference reflects a strategy of the ideal observer in beamforming. The observer first compresses RF data before processing it to arrive at a test statistic needed to make the decision.

The WF beamformer can be derived in the MMSE approach [68]. We also consider the WF beamformer as a solution of a general problem of Tikhonov regularization, given by [84]

$$\underset{\mathbf{f}}{\text{minimize}} \|\mathbf{g}_T - \mathbf{H}_T \mathbf{f}\|_2^2 + \gamma \|\mathbf{f}\|_2^2, \quad (5.24)$$

where  $\gamma$  is a regularized parameter ( $\gamma > 0$ ). Tikhonov regularization gives a solution of

$$\hat{\mathbf{f}}_{opt} = (\mathbf{H}_T^t \mathbf{H}_T + \frac{\gamma}{\sigma_{obj}^2} \mathbf{I})^{-1} \mathbf{H}_T^t \mathbf{g}_T, \quad (5.25)$$

provided  $\mathbf{f}$  is the scattering object from a low-contrast lesion, or  $\Sigma_f \simeq \sigma_{obj}^2 \mathbf{I}$ .

Without the regularization term, the solution of (5.25) becomes  $\hat{\mathbf{f}}_{opt} = \hat{\mathbf{f}}_{MV} = \mathbf{B}_{MV}^t \mathbf{g}_T$ . Because  $\mathbf{B}_{MV}^t \mathbf{H}_T = \mathbf{I}$ , the reconstruction error is given by

$$|\hat{\mathbf{f}}_{MV} - \mathbf{f}|_2 = |\mathbf{B}_{MV}^t \mathbf{H}_T \mathbf{f} - \mathbf{f} + \mathbf{B}_{MV}^t \mathbf{n}|_2 = |\mathbf{B}_{MV}^t \mathbf{n}|_2, \quad (5.26)$$

which can be quite high, particularly if  $\mathbf{H}_T$  is poorly conditioned. Thus, the regularization term helps avoid the ill-conditioned  $\mathbf{H}_T$ . The optimal regularized parameter  $\gamma$ , however, is usually unknown and in practical problems often determined by an *ad hoc* method.

By using the ideal observer analysis, we find the optimal regularized parameter  $\gamma = \sigma_n^2$ , or the solution of the regularization problem becomes the WF beamforming operator. In Appendix D, Section D.1, it is also shown that the WF beamformer is tolerant toward the ill-conditioning of  $\mathbf{H}_T$ , while the MV beamformer is reduced to the pseudoinverse  $\mathbf{H}_T^+$ . The outperformance of the WF beamformer in comparison to the MV can be observed through first-order approximations of (5.12) and (5.14). The approximation of (5.14) is much better if the eigenvalues of  $\mathbf{K}_n^{-1}$  are large, where  $\mathbf{K}_n \triangleq \sigma_{obj}^2 \mathbf{H}_T^t \Sigma_n^{-1} \mathbf{H}_T$ . A large  $\mathbf{K}_n^{-1}$  is equivalent to the poor condition of  $\mathbf{H}_T$  or low eSNR. These findings are in agreement with those from other studies [80], but we found them from an analytical framework developed on the basis of the ideal observer. Performance of those beamformers is demonstrated through numerical results in the next section.

## 5.4 Simulation

### 5.4.1 Implementation using Field II program

The 2-D pulse-echo impulse response for each transducer element is generated by using the Field II program [43,44], modeling after the SONOLINE Antares system (Siemens Medical Solutions, Mountain View, CA) with transducer VF10-5. The transducer array has 192 total elements separated by a 0.02 mm element kerf. By setting a 40 mm transmit/receive focal length and  $f/2$  in plane, the active aperture  $\sim 20$  mm, equivalent to 96 elements. The element impulse responses and that of the corresponding DS beamformer are generated

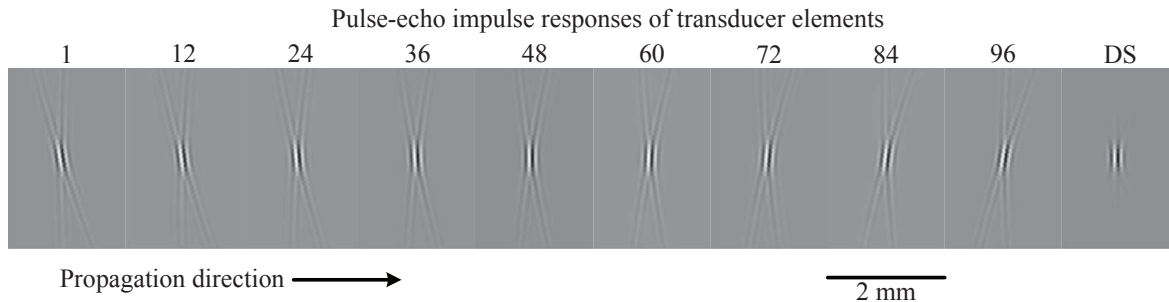


Figure 5.2: Pulse-echo impulse responses in 2-D of transducer elements. The last image (DS) is for the delay-and-sum beamformer.

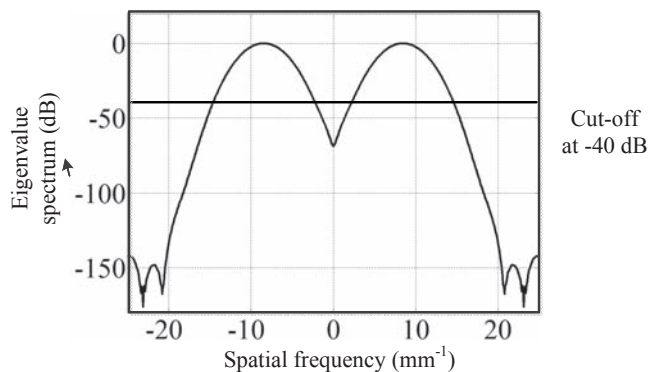


Figure 5.3: The normalized eigenvalue spectrum of  $\mathbf{H}_T^t \mathbf{H}_T$  with cut-off at  $-40$  dB to implement the MV beamformer [32].

and illustrated in Figure 5.2

Based on the pulse-echo impulse response from element  $j$ , we construct multiplication matrix  $\mathbf{H}_j$  and form system matrix  $\mathbf{H}_T$  for pre-beamformed RF data. Since  $\mathbf{H}_T$  is very large, a circulant assumption was made for each  $\mathbf{H}_j$ , providing advantages in computation [26]. The MV beamformer involves the ill-conditioned matrix product  $(\mathbf{H}_T^t \mathbf{H}_T)^{-1}$ , which requires a low-rank approximation. Figure 5.3 shows the normalized eigenvalue spectrum of  $\mathbf{H}_T^t \mathbf{H}_T$ . By cutting off frequency contributions less than  $-40$  dB, the percentage of total power contained in the discarded eigenvalues is less than 0.03%. The MV is implemented as the pseudoinverse of  $\mathbf{H}_T$  [68].

Figure. 5.4 shows an example of B-mode images for Task 4 with the spiculated “malignant” lesion on the top in all cases. Four beamformers are used to generate four pairs of images, including DS, MF, MV, and WF. Visually, the MF beamformer has the largest speckles. Both WF and MV beamformers reduce speckle sizes and make lesion boundaries become clearer. Comparing WF and MV beamformed B-mode images, the WF appears

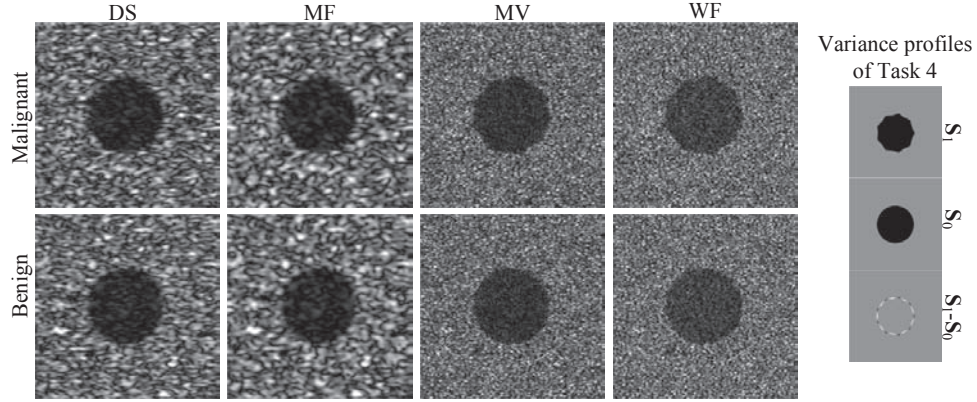


Figure 5.4: Examples of B-mode images for Task 4, implemented with four beamformers, including DS, MF, MV, and WF.

to have a better spatial resolution but lower contrast resolution.

#### 5.4.2 Results

The image quality of the envelope images is first evaluated through two basic metrics of contrast and spatial resolution. The images of a benign lesion in Figure. 5.4 are selected to evaluate the contrast resolution through beamforming techniques. The contrast resolution between a cyst and the background can be measured as [85]

$$C = \frac{S_{out} - S_{in}}{\sqrt{S_{out}^2 + S_{in}^2}}, \quad (5.27)$$

where  $S_{in}$  is the mean signal measured inside the cyst and  $S_{out}$  is the average signal measured from the same size region outside the cyst. By setting the contrast of the cyst equal to 5% the background at the benign variance profile for generating the benign B-mode, the contrast resolutions on envelope images for four beamformers are as follows:  $C_{DS} = 0.6486$ ,  $C_{WF} = 0.6552$ ,  $C_{MV} = 0.6140$ , and  $C_{WF} = 0.4035$ , corresponding to DS, MF, MV, and WF beamformers. Thus MV and WF beamformers reduce the contrast resolution, especially for the WF.

The spatial resolution on B-mode images is limited by the size of the acoustic speckles. The smaller size speckle provide for better spatial resolution. Therefore, the size of the speckle spots can be used to evaluate the spatial resolution. Speckle size is measured through the normalized autocovariance function (ACVF) of the B-mode image of fully developed speckles [21]. An example of a B-mode image with its normalized autocovari-

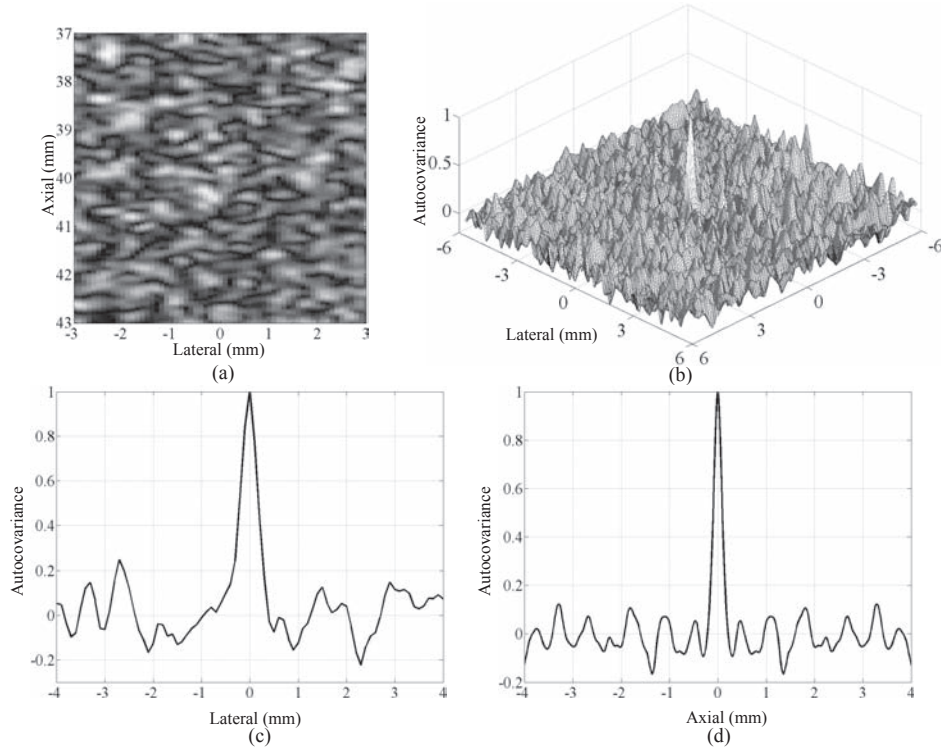


Figure 5.5: (a) An example of fully developed speckles. (b) Normalized autocovariance function used to calculate the speckle size. (c) Lateral cut through 0. (d) Axial cut through 0.

ance function, including one pulse on a noisy background, is shown in Figures 5.5 (a,b). The size of the speckle is measured at full width at half maximum ( $-6$  dB) of the pulse in both axial and lateral directions (Figures 5.5(c,d)) .

The ACVF's of DS, MF, MV, and WF are plotted in axial and lateral directions as in Figure. 5.6. The size of the speckle spots on DS B-mode images is about 0.158 mm in the axial and 0.454 mm in the lateral cuts. The MF beamformer broadens the speckle size in the axial (0.219 mm) and the lateral (0.473 mm) directions. The MV and WF both make the speckle area smaller, but between them the WF is a little better. The speckle size in the MV B-mode is 0.098 mm in the axial and 0.178 mm in the lateral axes, while in the WF B-mode, the sizes are 0.087 mm and 0.104 mm, respectively.

Beamformer performance is quantified using observer efficiency that characterizes the loss of task information through demodulation. The ideal observer is combined with the SW observer for B-mode images in (4.6) to calculate the efficiencies of transferring diagnostic information from RF data to B-mode for each beamformer. The efficiencies of the four beamformers applied to five lesion features are plotted in Figure 5.7. The efficiency of MF is always the lowest. The WF and MV make substantial improvements

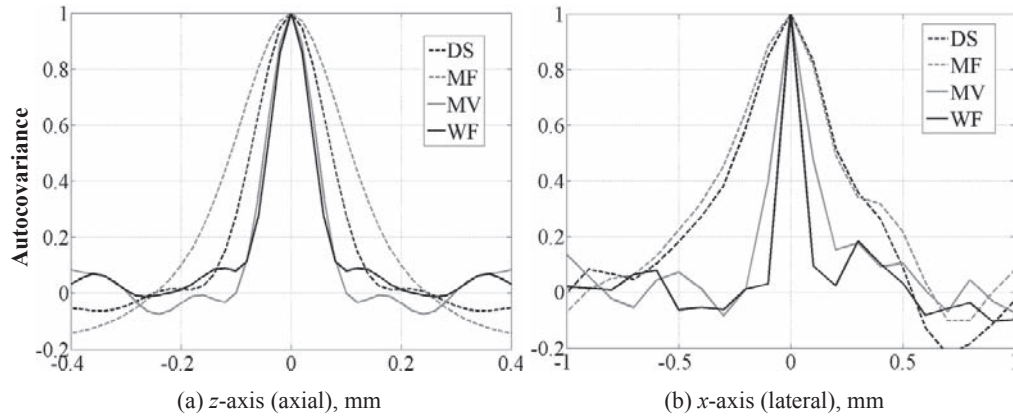


Figure 5.6: Autocovariance function of speckle images through DS, MF, MV, and WF beamformers, showing (a) axial cut through  $x = 0$  and (b) lateral cut through  $z = 0$ .

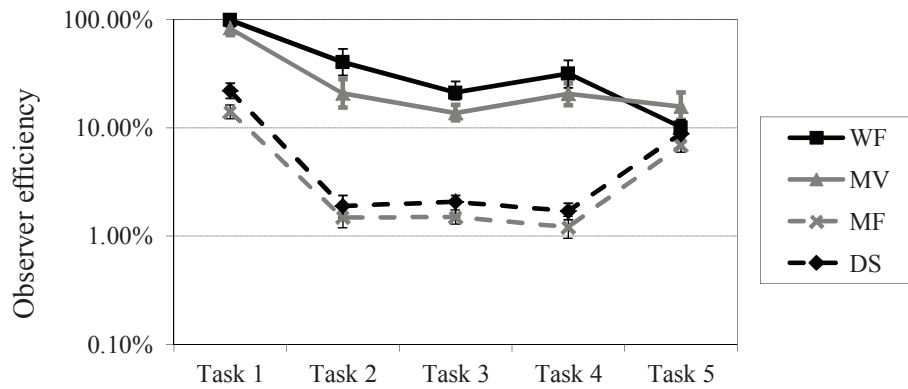


Figure 5.7: Observer efficiencies on B-mode images with different beamformers. An efficiency of 1 indicates that all task information is passed from RF echo signals into B-mode images. Error bars indicate one standard error.

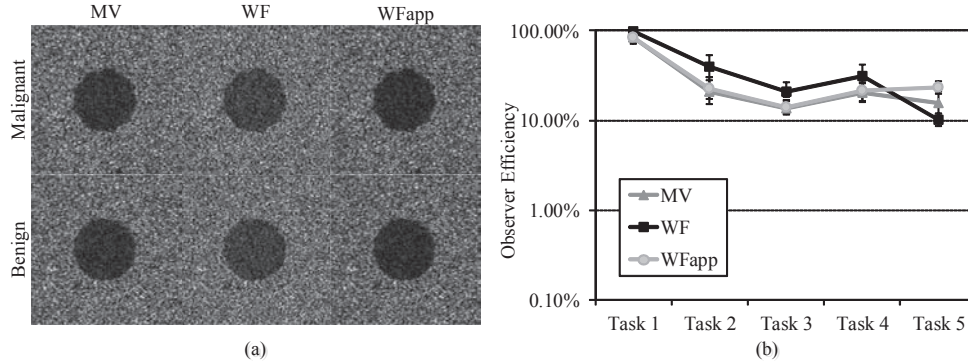


Figure 5.8: The envelope images of the MV and WF, and the WFapp B-mode implemented from the same RF data (a), along with the efficiency of the SW observer on those beamformers (b).

for the first four tasks, but in Task 5 (anechoic/hypoechoic), the efficiency of WF is reduced to approximately that of the DS (10.08% vs 8.85%). In Task 5, efficiency for MV is larger (15.71%).

To analyze the performance of the MV beamformer relative to the WF beamformer in Task 5, we notice that the low-rank approximation used to implement the MV has changed the system model. Therefore, we implement the WF beamformer with the same low-rank approximation for comparison between the WF and MV beamformers and refer to it as WFapp. The images of WFapp B-mode and its observer efficiency are plotted in Figures 5.8 (a,b) to compare with the other two beamformers. In Figure 5.8(a) the B-mode image from the WFapp appears to have the spatial resolution on par with the MV and somewhat improved contrast resolution. On the efficiency chart in Figure 5.8(b), the improvement of WFapp in comparison with the MV is very small in the first four tasks (less than 2%) but is significant for Task 5 (7.45%). In comparison with the WF beamformer computed at full rank, WFapp has lower efficiency in the first four tasks, but higher efficiency in Task 5 (23.16% vs 10.08%).

## 5.5 Discussion

In acoustic beamforming as applied to the formation of medical B-mode images, two irreversible processes reduce task information. The first occurs at the acquisition stage, where signals from all transducer elements are combined into a single A-scan line. The second occurs in demodulation at the display stage, where the phase component of RF data is discarded as required to interface with the human eye-brain system. Any information

loss involving these two processes cannot be recovered at the final envelope images.

By using the ideal observer analysis, we found that ideal performance is still reached through matched filtering. Thus, the MF beamformer preserves task information transferred from multiple received channels to the beamformed RF echo signals. In ultrasonic systems, however, beamformed RF signals are not the final images accessible by human observers. More information would be lost if demodulation is applied to the MF beamformed RF data [31]. The MF beamformer should be followed by de-blurred operators, which occur with MV and WF beamformers, to help preserve task information.

We found by applying ideal observer analysis that the minimum variance (MV) and Wiener filter (WF) beamformers each approximate to the ideal strategy. The difference between WF and MV beamformers is the additional term  $\sigma_n^2 \mathbf{I}$  in the inverse operator, in which  $\sigma_n^2 \mathbf{I}$  arose from a more accurate first-order approximation to the covariance matrix inverse. The better first-order approximation of the WF beamformer improves the SW observer performance. Therefore, WF should outperform MV in all five tasks. The improvement is significant when  $(\sigma_{\text{obj}}^2 \mathbf{H}_T^t \mathbf{H}_T / \sigma_n^2)^{-1}$  has large eigenvalues (low eSNR or poor conditioned  $\mathbf{H}_T$ ). Implementation of the MV, however, requires a low-rank approximation that changes the system model. The noise filtering advantages of rank reduction are well matched to the spatial-frequency requirements of Task 5, improving the MV beamformer performance.

# CHAPTER 6

## MEASUREMENTS OF THE SPATIOTEMPORAL PULSE-ECHO IMPULSE RESPONSE

### 6.1 Introduction

In the ideal observer analysis, the system matrix  $\mathbf{H}$  (or  $\mathbf{H}_T$  for pre-beamformed signals) plays a central role in modeling, developing beamforming algorithms, and post-processing filters suggested by the ideal strategy. Therefore, it is very important to have an accurate  $\mathbf{H}$ , which is most reliably obtained from experimental data. As described in Chapter 2, Section 2.3,  $\mathbf{H}$  is constructed from the pulse-echo spatiotemporal impulse response or point-spread-function (PSF) of the system, which can vary in space and time. An accurate measurement of the PSF is difficult to obtain. The PSF is also difficult to model accurately from some software programs [43, 44] because even small, unknown perturbations in the linear array transducer geometry can make significant changes in measured pulse-echo field patterns compared with modeled patterns, especially in the near-field.

A simple measurement is accomplished in the scan plane from local autocovariance estimates applied to fully developed image speckle [19] (see Figure 5.5). Coherent summation of reflected pressure waves measured at the transducer surface from randomly distributed scattering media results in B-mode speckles whose dimensions indicate in-plane spatial resolution, but only under the limiting conditions where maximum coherence is achieved (focal zone). It is well known that speckle correlation lengths for off-focus field locations and conditions that distort pulse phases, e.g., aberration media, underestimate the spatial extent of the impulse response and provide no direct phase information.

Better PSF estimates for 1-D arrays are obtained from RF signals of a line-scatterer reflection, provided the scattering material does not acoustically resonate near the carrier frequency. Beam profile phantoms with line scatterers are commercially available, e.g., ATS #539 (ATS Industries, Bridgeport CT). The echo pattern appears as a point response

---

Portions of this chapter are reprinted, with permission, from N.Q. Nguyen, C.K. Abbey, R.D. Yapp, and M.F. Insana, "Tomographic reconstruction of the pulse-echo spatiotemporal impulse response" in *Proceedings of Society of Photo-Optical Instrumentation Engineers (SPIE)*, vol. 7629, pp. 76290F.1-11, © 2010 The international society for optics and photonics.

in the scan plane, but is actually a LSF, which is the PSF integrated over the elevational dimension of the transducer aperture. Depending on the elevational beamwidth, the LSF may or may not be a good approximation of the PSF.

In this chapter, we propose two methods to measure the PSF that both follow the linear pulse-echo model describing RF data developed by Zemp et al. [41]. In the first method, the PSF is measured by scanning a single scatterer that approximates a Dirac delta function applied to the system input. In the second method, the function is reconstructed by processing echoes obtained from a line scatterer rotated in a plane normal to the beam axis. Applying a linear pulse-echo model of echo formation, LSF echoes are shown to yield projections of the sound beam that may be reconstructed to estimate the PSF. Projections are linear transformations of the PSF along lines in space. Reconstruction from projections is an inverse problem that can be solved through application of *singular value decomposition* (SVD) [8]. Our approach has similarities to standard filtered backprojection used in photon transmission or emission tomography [86], but a major geometric difference is that the detector does not rotate with the projection source. Pulse-echo projections from 1-D arrays contain a large null space that limits reconstruction accuracy. Some methods have been proposed for improving the reconstructed results. Mathematically, we show that the null space can be filled by using the 2-D transducer array or moving the transducer in the elevation direction. Without a 2-D array, however, this method is not feasible experimentally due to the time consuming aspects of data acquisition and the errors that are added during the long acquisition process. Therefore, the algebraic reconstruction technique (ART) has been applied. It was demonstrated in X-ray computed tomography that ART has improvements over the filtered backprojection method for situations of incomplete data or limited angle projections [87].

## 6.2 Scattering spheres

In this method, we use a gelatin gel volume into which 0.04 mm diameter glass spheres are randomly suspended. The density of the glass is 2.38 g/cc and the speed of sound in glass is 5570 m/s. The density and sound speed of the gelatin is 1.06 g/cc and 1500 m/s. With a pulse center frequency of 10 MHz, the sphere diameter is less than one third of the wavelength and thus the high-scattering point targets are reasonable approximations to delta functions. Figure 6.1(a) shows the experimental setup for the measurement. The sampling frequency of the SONOLINE Antares system is 40 MHz, which is equivalent to a resolution of 0.0193 mm in the axial direction. Therefore, an automation controller

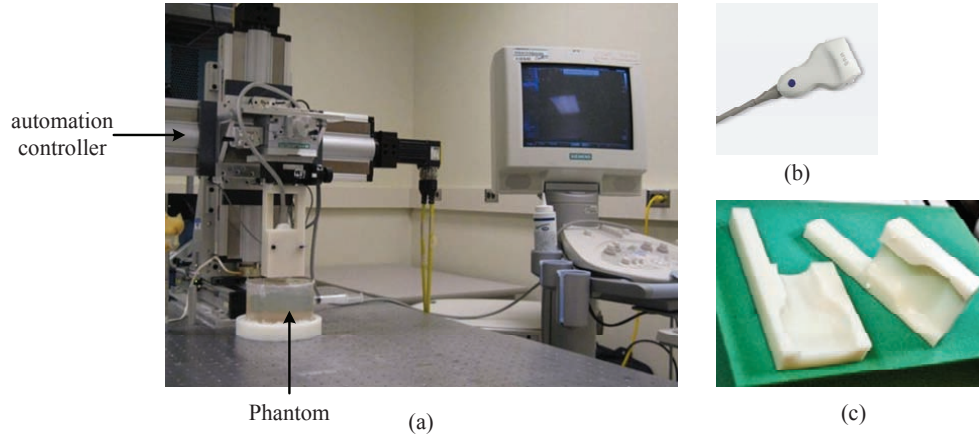


Figure 6.1: (a) Experimental setup including a motion controller and a phantom, (b) transducer VF 10-5, and (c) a holder that attaches the transducer to the motion controller.

(Parker Daedal), with a micrometer graduation of  $10^{-4}$  mm in all three dimensions, is used to adjust the position of the transducer. To guarantee the transducer is perpendicular to the surface of the phantom, a transducer holder (Figure 6.1(c)) is designed for mounting the transducer (Figure 6.1(b)) to the controller.

Figure 6.2(a) shows a B-mode image through a cross section of the gel in the axial-lateral plane. Notice how the impulse response varies with distance. Because the spheres are so small, the image shows the envelope of weak and noisy impulse responses at different spatial locations. For zero-mean additive noise, eSNR is increased by a factor of 1000 by averaging 1000 RF echo signals without moving the transducer. Recall that the transducer VF 10-5 being used is a linear array. A fixed focus of 40 mm was set on both transmit and receive. The lateral array pitch is 0.2 mm. The PSF are most compact near the focal length but broaden in both near-field and far-field regions. Moving the transducer in elevation at 0.5 mm increments, we acquired many planes to synthesize the 3-D PSF for the system. Figure (6.2)(b) shows an axial cut of this function at a distance of 52 mm (far-field) with the phase varied over the elevation-lateral plane.

Figure 6.3 shows axial cuts of RF echo signals through the lateral-elevational plane recorded at three distances: near-field, focal, and far-field. The sections are through planes of generally curved functions (with respect to constant phase fronts) that have not been demodulated. The elevation cuts of the corresponding PSFs through the axis origin are presented in Figure 6.4. The dark line on each image indicates the position of the cross section shown in Figure 6.3.

This method is fast and convenient; however, it has two disadvantages. First, the scattering signals from tiny glass spheres are weak, so measurements may be affected by

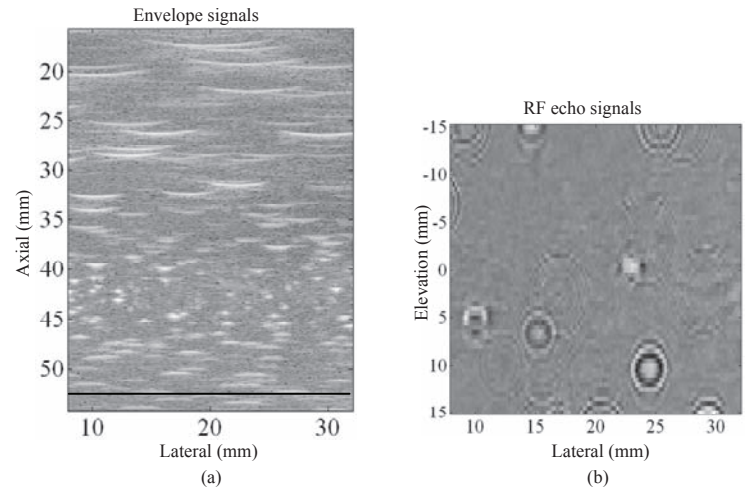


Figure 6.2: (a) A log-compressed B-mode image of a cross section of a gelatin block with a random distribution of 0.04 mm diameter spheres. eSNR is improved by averaging 1000 RF data frames. (b) A cut in the lateral-elevation plane at a distance of 52 mm (far-field), formed by moving the transducer in elevation at 0.5 mm increments.

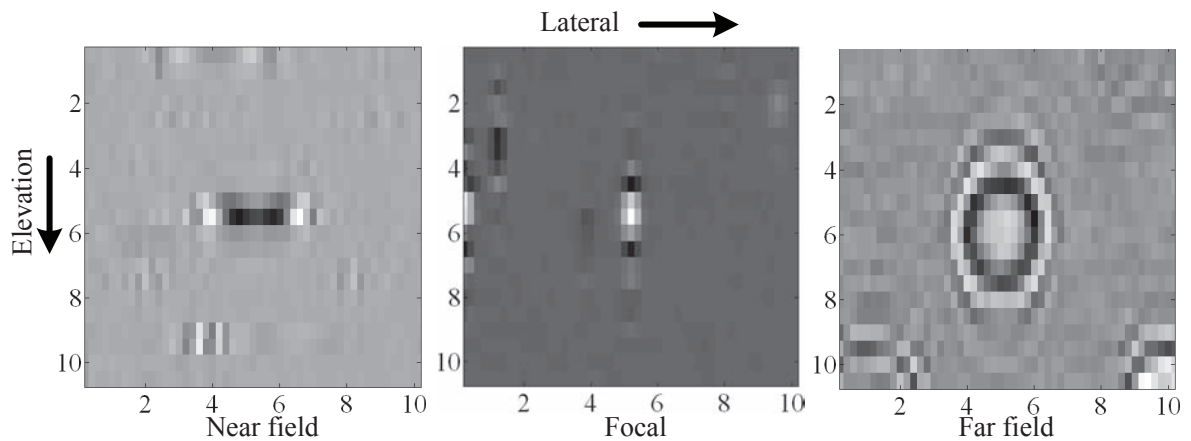


Figure 6.3: The axial cut of 3-D pulse-echo spatiotemporal impulse response in the near-field, focal-length, and far-field distances. Distances are in mm. When more than one sphere is in the field, there are multiple copies of PSFs.

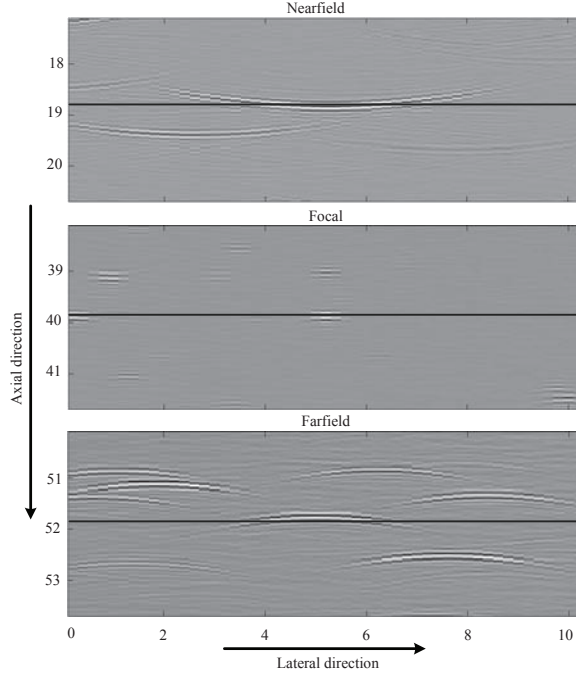


Figure 6.4: The elevation cuts through 0 of 3-D pulse-echo spatiotemporal impulse responses at near-field, focal-length, and far-field distances. Distances are in mm.

scattering from gel impurities and surface reflections. These are apparent in Figures 6.3 and 6.4. Second, the shift-varying impulse response requires scatterers to be placed far enough apart to not interfere and yet dense enough to capture the spatial variations in the impulse response. These problems can be avoided by reconstructing impulse responses from line scatterers as described in the next section.

## 6.3 Reconstruction from projections of rotating line

### 6.3.1 Background

The scan of a line rotated in a plane normal to the beam axis is illustrated in Figure 6.5. Zemp et al. [41] modeled the formation of RF echo signals  $g$  as a linear system given by

$$g(\mathbf{t}) = \int d\mathbf{x} h(\mathbf{x}, \mathbf{t})f(\mathbf{x}) + n(\mathbf{t}) . \quad (6.1)$$

Scattering function  $f$  is represented in object space at vector position  $\mathbf{x} = (x, y, z)$ . Object functions are linearly mapped into data  $g$  recorded at acquisition-time-dependent vector

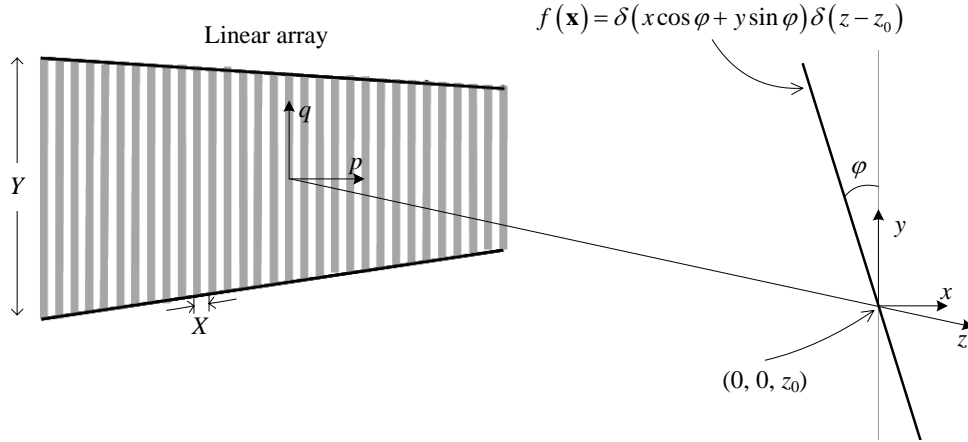


Figure 6.5: Geometry of the linear array and line scatterer (represented as Dirac deltas) are illustrated. The array coordinates  $p, q$  are sampled on the spatial intervals  $X, Y$ , respectively. The line scatterer, with coordinates  $x, y, z$ , is rotated in the  $xy$  plane about the  $z$  axis with angle  $\varphi$  [33].

$\mathbf{t} = (t_1, t_2, t_3)$  through the pulse-echo spatiotemporal impulse response  $h$ . Function  $n$  is signal-independent, white Gaussian noise originating from the measurement process. Echo acquisition is a mapping of spatial objects into temporal data, while B-mode image formation restores the spatial context for human interpretation. To reconstruct  $h$  from  $g$  projections, we must first describe essential space-time relationships among objects, RF data, and images.

Echo data are acquired as a sequential linear array, first along range time  $t_1$  to yield an A-line, then along cross-range time  $t_2$  to yield a frame, but the acquisition may be extended to “elevational time”  $t_3$  for dynamic imaging or volumetric acquisitions. The total acquisition time is  $t = t_1 + t_2 + t_3$ . Echoes are sampled in range at time  $t_1 = \ell T$ , for integer  $1 \leq \ell \leq L$  and at constant interval  $T$ . The  $t_1$  axis is approximately proportional to the image depth axis  $z$  via  $t_1 = 2z/c$  for sound speed  $c$ . Cross-range echo sampling corresponds to the lateral  $p$  axis of the array in Figure 6.5. We have  $t_2 = mLT$  for  $M$  lines per frame and  $-M/2 \leq m \leq M/2$ . The  $t_2$  axis is proportional to the lateral image axis  $p$  via  $t_2 = pLT/X$ ,  $p = mX$ , and array pitch  $X$ . For the 1-D arrays in Figure 6.5, the elevational axis is a point at  $q = 0$ , and so we set  $t_3 = rMLT$  for  $1 \leq r \leq R$  to track the time between frames,  $MLT$ , for a total acquisition time  $t = RMLT$ . However, for echo-volume acquisitions using a 2-D linear array,  $t_3 = rMLT/Y$  records acquisitions along the  $q$  axis of the 2-D array, and the volumetric frame rate is  $1/RMLT$ . Conversion from temporal to spatial coordinates using a 1-D array is summarized by the scan-conversion

imaging equation,

$$\mathbf{t} = \mathbf{P}\mathbf{x}, \quad \text{or} \quad \begin{pmatrix} t_1 \\ t_2 \end{pmatrix} = \begin{pmatrix} 2/c & 0 \\ 0 & LT/X \end{pmatrix} \begin{pmatrix} z \\ p \end{pmatrix}. \quad (6.2)$$

Zemp et al. [41] showed that the pulse-echo spatiotemporal impulse response  $h(\mathbf{x}, \mathbf{t})$  reduces to the PSF when the field position of a point scatterer is fixed and a frame is acquired, i.e.,  $\text{PSF}(\mathbf{t}) = h(\mathbf{t}|\mathbf{x})$ . Analogously, the *spatial sensitivity function* (SSF) is obtained when acquisition time is fixed and a point reflector is scanned in space,  $\text{ssf}(\mathbf{x}) = h(\mathbf{x}|\mathbf{t})$ . Also, for *isoplanatic* regions of the beam, the impulse response is shift invariant and, consequently, a function of a single variable,  $h(\mathbf{t} - \mathbf{P}\mathbf{x})$ . In isoplanatic regions, (6.1) becomes a convolution in the spatial domain,  $g(\mathbf{t}) = [h *_{\mathbf{x}} f](\mathbf{t}) + n(\mathbf{t})$ .

### 6.3.2 Problem formulation

Projections in pulse-echo ultrasound are echo signals reflected from a line scatterer represented by a product of Dirac deltas

$$f(\mathbf{x}) = \delta(x \cos \varphi + y \sin \varphi) \delta(z - z_0). \quad (6.3)$$

This object function is a line in the  $xy$  plane at distance  $z_0$  that is scanned by an array along the  $p$  axis. The line is then rotated about the  $z$  axis to angle  $\varphi$ . Consequently,  $(x, y, z)$  are object coordinates,  $(p, \varphi, t_1)$  are echo-data coordinates, and there is a mapping among them.

Applying (6.3) to (6.1), and ignoring the noise term, we express the echo signal as a function of  $\varphi$ ,

$$g(\mathbf{t}, \varphi) = \int dy \int dx h(x, y, z_0, \mathbf{t}) \delta(x \cos \varphi + y \sin \varphi), \quad (6.4)$$

where integration is over the entire  $xy$  plane and the results hold only at  $z = z_0$ . Since shift invariance can be assumed at a fixed distance,  $h(\mathbf{x}, \mathbf{t}) = h(\mathbf{t} - \mathbf{P}\mathbf{x})$ . Combining (6.2)

and (6.4) gives (see Figure 6.6),

$$\begin{aligned}
g(t_1, t_2, \varphi) &= \int dy \int dx h\left(\frac{Xt_2}{LT} - x, 0 - y, \frac{ct_1}{2} - z_0\right) \delta(x \cos \varphi + y \sin \varphi) \\
g(p, \varphi, t_1) &= \int dy \int dx h(x, y, \frac{ct_1}{2} - z_0) \delta[(p - x) \cos \varphi - y \sin \varphi] \\
g(\mathbf{s}) \triangleq g(p, \varphi) &= \int d\mathbf{r} h(\mathbf{r}) \delta(p \cos \varphi - \mathbf{r} \cdot \mathbf{n}(\varphi)).
\end{aligned} \tag{6.5}$$

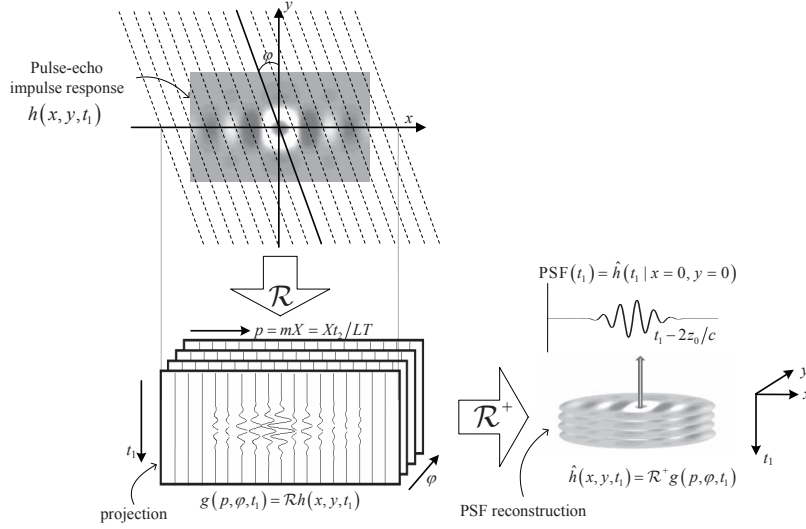


Figure 6.6: Geometry used to acquire echo projections and reconstruct the impulse response. Positioning a line scatterer in the  $xy$  plane at distance  $z = z_0$ , we explore  $h(x, y, t_1 | z_0, t_2, t_3)$  abbreviated as  $h(x, y, t_1)$ . Rotating the line scatterer about the  $z$  axis, we record projections  $g(p, \varphi, t_1)$  that are modeled by transformation  $\mathcal{R}h(x, y, t_1)$ . Reconstruction is implemented by the pseudoinverse,  $\hat{h}(x, y, t_1) = \mathcal{R}^+ g(p, \varphi, t_1)$ , which when computed for all  $t_1$  gives  $\hat{h}(x, y, t_1)$ . The PSF at location  $x, y, z_0$  is  $\text{PSF}(t_1) = \hat{h}(t_1 | x, y)$ . The operator  $\mathcal{R}$  maps information in object coordinates  $x, y, z_0$  into data coordinates  $p, \varphi, t_1$ , while the inverse operator  $\mathcal{R}^+$  maps them back [33].

The first form of (6.5) explicitly recognizes that we acquire data in range, cross-range, and at different projection angles. The second form performs the convolutional shifts on the delta function instead of  $h$  and substitutes  $p$  for  $t_2$ . The last form of (6.5) expresses the echo data as a *modified sinogram* for each range time  $t_1$ ; henceforth the  $t_1$  and  $z$  axes are implied. The modification from the traditional CT projections is that the detector does not rotate with the line scatterer, and therefore the delta function depends on  $p \cos \varphi$  instead of  $p$  as in computerized tomography. We have used  $\mathbf{s} = (p, \varphi)$  as a position vector in data space. Note that while  $\varphi$  ranges from 0 to  $\pi$ ,  $p$  is limited by the field of view  $[-a, a]$  of the system, where  $2a$  is the width of the transducer or the field of view. In

object space, we indicate field points using position vector  $\mathbf{r} = (x, y)$  and line-scatterer orientation using the unit direction vector  $\mathbf{n}(\varphi) = (\cos \varphi, \sin \varphi)$ . Now interpretation of the expression in terms of projection geometry becomes clear: each echo signal is made up of impulse response contributions that lie along a line connecting the center of the active array aperture to all points on the line scatterer, viz.,  $p \cos \varphi = \mathbf{r} \cdot \mathbf{n}(\varphi)$  (see Figure 6.5). Finally, sinogram generation is written compactly using operator  $\mathcal{R}$  via

$$g(\mathbf{s}) = [\mathcal{R} h](\mathbf{s}) \triangleq \int d\mathbf{r} h(\mathbf{r}) \delta(p \cos \varphi - \mathbf{r} \cdot \mathbf{n}(\varphi)) , \quad (6.6)$$

where  $\mathcal{R} : \mathcal{L}_2(\mathbb{R}^2) \rightarrow \mathcal{L}_2([0, \pi] \times [-a, a])$ .

Thus,  $h(\mathbf{s})$  can be reconstructed through the inverse operator  $\mathcal{R}^+$ . The diagram for the whole reconstruction of 3-D pulse-echo spatiotemporal impulse response is illustrated in Figure 6.6.

### 6.3.3 Filtered backprojection

By using the SVD method, the reconstruction  $\hat{h}(\mathbf{r})$  is given by

$$\begin{aligned} \hat{h}(\mathbf{r}) &= [\mathcal{R}^+ g](\mathbf{r}) \\ &= \int_0^\pi d\varphi \int_{-a}^a dp \int d\boldsymbol{\rho} |\cos \xi| e^{j2\pi \boldsymbol{\rho} \cdot \mathbf{r}} e^{-j2\pi \rho p \cos \theta} \delta(\xi - \varphi) g(p, \varphi) \\ &= \int_0^\pi d\varphi \int d\rho |\rho| e^{j2\pi \rho \mathbf{r} \cdot \mathbf{n}(\varphi)} |\cos \varphi| \int_{-a}^a dp e^{-j2\pi \rho p \cos \varphi} g(p, \varphi) , \end{aligned} \quad (6.7)$$

if  $-a \cos \varphi \leq \mathbf{r} \cdot \mathbf{n}(\varphi) \leq a \cos \varphi$ , and equals 0 otherwise. See Appendix E.

Equation (6.7) is similar to the expression for conventional filtered backprojection methods [86]. The difference is the factor  $\cos \varphi$  of the last equation in (6.7) that does not appear in CT reconstructions. This expression is the 1-D spatial Fourier transform of  $g$ , to which the ramp filter

$$w(\mathbf{r}, \varphi) \triangleq w(\mathbf{r} \cdot \mathbf{n}(\varphi)) = \int d\rho |\rho| e^{j2\pi \rho \mathbf{r} \cdot \mathbf{n}(\varphi)} \quad (6.8)$$

is applied, and the results for each projection angle are summed to reconstruct the impulse response  $\hat{h}$ . The main limitation in our experiment is that the integration variable  $p$  is scaled depending on the rotation angle of the line scatterer. As  $\varphi$  increases from 0 to  $\pi/2$ , the length of the  $p \cos \varphi$  axis decreases from typically 40 mm (the field of view) to 0 mm. If the  $p$  axis was continuously sampled, all information would be recovered with this

approach. However  $p$  is sampled on an interval equal to the array pitch,  $X = 0.2$  mm, i.e.,  $p = mX$ , where typically  $M = 192$ , and therefore information is lost increasingly as  $\varphi \rightarrow \pi/2$ .

To implement the solution of (6.7) numerically, we first replace  $\mathbf{r} \rightarrow (x, y)$  and  $\mathbf{n}(\varphi) \rightarrow (\cos\varphi, \sin\varphi)$ . Thus, the condition  $-a \cos\varphi \leq \mathbf{r} \cdot \mathbf{n}(\varphi) \leq a \cos\varphi$  equivalent to

$$-a \leq x + y \tan \varphi \leq a . \quad (6.9)$$

The line-scatterer angle is discrete in the range from 0 to 180°, e.g.,  $\varphi_n = \pi(2n - 1)/180$  for  $1 \leq n \leq 90$ . For the moment, also set  $|\rho| = 1$ . Then we can combine (6.7) and (6.8) to find the unfiltered backprojection estimate  $h_u$ ,

$$\begin{aligned} \hat{h}_u(x, y) &= \sum_n \int d\rho e^{j2\pi\rho(x \cos \varphi_n + y \sin \varphi_n)} |\cos \varphi_n| G(\rho \cos \varphi_n, \varphi_n) \\ &= \sum_n \hat{h}_u(x, y, \varphi_n) . \end{aligned} \quad (6.10)$$

We define

$$G(\rho \cos \varphi_n, \varphi_n) = \int dp e^{-j2\pi p \rho \cos \varphi_n} g(p, \varphi_n) \quad (6.11)$$

as the 1-D spatial Fourier transform, and  $\hat{h}_u(x, y, \varphi_n)$  as the unfiltered backprojection result for angle  $\varphi_n$ , which can be written as

$$\begin{aligned} \hat{h}_u(x, y, \varphi_n) &= \int d(\rho \cos \varphi_n) e^{j2\pi\rho(x \cos \varphi_n + y \sin \varphi_n)} G(\rho \cos \varphi_n, \varphi_n) \\ &= \int d\rho' e^{j2\pi\rho'(x + y \tan \varphi_n)} G(\rho', \varphi_n) \\ &= g(x + y \tan \varphi_n, \varphi_n) , \quad \text{where } \rho' = \rho \cos \varphi_n . \end{aligned} \quad (6.12)$$

Equation (6.12) describes how to take 1-D projection data and create one unfiltered backprojection line. First, at each  $\varphi_n$ , the data can only be acquired at the field of view, i.e.,  $y = 0$  and  $-a \leq x \leq a$ . In the case of non-zero  $y$ , if  $x + y \tan \varphi_n > a$  or  $x + y \tan \varphi_n < -a$ ,  $\hat{h}_u(x, y, \varphi_n) = 0$  since it does not satisfy the condition of (6.9). Otherwise,  $g(x + y \tan \varphi_n, \varphi_n)$  is interpolated from  $g(x, \varphi_n)$ . Thus, the best strategy at each  $\varphi_n$  is zero-padding  $g(x, \varphi_n)$  so that the projection data can cover the range of  $x + y \tan \varphi_n$ , then interpolating and re-arranging to obtain  $\hat{h}_u(x, y, \varphi_n)$  from  $g(x, \varphi_n)$ . The zero-padding creates a large null space in the sinogram that may limit the reconstruction accuracy of  $\hat{h}$ .

The null space can be filled by increasing  $a$  to  $+\infty$ , or we must be able to obtain

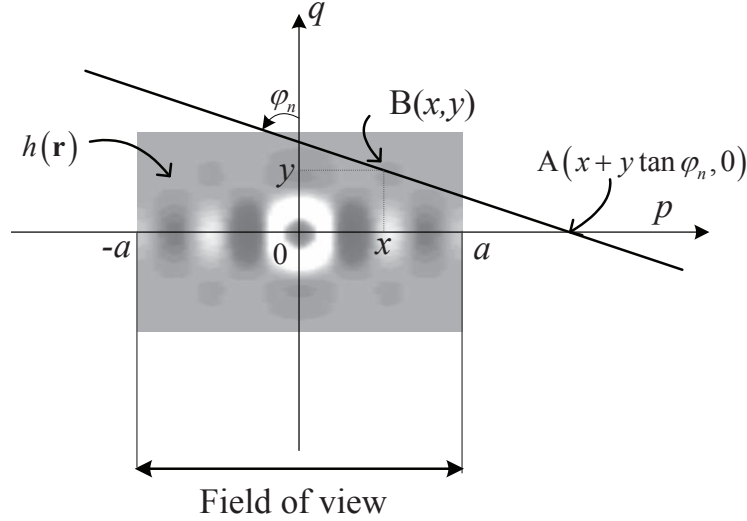


Figure 6.7: The diagram for expanding the range of acquired data by using a 2-D transducer or scanning the 1-D in the elevation direction ( $q$  axis).

the data at  $x + y \tan \varphi_n$  outside the field of view  $[-a, a]$ . Figure 6.7 illustrates the idea. Projecting  $h(x, y)$  at point A out of  $[-a, a]$  is equivalent to projecting it at point B which is inside the interval of  $[-a, a]$ ; however, B is off the  $p$  axis. Mathematically, the equivalence can be proved as follows:

$$\begin{aligned}
 g(x + y \tan \varphi_n, \varphi_n) &= \int \int dx' dy' h(x', y') \delta((x + y \tan \varphi_n) \cos \varphi_n - x' \cos \varphi_n - y' \sin \varphi_n) \\
 &= \int \int dx' dy' h(x', y') \delta((x - x') \cos \varphi_n + (y - y') \sin \varphi_n) \\
 &\triangleq g(x, y, \varphi_n), \tag{6.13}
 \end{aligned}$$

Thus, we can obtain the data outside the field of view by moving the transducer in the elevation direction, or using the 2-D array transducer.

The last two steps of the process are to apply a 1-D ramp filter  $w(\mathbf{r}, \varphi_n)$  from (6.8) to each  $\hat{h}_u(\mathbf{r}, \varphi_n)$  line, i.e., remove the earlier assumption that  $|\rho| = 1$ , and then sum the results over all angles:

$$\hat{h}(\mathbf{r}) = \sum_{\varphi_n} [w * \hat{h}_u](\mathbf{r}) = \left[ w_{2D} * \sum_{\varphi_n} \hat{h}_u \right](\mathbf{r}). \tag{6.14}$$

The second form is preferred because it is computationally faster and mathematically equivalent to applying a 2-D ramp filter to the summation once, rather than applying a 1-D filter to each line. The process is repeated for each range time  $t_1$  to build up a

3-D reconstruction of the impulse response  $\hat{h}(x, y, t_1)$ , as we show in Figure 6.6, but keep in mind that the results are for a single distance,  $z = z_0$ . If we repeat the experiment for different distances, we can find  $\hat{h}(x, y, z, t_1) \simeq h(\mathbf{x}, \mathbf{t})$ , which approximates the full pulse-echo spatiotemporal impulse response for the ultrasonic imaging system.

### 6.3.4 Algebraic reconstruction technique

We do not have a 2-D array transducer for acquiring data. Mechanically translating a 1-D transducer in the elevation direction is time consuming for each angle  $\varphi_n$ . Furthermore, data on a sinogram must have the same phase for reconstructing a cross section. The range time  $t_1$  at a single distance of  $z_0$  of all RF projections must be the same, or at least their differences must be within a temporal resolution of  $1/f_s = 0.025 \mu\text{s}$ , where  $f_s = 40 \text{ MHz}$  is the sampling frequency of the ultrasound machine. It makes the method of scanning 1-D arrays in the elevation direction become infeasible for experimental implementations. Therefore, a reconstruction method that is better adapted to managing the loss of information in each 1-D projection is sought.

The filtered backprojection method reconstructs the object based on the Fourier transform of projections. Since the transducer cannot rotate with the line scatter, however, the integration variable  $p$  was scaled by a factor of  $\cos\varphi$  in the Fourier transform of the projection at angle  $\varphi$ . In comparison with a standard CT reconstruction, the projection in this reconstruction is sampled unevenly with a scale of  $\cos\varphi$ . On the other hand, the total number of samples is fixed and equal to the number of A-scan lines in one RF data frame. This situation leads to truncated or missing projections when  $\varphi$  approaches  $\pi/2$ . It was shown in conventional CT that in such a situation the reconstruction can be amended by using the *algebraic reconstruction technique* (ART) [86, 87]. The method is an iterative process to solve a set of linear equations whose unknowns are elements of the cross section being reconstructed. In [86], ART was introduced along with several other modified versions for improving the performance and speed of implementation, such as the simultaneous iterative reconstructive technique (SIRT) and simultaneous algebraic reconstruction technique (SART). In this study, however, we apply only the simplest technique, ART. Details are provided in [88–90]. The equation that must be solved by ART is given by

$$\mathbf{g} = \mathbf{A}\mathbf{h} , \tag{6.15}$$

in which  $\mathbf{h}$  is a vector column arranged from the discrete cross section  $h(x, y)$ . Matrix  $\mathbf{A}$  is constructed from linear convolutions between  $h(x, y)$  and a rotating line, which mimics

line projections.  $\mathbf{g}$  is a vector column arranged from the sinogram. For solving (6.15), the solution is updated at the  $k^{\text{th}}$  iteration by

$$\mathbf{h}^{(k+1)} = \mathbf{h}^{(k)} + \lambda_k \frac{g_i - \langle \mathbf{a}^i, \mathbf{h}^{(k)} \rangle}{\|\mathbf{a}^i\|_2^2} \mathbf{a}^i, \quad (6.16)$$

in which  $\mathbf{a}^i$  is the  $i^{\text{th}}$  row of matrix  $\mathbf{A}$ ,  $g^i$  is the  $i^{\text{th}}$  component of  $\mathbf{g}$ , and  $\lambda_k$  is the relaxation parameter. Usually  $0 \leq \lambda_k \leq 2$ . The iterative process can be started from an arbitrary vector  $\mathbf{h}^{(0)}$ , and  $\mathbf{h}^{(k)}$  converges to a vector in subspace  $L$  given by

$$L = \bigcap_i \{ \mathbf{h} \mid \langle \mathbf{a}^i, \mathbf{h} \rangle = g_i \}, \quad (6.17)$$

provided that  $L$  is not an empty set [90].

Equation (6.16) can be interpreted as follows. At iteration  $k$ , the reconstructed version  $\mathbf{h}^{(k)}$  is re-projected at the same angles and subtracted from the sinogram. The residual then is back-projected, scaled, and updated to the function. In this process, projections which contain full information (with  $\varphi$  around  $0^\circ$ ) can be utilized through iteration for generating the missing information in truncated projections; therefore, they can contribute more to the reconstructed solution than other projections which are truncated by the limitation of the field of view. The iterations give the ART an advantage over the filtered backprojection method where all projections contribute to the solution equally. Another advantage of ART in comparison to other iterative techniques provided in [91–93] is that there is no interpolation or estimation for missing information from the given set of the projections; therefore, ART can avoid accumulating errors through iterations.

### 6.3.5 Simulation

We applied the Field II Ultrasound Simulation Program [43, 44] to model 3-D impulse responses with typical system parameters of the SONOLINE Antares system. The VF10-5 1-D linear array transducer was modeled. We simulated echo projections  $g(p, t_1, \varphi)$  or  $g(p, q, t_1, \varphi)$  from the linear model of the ultrasonic system [41]. An advantage of simulations is that reconstructions can be verified through comparisons to the original PSFs generated by the Field II program.

The system parameters used to model the PSFs are the same as those used in previous chapters. Range time  $t_1 = \ell T$  is sampled at 40 MHz ( $T = 25$  ns and therefore the spatial range sampling is  $cT/2 = 0.0193$  mm for  $c = 1487$  m/s). The lateral sampling interval,  $X = 0.2$  mm, equals the element pitch. We set a 40-mm transmit/receive focal length

and a 96-element ( $\sim 20$  mm) active aperture. The array has 192 total elements separated by a 0.02 mm kerf. The elevational element length is  $Y = 25$  mm. We applied a two-cycle excitation voltage to the transducer and found a nearly Gaussian-shaped pulse-echo amplitude spectrum with a 53% bandwidth that is centered at  $\sim 7$  MHz. Since Field II is most accurate in the focal zone and far-field, we generated PSFs at spatial positions  $\mathbf{x} = (0, 0, 40 \text{ mm})$  and  $(0, 0, 60 \text{ mm})$ . These PSFs are shown in Figures 6.8(a) and 6.9(a), respectively. Since the responses are three dimensional, we display the pressure amplitudes separately in the axial-lateral plane (elevational cut) and the lateral-elevational plane (axial cut). Projection data are recorded along the  $p$  axis for a 1-D transducer array, or both the  $p$  and  $q$  axes for 2-D array (see Figure 6.1). In each case, projections were acquired at 90 angular locations,  $1^\circ \leq \varphi \leq 179^\circ$  in steps of  $2^\circ$ , and no measurement noise was added.

The reconstruction procedure is as follows. Recall that the  $p$  axis is sampled,  $p = mX$  for  $-M/2 \leq m \leq M/2$ , where the pitch of the array is  $X = 0.2$  mm and there are  $M = 192$  total array elements and 192 A-scan lines. We will adopt the same sampling interval for the  $y$  axes, such that  $x = mX$  and  $y = m'X$ . For 2-D array reconstruction,  $\hat{h}_u(m, m', \varphi_n)$  can be obtained directly from projection data as we step along  $m$  and  $m'$ . For 1-D array reconstruction, we go to  $g(m + m' \tan \varphi_n, \varphi_n)$  interpolated from  $g(m, \varphi_n)$ . However, values of  $m + m' \tan \varphi_n$  that extend outside the range  $-M/2 \leq m' \leq M/2$  must be set to zero because we have no values to interpolate, and information is lost. For ART, we start from the solution of a 1-D array. The relaxation parameter is set to 0.25, and the number of iterations is 50. Every row of matrix A is scanned once in each iteration. The results from 2-D array and 1-D array reconstructions, as well as from ART, are shown in Figures 6.8(b,c,d) and 6.9(b,c,d) for the PSFs at focal and far-field respectively.

On the figures, we can see that there are errors in the 1-D array reconstruction. The errors are acceptable in the focal region when the PSF is compact. However, they become severe at far-field as the PSF is broadened. In the axial cut of Figures 6.9(c), the two ends in the elevational axis of the phase rings are not reconstructed completely due to missing information. These errors generate artifacts along the lateral axis in the corresponding elevational cut. By using ART, those rings can be fully recovered and the artifacts in the elevational cut are also removed. The results from ART are on par or even better than those from 2-D array reconstruction. However, iterations of ART create some noise in the background of the reconstructed images. That reconstruction noise can be observed clearer on the axial cut of Figures 6.8(d).

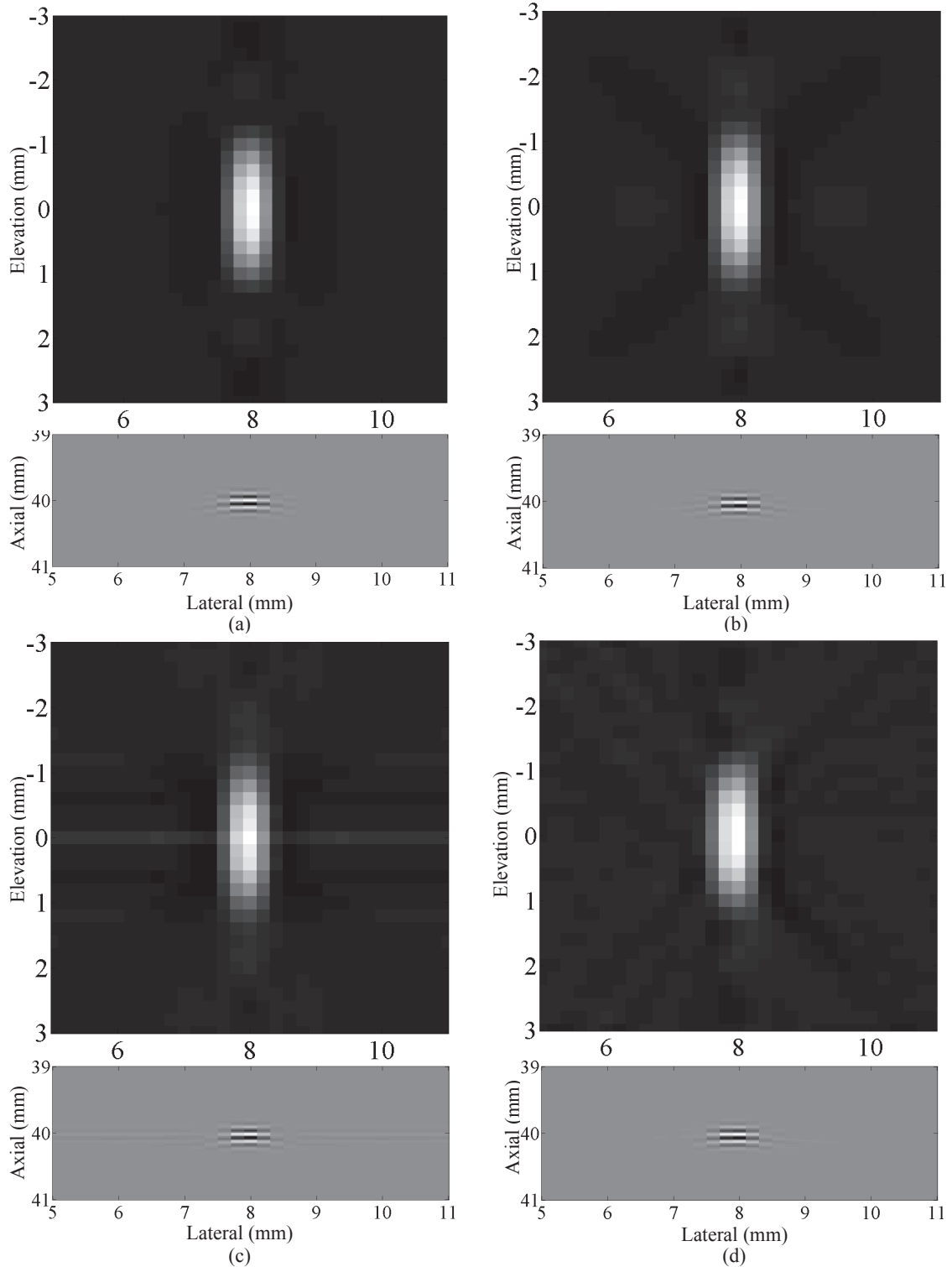


Figure 6.8: 3-D pulse-echo spatiotemporal impulse responses positioned at focal region of  $(0, 0, 40 \text{ mm})$  is generated by using the Field II program (a), reconstructed by using 2-D projections (b), reconstructed by using 1-D projections (c), and reconstructed by using the ART at each cross section (d). The 3-D function is displayed by the axial cut at 40 mm and the elevation cut at the origin.

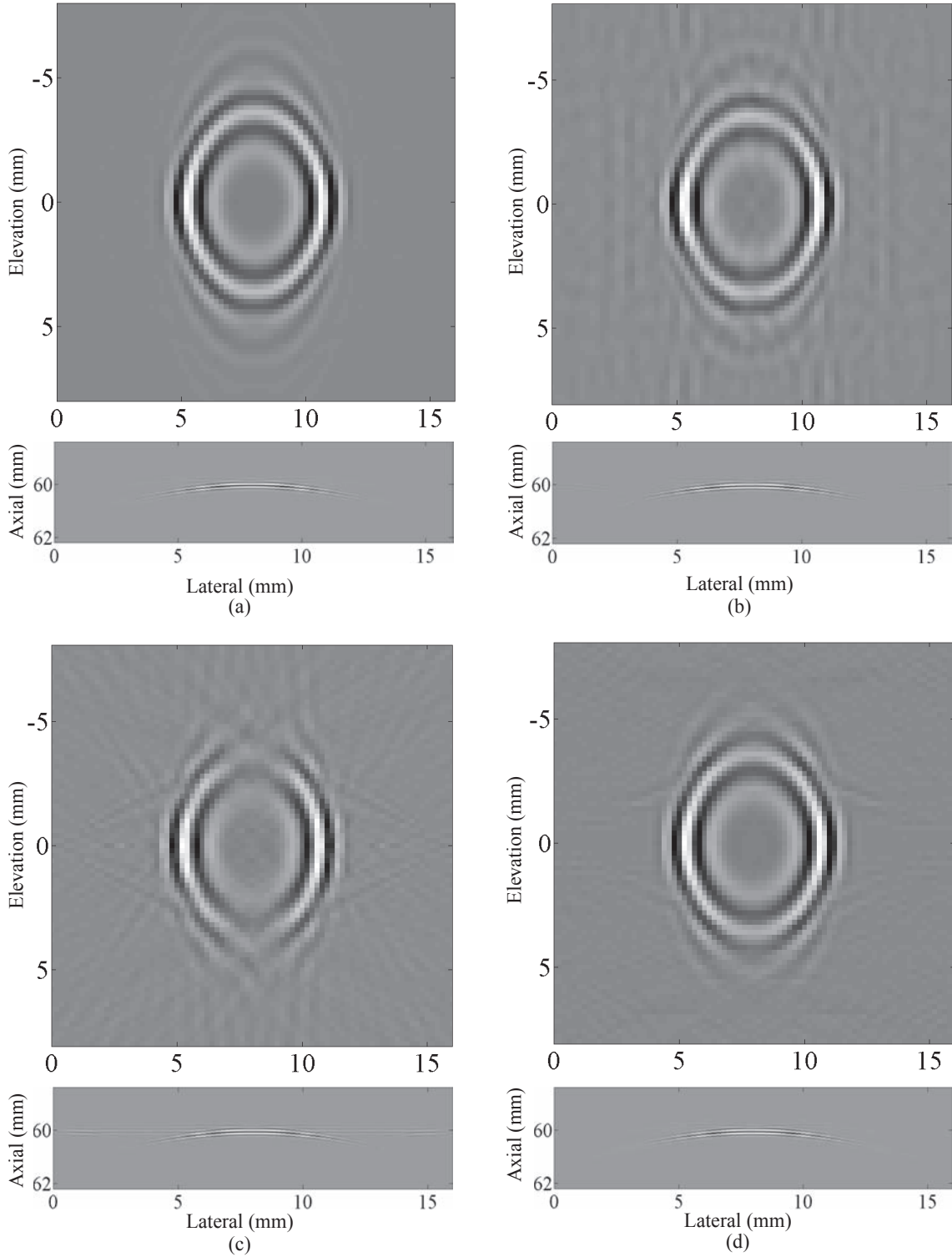


Figure 6.9: 3-D pulse-echo spatiotemporal impulse responses positioned at far-field of  $(0, 0, 60 \text{ mm})$  is generated by using the Field II program (a), reconstructed by using 2-D projections (b), reconstructed by using 1-D projections (c), and reconstructed by using the ART at each cross section (d). The 3-D function is displayed by the axial cut at  $60 \text{ mm}$  and the elevation cut at the origin.

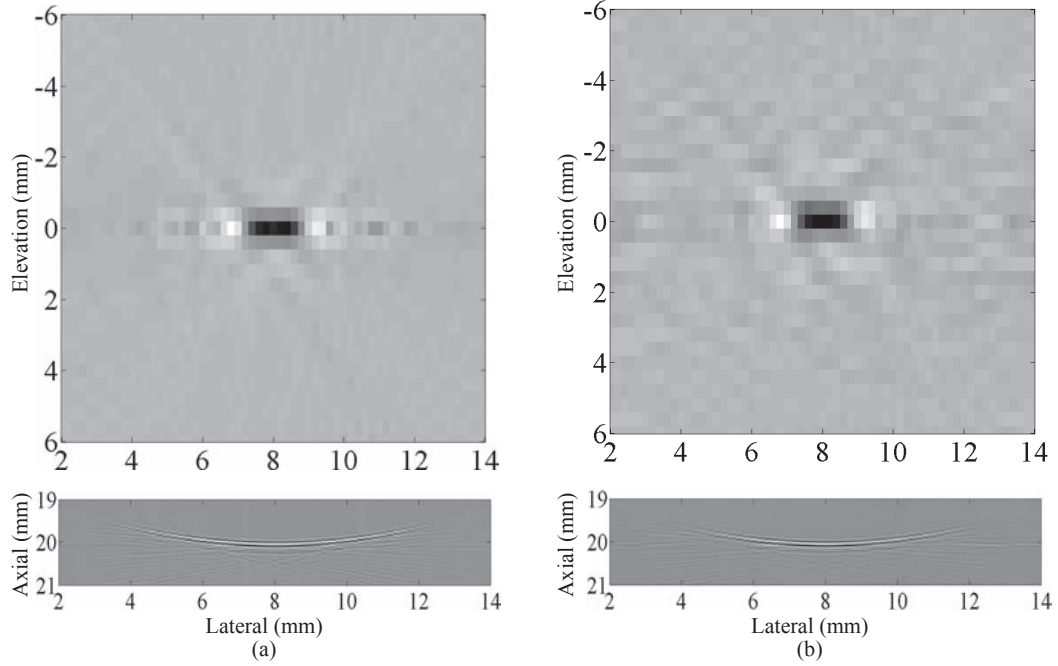


Figure 6.10: A 3-D PSF in near-field as reconstructed from experimental data with (a) 1-D array projection and (b) ART. The 3-D function is displayed by the axial cut at 20 mm and the elevation cut at the origin.

### 6.3.6 Experimental implementation

We recorded measured RF echo signals  $g(p, t_1, \varphi)$  by fixing a line scatterer and rotating a linear array transducer that was mounted in a fixture that provides positioning accuracy. The line scatterer was a 100  $\mu\text{m}$ -diameter metal wire placed in degassed water at room temperature. All of the system parameters and geometric details described above for simulations were applied experimentally. Dynamic focusing and aperture growth were disabled on the system. The echo SNR of the system relative to the wire echo was approximately 32 dB for each recorded frame. However, at each angle, we acquired 100 RF frames that were averaged to reduce the effects of electronic noise. The echo SNR for the averaged projections increased to 52 dB, and thus we considered the RF data to be noiseless.

The reconstructed PSFs from the measurement at the 20 mm, 40 mm, and 60 mm distances are shown in Figures 6.10, 6.11, and 6.12, respectively. They correspond to near-field, focal region, and far-field of an  $f/2$  in-plane aperture. The 2-D array transducer is not available in the lab, and we also do not scan 1-D arrays in the elevation direction due to errors added in long acquisition. Each PSF at those locations is reconstructed by using 1-D array reconstruction and then amended using ART. The 1-D

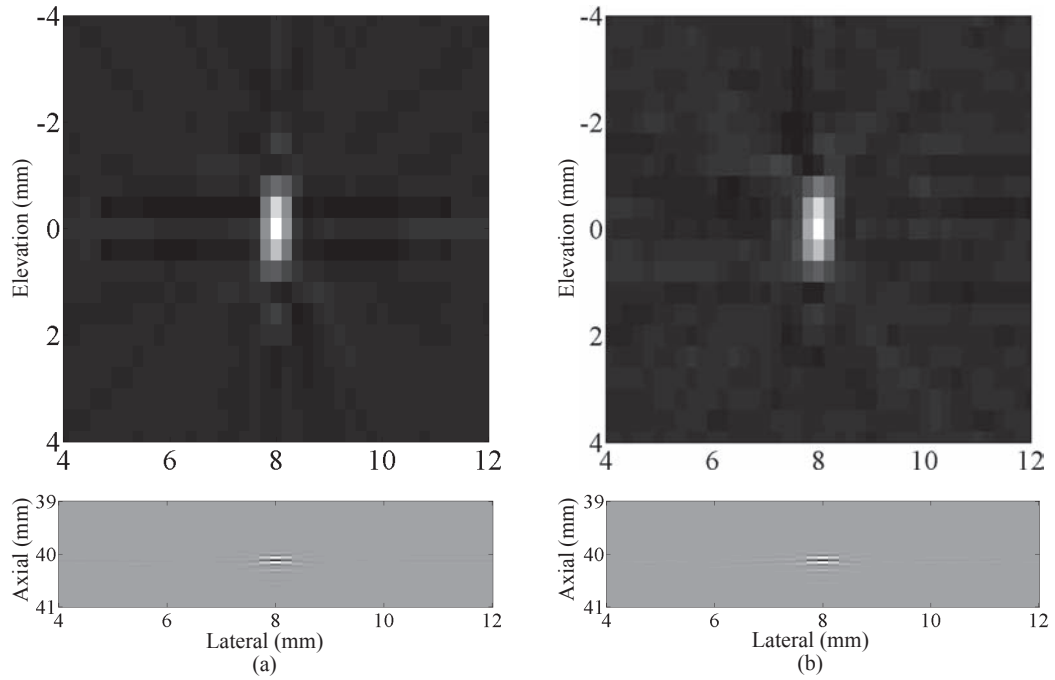


Figure 6.11: A 3-D PSF in focal region as reconstructed from experimental data with (a) 1-D array projection and (b) ART. The 3-D function is displayed by the axial cut at 40 mm and the elevation cut at the origin.

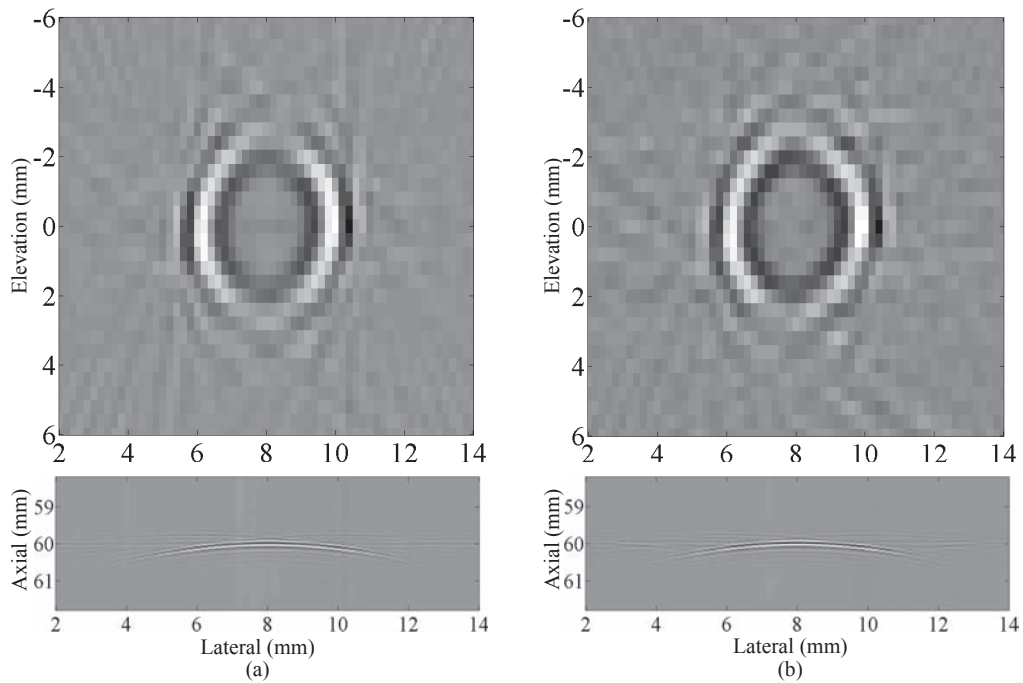


Figure 6.12: A 3-D PSF in far-field as reconstructed from experimental data with (a) 1-D array projection and (b) ART. The 3-D function is displayed by the axial cut at 60 mm and the elevation cut at the origin.

array reconstruction results have errors due to the missing information as observed with simulation results. Besides, additional errors come from the misalignment between the line scatterer and the transducer. ART is implemented on experimental data beginning with a 1-D reconstruction; however, the improvements on experimental data are not as much as those obtained in simulation. In the focal region, the field pattern in the axial cut of Figure 6.11(b) is somewhat worse because it is a little affected by background noise from ART. However, ART makes some improvements on the axial cut of PSF in far-field (Figure 6.11(c)) as the phase patterns become clearer by comparison with the results from 1-D array reconstruction.

## 6.4 Discussion

By comparison with the first technique of scanning glass spheres suspended in gelatin, the line scatterer is easier to position at known distances, and provides much stronger scattering signals. The high eSNR of the line scattering signal allows a clearer visualization of the phase changes on reconstructed results of the lateral-elevation plane. However, in the far-field, where the function is less compact, the 1-D array reconstruction could not reconstruct the PSF well along the elevational direction. Reconstruction errors are caused by missing data in the sinogram. The line scatterer also creates ringing effects in the axial direction that have not been observed with measurements of scanning scatters.

The filtered backprojection reconstruction from data acquired using a 1-D array is effective when the data are sampled uniformly and contribute equally to the reconstruction. In our problem, since the transducer could not rotate with the line scatterers, projection data are truncated or even limited when the scanned angle is about  $\pi/2$ . For this case, ART can be implemented as a supplement to 1-D array reconstruction to amend the result. Although results from ART have many improvements over 1-D array reconstruction, the technique does not work effectively on experimental data for several reasons. Matrix A modeling used for iterations is constructed from linear convolutions between axial cuts of the 3-D PSF and a rotating line. It models interference between sound pressure and the line scatterer. However, the sound pressure is a continuous signal. Modeling the interference process discretely with the sparse sampling interval of 0.2 mm may not be accurate and can have adverse effects on results. Better matrix A modeling for the interference is needed. Another reason is the presence of errors in projection data. Errors arise from the misalignment between the line scatterer and the transducer surface, and any changes in the water temperature during acquisition.

With the sampling frequency of 40 MHz, the axial sampling interval is about 0.02 mm. This resolution requires a precise alignment of the line perpendicular to the ultrasound beam axis. Otherwise, we cannot form a sinogram correctly. We found under the standard laboratory conditions that projection data in far-field are shifted by 3 pixels in distance if the water temperature changes by  $0.1^\circ$ . Thus, this method needs significant automation for fast, efficient implementation. Nevertheless, it still provides an analysis for reconstruction the 3-D pulse-echo spatiotemporal impulse response. The function is necessary for constructing a deconvolution filter or a beamformer of the RF data. The results also describe the acoustic field in the lateral-elevational plane, which can be useful for optimizing transducer design or in developing techniques for image improvement and tissue characterization.

# CHAPTER 7

## CONCLUSIONS

### 7.1 Summary

The ability of modern ultrasonic systems to digitize and store RF echo signals has increased the flexibility of processing the data before computing final B-mode images. Assessment of a new re-configured system or a processing algorithm applied to data in medical imaging research, however, is complicated. Individual physical parameters, such as contrast and resolution, are incomplete characterizations because they do not fully consider the compromise among the metrics that all contribute to address various clinical tasks. This dissertation provides the analytical framework that connects engineering tradeoffs for system design directly to diagnostic performance on achieving specific tasks. The main contributions of this dissertation are summarized below.

DEVELOP OBJECTIVE ASSESSMENT OF SONOGRAPHIC DATA. Extending the ideal observer acting on the RF data introduces new analytical challenges to the framework. Due to physical properties of sound-tissue interactions, important features for the breast cancer diagnosis are embedded in the spatial fluctuations of the scattering signals. This RF data modeling leads to a quadratic form of the test statistic. Under the nonlinear form, the normal distribution for the test statistic may be lost, and connection of the diagnostic performance to engineering metrics of the imaging system, developed rigorously for photon imaging modalities, becomes uncertain. By relating the Kullback-Leibler divergence to the area between the two probabilities of detection and false alarm curves, we have proposed the use of the divergence to index the ideal performance. Under the normally distributed test statistic, the information metric is proved analytically to equal the  $\text{SNR}_I$ , a metric that quantifies the ideal performance through the separation of the ideal observer responses for each class of data. When the normality condition is lost, which happens in some sonographic tasks, the metric is found numerically as a better representation for the ideal performance. The new interpretation allows us to establish the AIS concept for sonography equivalent to the NEQ from radiography. The AIS describes the efficiency

of transferring diagnostic information from the object to RF data over spatial frequency, providing a foundation for medical ultrasonic imaging system design. AIS also provides a convenient method to compute the ideal performance without using Monte Carlo studies. The nature of sound-tissue interactions changes the source of object contrast in sonography, which means that AIS has a more complicated frequency structure than NEQ in radiography. This treatment is focused on the acquisition stage of image formation that can only help designers adjust acquisition parameters to maximize RF data information. Some signal processing algorithms are needed to ensure accessibility of the information to human observers at final B-mode images.

POST-PROCESSING. Another challenge is calculating the inverses of covariance matrices with high dimensionality in the quadratic form of the ideal observer. The computation was first accomplished by using the power series expansion for each inversion, in which the covariance matrix is decomposed into background and task components. Analysis of the power-series expansion at one iteration first reveals the role of Wiener filtering in the RF domain before computing the envelope image. The resulting envelope images yield measurable improvements in human observer performance when the task is detecting a low-contrast lesion or discriminating different features on the lesion boundary. However, performance was reduced when observers were asked to discriminate anechoic and hypoechoic lesions. In that task, the condition for the accurate first-order approximation is found to be violated. A better first-order approximation was made. The new approximation leads us to the iterative Wiener filter, which is a combination the Wiener filter with an iterative process to adaptively tune the echo statistics wherever there is diagnostic information. The iterative Wiener filter makes improvements on human observer performance in all tasks at the cost of computation. Those filters are then implemented on experimental data where the results include a realistic shift-variant for the pulse-echo spatiotemporal impulse response.

BEAMFORMING. The ideal observer framework is extended to each element of the transducer to find optimal beamforming strategies for specific tasks. The goal of beamforming is to maximize the diagnostic information content of the acquired data, while the goal of post-processing is to maximize the efficiency at which observers can access diagnostic information. Through the analysis, we found that the MV beamformer can be decomposed into two processes, the matched filtering following by an inverse operator. While the matched filtering compresses RF signals from individual channels into a single RF signal without losing any diagnostic information, the inverse operator maximizes the di-

agnostic information through demodulation. The inverse has emerged from a first-order approximation of the ideal observer for pre-beamformed RF data. Efforts at improving the approximation yield the WF beamformer. The comparison between beamformers is made by using the basic metrics of lesion contrast and resolution, and also through the panel of five sonographic tasks. Through the ideal observer analysis, we found the WF outperforms the MV in the first four tasks. But like the Wiener filter for DS beamformed RF data, the WF beamformer does not work effectively in Task 5 of anechoic/hypoechoic discrimination, where the corresponding first-order approximation is violated by the task condition. Implementation of the MV beamformer requires low-rank approximation that handicaps performance for discriminating four of five lesion features, but performs well for Task 5 because reducing rank filters data that is well matched to the feature spectrum. First-order approximations may reduce the potential gains in task performance; therefore, the final results should be evaluated by using human observer studies.

MEASUREMENTS OF THE 3-D PULSE-ECHO SPATIOTEMPORAL IMPULSE RESPONSE SYSTEM. We follow a linear pulse-echo model describing the RF data to propose two methods to measure the function. The first method scans a gelatin gel volume which contains 0.04 mm glass spheres mimicking scatterers. The second method reconstructs the function from 1-D transducer RF data of line scatter echoes. This method is similar to the reconstruction problem in standard CT, but the data projections now are limited and sampled unevenly when transformed into the spatial frequency domain. The reconstructed result from the filtered backprojection method therefore has a large error caused by the missing information in the data. The result can be amended by using the ART method as a supplemental step. ART is shown to make many improvements in simulation, but does not help much on experimental data. The reasons may be from errors in modeling the interference between the ultrasound beam and the rotating line, misalignment between the beam axis and the line, or from errors added during the long data acquisition process. The reconstruction method requires significant automation for efficient implementation.

## 7.2 Future work

The applications in this research have been to optimizing breast cancer diagnosis, but the concepts are generally applicable. While much is known on this topic in radiography and other photon-based medical imaging methods, the subject is far from mature in sonography. There are several reasons for this limitation. Besides those generated

from the quadratic form of the ideal observer in the acquisition stage and resolved in this dissertation, another reason is the use of nonlinear processing in the display stage, which complicates system modeling and statistical analysis. In the following we give an overview of the ongoing and future research directions.

**IDEAL OBSERVER OF B-MODE IMAGES.** Currently, we have approximated the model developed by Smith and Wagner as the ideal observer acting on the B-mode image to disambiguate effects of computing an envelope from those of the human observer. This is an exact ideal observer for low-contrast detection under assumptions of no acquisition noise and speckle spots rather than pixels determining statistical properties of imaging data. A more accurate model should be derived from the log-likelihood ratio between pdf's of multivariate Rayleigh distributions [94]. If the test statistic can be computed, we are able to obtain the task information through (3.28). Note that we prove (3.28) for any log-likelihood ratio. The exact ideal observer allows us to calculate an accurate information loss through demodulation, as well as to get a better evaluation of the human observer's ability to access the information. The ideal observer framework on the envelope image also provides an opportunity to derive the AIS of the B-mode. That AIS will describe the efficiency of transferring information from the object inside the patient's body to the final images of the sonographic system.

**RECOVERING PHASE INFORMATION FROM RF DATA.** The information spectrum of RF data has three lobes: one main lobe at the origin and two other side lobes at higher spatial frequencies. We show in Chapter 4 through ideal observer analysis of the sine-wave detection that the information at the side-lobes could not be displayed on the B-mode image even with support from Wiener filtering of the RF domain. Information in the side lobe of the AIS is conveyed by the phase component of RF data discarded through a simple demodulation. How to recover the information for use in medical applications remains to be investigated. One potential method is to color coded the information and overlay it on top of the standard B-mode image (as in Doppler imaging).

**MODELING HUMAN OBSERVER.** The ideal observer has the ability to access diagnostic information in data after complex transformations that the human observer may not be able to do. Therefore, it is crucial that the information content measured by the ideal observer is visually accessible to the human observer. Accessibility can be quantified from observer efficiency estimates obtained through psychophysical studies, which are usually costly, time consuming, and unstable due to the internal noise in human eye-brain systems. To

minimize time and expense associated with human studies, we should develop computational techniques that accurately predict the human response to ultrasound breast images. That model, if successfully developed, would also reveal a compatible strategy of processing data with the human eye-brain for diagnostic purposes. Human observer performance is limited by sampling efficiency [95], internal noise [96], and nonlinear effects such as spatial uncertainty [97, 98]. Research from other medical imaging modalities shows that the Hotelling observer [99] – an optimal linear (in the data) observer – is a good predictor of human responses in some cases [100], which can be applicable to sonograms.

EXTENDING THE BEAMFORMING FRAMEWORK TO OTHER MODALITIES. A new contribution of this dissertation to the ideal observer analysis is the derivations of beamformers from first-order approximations of the ideal strategies. In ultrasonic systems, the advances in technology of going from single-element to array transducers is analogous to those from X-ray projections to computed tomography (CT), from nuclear magnetic resonance (NMR) to magnetic resonance imaging (MRI), and from planar single-photon emission imaging to single-photon emission computed tomography (SPECT). Using multiple imaging planes allows larger scanning coverage of the object. A question left is how to combine those plane together to form a higher spatial resolution image for the medical systems. Beamforming in sonography as well as the reconstruction in other modalities, essentially arises from a solution of the linear inverse problems under specific physical conditions. Therefore, the ideal observer analysis we developed for finding optimal beamformers can be applicable in other medical imaging modalities with some modifications in observer modeling. The modifications are to amend the difference in physical properties from the interactions between tissue and media. The modification step will be the most challenging part of the work.

Currently, X-ray mammography is still a standard imaging method for breast cancer screening. However, radiography employs ionizing radiation that demands very careful use. In addition to diagnostic errors, use of X-ray and gamma-ray imaging carries significant patient risks. The risks associated with sonography, fortunately, are much lower. Designers of this low-cost modality have not had to face the same economic and safety design pressures that spawned development of rigorous image quality analysis in radiography. Once such an analysis is also available in sonography, the industry will have better tools to address the value and limitations imposed by the current output-power limits. In addition, ever greater computational power means that systems can be quickly reconfigured for different patient body types and exam requirements, which can improve

diagnostic performance with little increased cost. Yet this can occur only when an analytical framework based on the ideal observer analysis is available in medical sonography.

# APPENDIX A

## RELATION OF $\text{SNR}_I$ TO THE IDEAL OBSERVER AUC

Appendix A proves the relation between  $\text{SNR}_I$  and the IO performance in (2.23) under the normal distribution for the test statistic. More details of the proof are provided in [8, 15]. First, the step function in (2.19) can be written in the Fourier domain as

$$\text{step}(x) = \frac{1}{2} + \frac{1}{2\pi i} \mathcal{P} \int_{-\infty}^{\infty} \frac{d\xi}{\xi} \exp(2\pi i \xi x), \quad (\text{A.1})$$

where  $\mathcal{P}$  indicates that the integral is interpreted as a Cauchy principal value. The Cauchy principal value integral is used to avoid the singularity on the path of the integration. Then, the expression in the second line of (2.19) becomes

$$\begin{aligned} \text{AUC} &= \frac{1}{2} + \frac{1}{2\pi i} \mathcal{P} \int_{-\infty}^{\infty} \frac{d\xi}{\xi} \int_{-\infty}^{\infty} dx q_0(x) \int_{-\infty}^{\infty} dt q_1(t) \exp[2\pi i \xi(t - x)] \\ &= \frac{1}{2} + \frac{1}{2\pi i} \mathcal{P} \int_{-\infty}^{\infty} \frac{d\xi}{\xi} \psi_{\lambda_0}(\xi) \psi_{\lambda_1}^*(\xi), \end{aligned} \quad (\text{A.2})$$

where  $\psi_{\lambda_j}(\xi)$  is the characteristic function of  $\lambda$  under hypothesis  $H_j$  ( $j = 0, 1$ ),

$$\psi_{\lambda_j}(\xi) = \int_{-\infty}^{\infty} d\xi q_j(t) \exp(-2\pi i \xi t). \quad (\text{A.3})$$

Under the normal distribution for the test statistic  $\lambda$ , the characteristic function is given by

$$\psi_{\lambda_j}(\xi) = \exp(-2\pi i \bar{\lambda}_j \xi - 2\pi^2 \sigma_j^2 \xi^2), \quad (\text{A.4})$$

in which  $\bar{\lambda}_j$  and  $\sigma_j^2$  are mean and variance of  $\lambda$  under hypothesis  $H_j$ . The AUC in (A.2) then becomes

$$\begin{aligned}
\text{AUC} &= \frac{1}{2} + \frac{1}{2\pi i} \mathcal{P} \int_{-\infty}^{\infty} \frac{d\xi}{\xi} \exp \left[ -2\pi i (\bar{\lambda}_0 - \bar{\lambda}_1) \xi - 2\pi^2 (\sigma_0^2 + \sigma_1^2) \xi^2 \right] \\
&= \frac{1}{2} + \frac{1}{2\pi} \mathcal{P} \int_{-\infty}^{\infty} \frac{d\xi}{\xi} \sin \left[ 2\pi (\bar{\lambda}_1 - \bar{\lambda}_0) \xi \right] \exp \left[ -2\pi^2 (\sigma_0^2 + \sigma_1^2) \xi^2 \right] \\
&= \frac{1}{2} + (\bar{\lambda}_1 - \bar{\lambda}_0) \int_{-\infty}^{\infty} d\xi \text{sinc} \left[ 2\pi (\bar{\lambda}_1 - \bar{\lambda}_0) \xi \right] \exp \left[ -2\pi^2 (\sigma_0^2 + \sigma_1^2) \xi^2 \right]. \quad (\text{A.5})
\end{aligned}$$

Applying Parseval's theorem to the last expression, we obtain

$$\begin{aligned}
\text{AUC} &= \frac{1}{2} + \frac{1}{2\sqrt{2\pi(\sigma_0^2 + \sigma_1^2)}} \int_{-\infty}^{\infty} dx \text{rect} \left[ \frac{x}{2(\bar{\lambda}_1 - \bar{\lambda}_0)} \right] \exp \left[ -\frac{x^2}{2(\sigma_0^2 + \sigma_1^2)} \right] \\
&= \frac{1}{2} + \frac{1}{\sqrt{2\pi(\sigma_0^2 + \sigma_1^2)}} \int_0^{(\bar{\lambda}_1 - \bar{\lambda}_0)} dx \exp \left[ -\frac{x^2}{2(\sigma_0^2 + \sigma_1^2)} \right]. \quad (\text{A.6})
\end{aligned}$$

With the error function given by

$$\text{erf}(x) = \frac{2}{\sqrt{\pi}} \int_0^x \exp(-t^2) dt, \quad (\text{A.7})$$

Equation (A.6) yields the relationship of (2.23) by a change of the variable inside the integral.

# APPENDIX B

## SUPPORTING MATERIAL FOR CHAPTER 3

### B.1 Proof of (3.28)

In this section of Appendix B, we derive (3.28) that relates the  $J$  to the area between the detection and false-alarm probability curves as functions of the decision threshold. Integrating by parts the right-hand side (RHS) of (3.28) gives us

$$\int_{-\infty}^{\infty} dt \{P_D(t) - P_F(t)\} = t \{P_D(t) - P_F(t)\} \Big|_{-\infty}^{\infty} - \int_{-\infty}^{\infty} t d\{P_D(t) - P_F(t)\}. \quad (\text{B.1})$$

To evaluate the first term on the RHS of (B.1), we apply the Chernoff bound to have [46]

$$\begin{aligned} P_D(t) &= \Pr(\lambda(\mathbf{g}) > t | H_1) \\ &< e^{-\beta t} M_1(\beta), \text{ for any } \beta > 0 \end{aligned} \quad (\text{B.2})$$

where  $M_i(\beta)$  is the moment-generating function underlying  $H_i$ , given by [15]

$$M_i(\beta) = \int_{-\infty}^{\infty} d\lambda q_i(\lambda) \exp(\beta\lambda), \quad i = 0, 1. \quad (\text{B.3})$$

For  $t \rightarrow +\infty$ ,  $t e^{-\beta t} \rightarrow 0$  since the decrease in  $e^{-\beta t}$  is much faster than the increase in  $t$ ,  $M_1(\beta)$  remains unchanged; therefore,  $t P_D(t) \rightarrow 0$ . Similarly,  $t P_F(t) \rightarrow 0$ ; therefore  $t \{P_D(t) - P_F(t)\} \rightarrow 0$  as  $t \rightarrow +\infty$ .

For  $t \rightarrow -\infty$ , by changing variable  $t$  to  $t' = -t$ , the first term on the RHS of (B.1) can be written as

$$\begin{aligned} &t \{P_D(t) - P_F(t)\} \\ &= t' \{ \Pr(-\lambda(\mathbf{g}) > t' | H_1) - \Pr(-\lambda(\mathbf{g}) > t' | H_0) \}. \end{aligned} \quad (\text{B.4})$$

By noting that  $-\lambda(\mathbf{g}) = \ln[p_0(\mathbf{g})/p_1(\mathbf{g})]$  is also a log-likelihood ratio and  $t' \rightarrow +\infty$ , therefore, the Chernoff bound is still applicable to  $-\lambda(\mathbf{g})$  and  $t'$ . Hence, we have  $t\{P_D(t) - P_F(t)\} \rightarrow 0$  as  $t \rightarrow -\infty$ .

Thus, there is only the second term left in the RHS of (B.2). Combining with

$$\frac{d}{dt}\{P_D(t)\} = -q_1(t) \text{ and } \frac{d}{dt}\{P_F(t)\} = -q_0(t) , \quad (\text{B.5})$$

the RHS of (B.1) becomes

$$\begin{aligned} & - \int_{-\infty}^{\infty} t d\{P_D(t) - P_F(t)\} = \int_{-\infty}^{\infty} t [q_1(t) - q_0(t)] dt \\ & = \int d\mathbf{g} (p_1(\mathbf{g}) - p_0(\mathbf{g})) \ln \frac{p_1(\mathbf{g})}{p_0(\mathbf{g})}. \end{aligned} \quad (\text{B.6})$$

Combining with the definition of  $J$  in (3.27), we have proved the equality of (3.28).

## B.2 Proof of (3.30)

In this section,  $J$  is related to the moments of the log-likelihood ratio  $\lambda$  under a normal distribution for  $q_0(\lambda)$ . We invoke the *exponential family of distributions*  $p_\tau(\mathbf{g})$  [52],

$$p_\tau(\mathbf{g}) = \frac{p_0(\mathbf{g}) e^{\tau\lambda(\mathbf{g})}}{M_0(\tau)} , \quad (\text{B.7})$$

for  $0 \leq \tau \leq 1$ .  $M_0(\tau)$  is defined as the moment-generating function under hypothesis  $H_0$  [15] but in (B.7) it serves as a normalization constant for pdf  $p_\tau(\mathbf{g})$ .

Denoting  $q_\tau(\lambda)$  as another exponential family for variable  $\lambda$  corresponding to each distribution of  $p_\tau(\mathbf{g})$ , we show that if  $q_0(\lambda)$  is normally distributed, then all distributions of  $q_\tau(\lambda)$  must also be normally distributed with the same variance.

The moment-generating function  $M_\tau(\beta)$  underlying  $p_\tau(\mathbf{g})$  can be written as

$$\begin{aligned} M_\tau(\beta) &= \int_{-\infty}^{\infty} d\mathbf{g} p_\tau(\mathbf{g}) e^{\beta\lambda(\mathbf{g})} \\ &= \frac{M_0(\beta + \tau)}{M_0(\tau)}, \end{aligned} \quad (\text{B.8})$$

in which the second expression is obtained by combination with (B.7). The corresponding

characteristic function for  $\lambda$  is given by

$$\psi_\tau(\xi) = \int_{-\infty}^{\infty} d\mathbf{g} p_\tau(\mathbf{g}) e^{-2\pi i \xi \lambda(\mathbf{g})}. \quad (\text{B.9})$$

Comparing (B.3) and (B.9) gives us

$$M_\tau(\beta) = \psi_\tau\left(\frac{i\beta}{2\pi}\right). \quad (\text{B.10})$$

Replace  $\beta = -2\pi i \xi$  and combine with (B.10) to obtain

$$\psi_\tau(\xi) = \frac{1}{M_0(\tau)} \psi_0\left(\xi + \frac{i\tau}{2\pi}\right). \quad (\text{B.11})$$

Taking the inverse Fourier transform of (B.11), we have

$$q_\tau(\lambda) = \frac{e^{\tau\lambda}}{M_0(\tau)} q_0(\lambda), \quad 0 \leq \tau \leq 1. \quad (\text{B.12})$$

Equation (B.12) shows a relation among distributions of family  $q_\tau(\lambda)$ . If  $\lambda$  is normally distributed under hypothesis  $H_0$ ,  $q_0(\lambda)$  can be written as

$$q_0(\lambda) = \frac{1}{\sqrt{2\pi}\sigma} e^{-\frac{(\lambda-\bar{\lambda}_0)^2}{2\sigma^2}}, \quad (\text{B.13})$$

where  $\bar{\lambda}_0$  and  $\sigma_0^2$  are the mean and variance of the distribution. Substituting (B.13) into (B.12), we have

$$q_\tau(\lambda) = \frac{e^{\tau\bar{\lambda}_0 + \frac{\tau^2\sigma_0^2}{2}}}{M_0(\tau)} \frac{1}{\sqrt{2\pi}\sigma_0} e^{-\frac{(\lambda-\bar{\lambda}_0-\tau\sigma_0^2)^2}{2\sigma_0^2}}, \quad (\text{B.14})$$

where  $M_0(\tau) = e^{\tau\bar{\lambda}_0 + \frac{\tau^2\sigma_0^2}{2}}$  is the moment generating function [8]. Thus,  $q_\tau(\lambda)$  is also Gaussian with the same variance  $\sigma_0^2$ .

This result is consistent with the finding of Barrett et al. [15]. They showed that if the log-likelihood ratio is normally distributed under one hypothesis, it is necessarily normally distributed under the other with the same variance. This result is more general because the property is applied to any distribution in the family of  $\{q_\tau(\lambda) : 0 \leq \tau \leq 1\}$  including  $q_1(\lambda)$ .

To derive (3.30), we continue by introducing the *cumulant-generating function*  $L_0(\tau) =$

$\ln M_0(\tau)$  [8, 15], and taking its first derivative to obtain

$$\begin{aligned} L'_0(\tau) &= \frac{M'_0(\tau)}{M_0(\tau)} \\ &= \frac{1}{M_0(\tau)} \int_{-\infty}^{\infty} d\mathbf{g} \lambda(\mathbf{g}) p_0(\mathbf{g}) e^{\tau \lambda(\mathbf{g})}. \end{aligned} \quad (\text{B.15})$$

Combining with (B.7), the second expression in (B.15) is recognized as  $\bar{\lambda}_\tau$ , the conditional mean of  $\lambda$  underlying  $p_\tau(\mathbf{g})$ . By denoting  $\theta(\tau) = L'_0(\tau)$ , we obtain

$$\theta(\tau) = \bar{\lambda}_\tau = \frac{M'_0(\tau)}{M_0(\tau)}. \quad (\text{B.16})$$

Taking the derivative of (B.16), we have

$$\begin{aligned} \theta'(\tau) &= \frac{M''_0(\tau)}{M_0(\tau)} - \left( \frac{M'_0(\tau)}{M_0(\tau)} \right)^2 \\ &= \frac{1}{M_0(\tau)} \int_{-\infty}^{\infty} d\mathbf{g} \lambda^2(\mathbf{g}) p_0(\mathbf{g}) e^{\tau \lambda(\mathbf{g})} - \bar{\lambda}_\tau^2. \end{aligned} \quad (\text{B.17})$$

The integral in (B.17) is the second moment of  $\lambda(\mathbf{g})$  underlying  $p_\tau(\mathbf{g})$ . Therefore,

$$\theta'(\tau) = \text{var}_\tau(\lambda) = \sigma_0^2. \quad (\text{B.18})$$

Equation (B.18) means that  $\theta'(\tau) > 0$  for  $0 \leq \tau \leq 1$  or  $\theta(\tau)$  is a continuous and strictly monotonic function in that range of 0 to  $\tau$ . We define the Kullback-Leibler divergence  $J(0, \tau)$  between  $p_\tau(\mathbf{g})$  and  $p_0(\mathbf{g})$  as

$$\begin{aligned} J(0, \tau) &= \int (p_\tau(\mathbf{g}) - p_0(\mathbf{g})) \ln \frac{p_\tau(\mathbf{g})}{p_0(\mathbf{g})} d\mathbf{g} \\ &= (\theta(\tau) - \theta(0)) \tau. \end{aligned} \quad (\text{B.19})$$

At  $\tau = 1$ ,  $J(0, 1) = J$ , the divergence defined in (3.27).

From (B.19),  $J(0, \tau)$  is also considered as a function of  $\theta$ . Denoting  $J(0, \tau) = m(\theta)$ , we apply a second-order Taylor series expansion of  $m(\theta)$  at  $\theta(0)$  to obtain

$$m(\theta) = m(\theta(0)) + (\theta(\tau) - \theta(0)) m'(\theta(0)) + \frac{1}{2} (\theta(\tau) - \theta(0))^2 m''(\theta(\xi)), \quad (\text{B.20})$$

where  $\xi$  is some value between 0 and  $\tau$ . The last term of (B.20) is obtained by combining with the property of  $\theta(\tau)$  which is continuous and strictly monotonic in the range of  $[0, \tau]$ .

Derivatives of  $m(\theta)$  are given by

$$\begin{aligned} m'(\theta) &= \tau(\theta) + (\theta(\tau) - \theta(0))\tau'(\theta) , \\ m''(\theta) &= 2\tau'(\theta) + (\theta(\tau) - \theta(0))\tau''(\theta) . \end{aligned} \tag{B.21}$$

With  $\theta'(\tau)\tau'(\theta) = 1$ , we take the derivative of both sides to have  $\theta''(\tau)\tau'(\theta) + \theta'(\tau)\tau''(\theta) = 0$ . Since  $\theta'(\tau) = \sigma_0^2$  equals a constant,  $\theta''(\tau) = 0$  which leads to  $\tau''(\theta) = 0$  and the second equation of (B.21) becomes

$$m''(\theta(\tau)) = 2/\theta'(\tau) = 2/\sigma_0^2 . \tag{B.22}$$

Evaluating other derivatives of  $m(\theta(\tau))$  at  $\tau = 0$ , we have

$$\begin{aligned} m(\theta(0)) &= 0 , \\ m'(\theta(0)) &= \tau(\theta) = 0 . \end{aligned} \tag{B.23}$$

Thus  $m(\theta)$  or  $J(0, \tau)$  in (B.19) is simplified to

$$J(0, \tau) = [\theta(\tau) - \theta(0)]^2 / \sigma_0^2 . \tag{B.24}$$

At  $\tau = 1$ , we have

$$J(0, 1) = [\theta(1) - \theta(0)]^2 / \sigma_0^2 . \tag{B.25}$$

With  $J = J(0, 1)$ ,  $\sigma_0^2 = \sigma_1^2$ , and  $\theta(\tau) = \bar{\lambda}_\tau$ , we have derived (3.30).

# APPENDIX C

## WIENER FILTER FOR LINEAR SHIFT VARIANCE PULSE-ECHO IMPULSE RESPONSE

This appendix provides an expansion of the shift-invariant methodology to include depth-varying impulse responses for the Wiener filter. In our simulation, RF data is generated by a linear convolution of the scattering object and the impulse response at the focal region. This linear shift-invariant model is valid only for the isoplanatic region where the system impulse response is unchanged. In the ultrasonic system, the impulse response is changed very little along the lateral direction, but rapidly in the axial direction because of diffraction and ultrasound attenuation. Thus, we need a more realistic model for the RF data and a corresponding Wiener filter.

In [41], Zemp et al. found that the isoplanatic region can be made for a small patch (in the axial direction), where the size of the patch is 2 mm for dynamic focused and 1 mm for fixed focused at the receiver. Therefore, we proposed a new model for the RF data, in which it is still a linear transformation of the scattering object but the impulse response is applied locally and updated for each isoplanatic patch. The equation for RF data  $\mathbf{g}$  is given as

$$\mathbf{g} = \sum_{j=1}^k \mathbf{H}_j \mathbf{f}_j + \mathbf{n} = \mathbf{H} \mathbf{f} + \mathbf{n}, \quad (\text{C.1})$$

where  $k$  is the number of the divided patches and  $\mathbf{H}_j$  is the block Toeplitz matrix constructed from the impulse response  $h_j$  for the  $j^{\text{th}}$  patch.  $\mathbf{f}_j = \mathbf{E}_j \mathbf{f}$ , where  $\mathbf{f}$  is a column vector of scattering objects, and  $\mathbf{E}_j$  is a diagonal matrix with the elements of the diagonal of 1's in the region corresponding to patch  $j$ , and 0's for elsewhere. Then we obtain the equation for  $\mathbf{E}_j$ , given as

$$\sum_{j=1}^k \mathbf{E}_j = \mathbf{I}, \quad (\text{C.2})$$

where  $\mathbf{I}$  is an identity matrix of dimension  $n$ , and  $\mathbf{H} = \sum_{j=1}^k \mathbf{H}_j \mathbf{E}_j$ . Note that  $\mathbf{H}_j$  is a block Toeplitz matrix for all  $j$  from 1 to  $k$ , but  $\mathbf{H}$  is not.

The covariance matrices for the RF data  $\mathbf{g}$  now become

$$\boldsymbol{\Sigma}_i = \sigma_{\text{obj}}^2 \sum_{j=1}^k \mathbf{H}_j \mathbf{E}_j (\mathbf{I} + \mathbf{S}_i) \mathbf{E}_j^t \mathbf{H}_j^t \quad i = 0, 1 \quad (\text{C.3})$$

and the decision variable is still given by (2.6).

Separating the covariance matrices into stationary and nonstationary terms as in (3.3), we obtain the equations for  $\boldsymbol{\Sigma}_s$  and  $\Delta\boldsymbol{\Sigma}_i$  given as

$$\begin{aligned} \boldsymbol{\Sigma}_s &= \sigma_{\text{obj}}^2 \sum_{j=1}^k \mathbf{H}_j \mathbf{E}_j \mathbf{E}_j^t \mathbf{H}_j^t + \sigma_n^2 \mathbf{I} \\ \Delta\boldsymbol{\Sigma}_i &= \sigma_{\text{obj}}^2 \sum_{j=1}^k \mathbf{H}_j \mathbf{E}_j \mathbf{S}_i \mathbf{E}_j^t \mathbf{H}_j^t. \end{aligned} \quad (\text{C.4})$$

Using the power series expansion of covariance matrix and truncating at the first order, we obtain the linear approximation of the decision variable

$$\lambda(\mathbf{g}) \cong \frac{1}{2} \mathbf{g}^t \boldsymbol{\Sigma}_s^{-1} (\Delta\boldsymbol{\Sigma}_1 - \Delta\boldsymbol{\Sigma}_0) \boldsymbol{\Sigma}_s^{-1} \mathbf{g}, \quad (\text{C.5})$$

where

$$\Delta\boldsymbol{\Sigma}_1 - \Delta\boldsymbol{\Sigma}_0 = \sigma_{\text{obj}}^2 \sum_{j=1}^k \mathbf{H}_j \mathbf{E}_j (\mathbf{S}_1 - \mathbf{S}_0) \mathbf{E}_j^t \mathbf{H}_j^t. \quad (\text{C.6})$$

Noting that for  $j \neq l$ ,  $\mathbf{E}_j (\mathbf{S}_1 - \mathbf{S}_0) \mathbf{E}_l^t = 0$ ,  $\Delta\boldsymbol{\Sigma}_1 - \Delta\boldsymbol{\Sigma}_0$  can be written as

$$\begin{aligned} \Delta\boldsymbol{\Sigma}_1 - \Delta\boldsymbol{\Sigma}_0 &= \sigma_{\text{obj}}^2 \left( \sum_{j=1}^k \mathbf{H}_j \mathbf{E}_j \right) (\mathbf{S}_1 - \mathbf{S}_0) \left( \sum_{j=1}^k \mathbf{E}_j^t \mathbf{H}_j^t \right) \\ &= \sigma_{\text{obj}}^2 \mathbf{H} (\mathbf{S}_1 - \mathbf{S}_0) \mathbf{H}^t. \end{aligned} \quad (\text{C.7})$$

By replacing (C.7) into (C.5), we obtain the first-order approximation of the test statistic given as

$$\lambda(\mathbf{g}) \approx \frac{1}{2} \mathbf{g}^t \boldsymbol{\Sigma}_s^{-1} \mathbf{H} \Delta\mathbf{S} \mathbf{H}^t \boldsymbol{\Sigma}_s^{-1} \mathbf{g}. \quad (\text{C.8})$$

Thus, the stationary Wiener filter has a form of  $\mathbf{H}^t \boldsymbol{\Sigma}_s^{-1} \mathbf{g}$ , where

$$\mathbf{H} = \sum_{j=1}^k \mathbf{H}_j \mathbf{E}_j \quad (\text{C.9})$$

and

$$\boldsymbol{\Sigma}_s = \sigma_{\text{obj}}^2 \sum_{j=1}^k \mathbf{H}_j \mathbf{E}_j \mathbf{E}_j^t \mathbf{H}_j^t + \sigma_n^2 \mathbf{I}. \quad (\text{C.10})$$

We note that for  $j \neq l$ ,  $\mathbf{E}_j \mathbf{E}_l^t = 0$ , combining with (C.9),  $\boldsymbol{\Sigma}_s$  can be written as

$$\boldsymbol{\Sigma}_s = \sigma_{\text{obj}}^2 \mathbf{H} \mathbf{H}^t + \sigma_n^2 \mathbf{I}. \quad (\text{C.11})$$

Thus the Wiener filter still has the same form as the Wiener filter we derived in [26], except that the system matrix  $\mathbf{H}$  now is a partial sum of block-Toplitz matrices and  $\boldsymbol{\Sigma}_s$  is not a covariance of a stationary process. To calculate the Wiener filtered RF data, a gradient conjugate method will be needed.

# APPENDIX D

## SUPPORTING MATERIAL FOR CHAPTER 5

### D.1 Ideal observer analysis for ill-conditioned $\mathbf{K}_n$

We begin with (5.9) where the poor condition of  $\mathbf{K}_n$  prevents the Woodbury matrix inverse identity from being applied. To avoid the poor condition, we modify  $\mathbf{K}_n$  to  $\mathbf{K}_{n,\varepsilon} \triangleq \sigma_{\text{obj}}^2 \mathbf{H}_T^t \Sigma_n^{-1} \mathbf{H}_T + \varepsilon \mathbf{I}$ , where  $\varepsilon > 0$ .

The test statistic in (5.9) is also modified to

$$\lambda_\varepsilon(\mathbf{g}_T) = \frac{\sigma_{\text{obj}}^2}{2} \mathbf{g}_T^t \Sigma_n^{-1} \mathbf{H}_T (\Psi_{1,\varepsilon}^{-1} - \Psi_{0,\varepsilon}^{-1}) \mathbf{H}_T^t \Sigma_n^{-1} \mathbf{g}_T, \quad (\text{D.1})$$

where  $\Psi_{i,\varepsilon} = (\mathbf{I} + \mathbf{S}_i)^{-1} + \mathbf{K}_{n,\varepsilon}$ ,  $i = 0,1$ , and  $\lambda(\mathbf{g}) = \lim_{\varepsilon \rightarrow 0^+} \lambda_\varepsilon(\mathbf{g})$ .

Because  $\varepsilon > 0$ ,  $\mathbf{K}_{n,\varepsilon}$  is guaranteed to be invertible, we can apply the Woodbury matrix inverse identity to  $\Psi_{i,\varepsilon}^{-1}$  to obtain

$$\Psi_{i,\varepsilon}^{-1} = \mathbf{K}_{n,\varepsilon}^{-1} - \mathbf{K}_{n,\varepsilon}^{-1} (\mathbf{K}_{n,\varepsilon}^{-1} + \mathbf{I} + \mathbf{S}_i)^{-1} \mathbf{K}_{n,\varepsilon}^{-1}. \quad (\text{D.2})$$

Replacing into (D.1), we obtain

$$\lambda_\varepsilon(\mathbf{g}_T) = \frac{\sigma_{\text{obj}}^2}{2} \mathbf{g}_T^t \mathbf{H}_T \Sigma_n^{-1} \mathbf{K}_{n,\varepsilon}^{-1} (\Phi_{0,\varepsilon}^{-1} - \Phi_{1,\varepsilon}^{-1}) \mathbf{K}_{n,\varepsilon}^{-1} \mathbf{H}_T^t \Sigma_n^{-1} \mathbf{g}_T, \quad (\text{D.3})$$

where  $\Phi_{i,\varepsilon} = \mathbf{K}_{n,\varepsilon}^{-1} + \mathbf{I} + \mathbf{S}_i$ ,  $i = 0,1$ .

By adopting the first-order approximation of  $(\mathbf{I} + \mathbf{A})^{-1} \simeq \mathbf{I} - \mathbf{A}$  to calculate  $\Phi_{i,\varepsilon}^{-1}$ ,  $\lambda_\varepsilon(\mathbf{g}_T)$  can be explored further. In the first approximation, we choose  $\mathbf{A} \triangleq \mathbf{K}_{n,\varepsilon}^{-1} + \mathbf{S}_i$  which leads to

$$\Phi_{i,\varepsilon}^{-1} \simeq \mathbf{I} - (\mathbf{K}_{n,\varepsilon}^{-1} + \mathbf{S}_i), \quad (\text{D.4})$$

and

$$\begin{aligned}
\lambda_\varepsilon(\mathbf{g}_T) &\simeq \frac{\sigma_{\text{obj}}^{-2}}{2} \mathbf{g}_T^t \mathbf{H}_T \boldsymbol{\Sigma}_n^{-1} \mathbf{K}_{n,\varepsilon}^{-1} (\mathbf{S}_1 - \mathbf{S}_0) \mathbf{K}_{n,\varepsilon}^{-1} \mathbf{H}_T^t \boldsymbol{\Sigma}_n^{-1} \mathbf{g}_T \\
&= \frac{\sigma_{\text{obj}}^{-4}}{2} \mathbf{g}_T^t \mathbf{H}_T \boldsymbol{\Sigma}_n^{-1} (\sigma_{\text{obj}}^2 \mathbf{H}_T^t \mathbf{H}_T + \varepsilon \sigma_n^2 \mathbf{I}) \Delta \mathbf{S} (\sigma_{\text{obj}}^2 \mathbf{H}_T^t \mathbf{H}_T + \varepsilon \sigma_n^2 \mathbf{I})^{-1} \mathbf{H}_T^t \boldsymbol{\Sigma}_n^{-1} \mathbf{g}_T \\
&= \frac{\sigma_{\text{obj}}^{-4}}{2} \mathbf{g}_T^t \mathbf{B}_{MV,\varepsilon} \Delta \mathbf{S} \mathbf{B}_{MV,\varepsilon}^t \mathbf{g}_T .
\end{aligned} \tag{D.5}$$

in which  $\mathbf{B}_{MV,\varepsilon}^t = (\sigma_{\text{obj}}^2 \mathbf{H}_T^t \mathbf{H}_T + \varepsilon \sigma_n^2 \mathbf{I})^{-1} \mathbf{H}_T^t$ .

Provided that the first-order approximation in (D.4) holds for all  $\varepsilon > 0$ ,  $\lambda_\varepsilon(\mathbf{g}_T)$  is factorized into  $\mathbf{B}_{MV,\varepsilon}^t \mathbf{g}_T$  squared and the task information  $\Delta \mathbf{S}$ . Letting  $\varepsilon \rightarrow 0^+$  we can get back to  $\lambda(\mathbf{g})$  from  $\lambda_\varepsilon(\mathbf{g}_T)$  meanwhile  $\lim_{\varepsilon \rightarrow 0^+} (\sigma_{\text{obj}}^2 \mathbf{H}_T^t \mathbf{H}_T + \varepsilon \sigma_n^2 \mathbf{I})^{-1} \mathbf{H}_T^t = \sigma_{\text{obj}}^{-2} \mathbf{H}_T^+$  since it is the limitation representation of the pseudoinverse (ref. [8], page 40). Thus, the first-order approximation leads us to the pseudoinverse of the system matrix.

In the second exploration, we use a different separation to obtain a better first-order approximation for  $\varepsilon > 0$ , given by  $\boldsymbol{\Phi}_{i,\varepsilon} = (\mathbf{K}_{n,\varepsilon}^{-1} + \mathbf{I}) + \mathbf{S}_i$ , to obtain

$$\boldsymbol{\Phi}_{i,\varepsilon}^{-1} \approx (\mathbf{K}_{n,\varepsilon}^{-1} + \mathbf{I})^{-1} - (\mathbf{K}_{n,\varepsilon}^{-1} + \mathbf{I})^{-1} \mathbf{S}_i (\mathbf{K}_{n,\varepsilon}^{-1} + \mathbf{I})^{-1} , \tag{D.6}$$

and

$$\lambda_\varepsilon(\mathbf{g}_T) \approx \frac{\sigma_{\text{obj}}^2}{2} \mathbf{g}_T^t \mathbf{H}_T (\sigma_n^2 \mathbf{K}_{n,\varepsilon} + \sigma_n^2 \mathbf{I})^{-1} (\mathbf{S}_1 - \mathbf{S}_0) (\sigma_n^2 \mathbf{K}_{n,\varepsilon} + \sigma_n^2 \mathbf{I})^{-1} \mathbf{H}_T^t \mathbf{g}_T , \tag{D.7}$$

which results in a WF beamformer given by  $\mathbf{B}_{WF,\varepsilon}^t = (\sigma_{\text{obj}}^2 \mathbf{H}_T^t \mathbf{H}_T + \sigma_n^2 \mathbf{I} + \varepsilon \sigma_n^2 \mathbf{I})^{-1} \mathbf{H}_T^t$ .

For  $\varepsilon \rightarrow 0^+$ , we have  $\lim_{\varepsilon \rightarrow 0^+} \mathbf{B}_{WF,\varepsilon} = \mathbf{B}_{WF}$  or WF beamformer remains in the same form. Thus, WF beamformer is robust and tolerant toward the ill-conditioned  $\mathbf{K}_n$ , while the MV beamformer is reduced to the pseudoinverse of the system matrix.

## D.2 Minimum variance distortionless response (MVDR)

The MVDR problem in (5.18) can be solved by using the method of Lagrange multipliers. We form a cost function involving undetermined Lagrange matrix  $\boldsymbol{\Lambda}$ , given by

$$J(\mathbf{B}) = \text{Tr} [\mathbf{B}^t \boldsymbol{\Sigma}_n \mathbf{B} + \boldsymbol{\Lambda}^t (\mathbf{H}^t \mathbf{B} - \mathbf{I})] . \tag{D.8}$$

Taking the gradient of (D.8) with respect to  $\mathbf{B}$

$$\frac{\partial J(\mathbf{B})}{\partial \mathbf{B}} = \Sigma_n \mathbf{B} + \mathbf{H} \boldsymbol{\Lambda} . \quad (\text{D.9})$$

Setting the sum of (D.9) equal to 0, we obtain  $\mathbf{B}_{opt} = -\Sigma_n^{-1} \mathbf{H} \boldsymbol{\Lambda}$ . Hence,

$$\mathbf{H}^t \mathbf{B} = \mathbf{I} = -\mathbf{H}^t \Sigma_n^{-1} \mathbf{H} \boldsymbol{\Lambda} . \quad (\text{D.10})$$

Thus, we obtain

$$\boldsymbol{\Lambda} = -(\mathbf{H}^t \Sigma_n^{-1} \mathbf{H})^{-1} , \quad (\text{D.11})$$

and

$$\mathbf{B}_{opt} = \Sigma_n^{-1} \mathbf{H} (\mathbf{H}^t \Sigma_n^{-1} \mathbf{H})^{-1} . \quad (\text{D.12})$$

The beamformer has a form in (D.12) is known as minimum variance distortionless response or linear constraint minimum variance (LCMV) in some literature about beamforming [68].

### D.3 Proof of (5.23)

Starting from (5.8), we have

$$\begin{aligned} \Sigma_{T,i}^{-1} \mathbf{H}_T &= \Sigma_n^{-1} \mathbf{H}_T - \Sigma_n^{-1} \mathbf{H}_T ((\mathbf{I} + \mathbf{S}_i)^{-1} + \sigma_{obj}^2 \mathbf{H}_T^t \Sigma_n^{-1} \mathbf{H}_T)^{-1} \sigma_{obj}^2 \mathbf{H}_T^t \Sigma_n^{-1} \mathbf{H}_T \\ &= \Sigma_n^{-1} \mathbf{H}_T ((\mathbf{I} + \mathbf{S}_i)^{-1} + \sigma_{obj}^2 \mathbf{H}_T^t \Sigma_n^{-1} \mathbf{H}_T)^{-1} (\mathbf{I} + \mathbf{S}_i)^{-1} , \end{aligned} \quad (\text{D.13})$$

and

$$\mathbf{H}_T^t \Sigma_{T,i}^{-1} \mathbf{H}_T = \mathbf{H}_T^t \Sigma_n^{-1} \mathbf{H}_T ((\mathbf{I} + \mathbf{S}_i)^{-1} + \sigma_{obj}^2 \mathbf{H}_T^t \Sigma_n^{-1} \mathbf{H}_T)^{-1} (\mathbf{I} + \mathbf{S}_i)^{-1} , \quad (\text{D.14})$$

for  $i = 0, 1$ . Combining (D.13) and (D.14), we obtain

$$\Sigma_{T,i}^{-1} \mathbf{H}_T (\mathbf{H}_T^t \Sigma_{T,i}^{-1} \mathbf{H}_T)^{-1} = \Sigma_n^{-1} \mathbf{H}_T (\mathbf{H}_T^t \Sigma_n^{-1} \mathbf{H}_T)^{-1} , \quad (\text{D.15})$$

which proves (5.23)

# APPENDIX E

## RECONSTRUCTION USING THE SVD METHOD

With  $\mathcal{R}$  given in (6.6), applying the adjoint operator  $\mathcal{R}^\dagger$  to backproject  $g$  onto the object space, we obtain

$$[\mathcal{R}^\dagger g](\mathbf{r}) = \int_0^\pi d\varphi \int_{-a}^a dp g(p, \varphi) \delta(p \cos \varphi - \mathbf{r} \cdot \mathbf{n}(\varphi)) . \quad (\text{E.1})$$

At each  $\varphi$ ,  $\mathcal{R}^\dagger$  backprojects the 1-D data function  $g(p, \varphi)$  back into 2-D object space by substituting  $p \cos \varphi \rightarrow \mathbf{r} \cdot \mathbf{n}(\varphi)$ . Combining with (6.6), we have

$$[\mathcal{R}^\dagger \mathcal{R} h](\mathbf{r}) = \int_0^\pi d\varphi \int_{-a}^a dp \delta(p \cos \varphi - \mathbf{r} \cdot \mathbf{n}(\varphi)) \int d\mathbf{r}' h(\mathbf{r}') \delta(p \cos \varphi - \mathbf{r}' \cdot \mathbf{n}(\varphi)) . \quad (\text{E.2})$$

By choosing the Fourier kernel  $u_\rho(\mathbf{r}) = e^{j2\pi\boldsymbol{\rho}\cdot\mathbf{r}}$  as the eigenfunction for the object space, we obtain

$$\begin{aligned} [\mathcal{R}^\dagger \mathcal{R} u_\rho](\mathbf{r}) &= \int_0^\pi d\varphi \int_{-a}^a dp \delta(p \cos \varphi - \mathbf{r} \cdot \mathbf{n}(\varphi)) \int d\mathbf{r}' u(\mathbf{r}') \delta(p \cos \varphi - \mathbf{r}' \cdot \mathbf{n}(\varphi)) \\ &= \int_0^\pi d\varphi \int_{-a}^a dp \delta(p \cos \varphi - \mathbf{r} \cdot \mathbf{n}(\varphi)) \int d\mathbf{r}' e^{j2\pi\boldsymbol{\rho}\cdot\mathbf{r}'} \delta(p \cos \varphi - \mathbf{r}' \cdot \mathbf{n}(\varphi)) . \end{aligned} \quad (\text{E.3})$$

Using the definition of the delta function,

$$\begin{aligned} \int d\mathbf{r}' e^{j2\pi\boldsymbol{\rho}\cdot\mathbf{r}'} \delta(p \cos \varphi - \mathbf{r}' \cdot \mathbf{n}(\varphi)) &= \int d\mathbf{r}' e^{j2\pi\boldsymbol{\rho}\cdot\mathbf{r}'} \int dt e^{j2\pi t(p \cos \varphi - \mathbf{r}' \cdot \mathbf{n}(\varphi))} \\ &= \int dt e^{j2\pi t p \cos \varphi} \delta(\boldsymbol{\rho} - t\mathbf{n}(\varphi)) . \end{aligned} \quad (\text{E.4})$$

The argument  $\boldsymbol{\rho} - t\mathbf{n}(\varphi)$  is two-dimensional. We project the delta function onto two orthogonal axes  $(\mathbf{n}(\varphi), \mathbf{n}^\perp(\varphi))$  as in the expression  $\delta(\mathbf{r}) = \delta(x)\delta(y)$ , and we find the

product of two delta functions,

$$\begin{aligned}\delta(\boldsymbol{\rho} - t\mathbf{n}(\varphi)) &= \delta[(\boldsymbol{\rho} - t\mathbf{n}(\varphi)) \cdot \mathbf{n}(\varphi)]\delta[(\boldsymbol{\rho} - t\mathbf{n}(\varphi)) \cdot \mathbf{n}^\perp(\varphi)] \\ &= \delta(\rho \cos(\xi - \varphi) - t) \delta(\rho \sin(\xi - \varphi)),\end{aligned}\quad (\text{E.5})$$

where  $\boldsymbol{\rho} = (\rho, \xi)$  is the polar coordinate in the Fourier domain. Substituting (E.5) into (E.4), we find

$$\int d\mathbf{r}' e^{j2\pi\boldsymbol{\rho}\cdot\mathbf{r}'} \delta(p\cos\varphi - \mathbf{r} \cdot \mathbf{n}(\varphi)) = \frac{1}{|\rho|} e^{j2\pi\rho p\cos\varphi} \delta(\xi - \varphi). \quad (\text{E.6})$$

The last equation comes from the relation [8]

$$\delta(y(x)) = \sum_{n=1}^N \frac{\delta(x - x_n)}{|y'(x_n)|}, \quad (\text{E.7})$$

simply applied to  $\delta(\rho \sin(\xi - \varphi))$ .

Replacing (E.6) into (E.3), we obtain

$$\begin{aligned}[\mathcal{R}^\dagger \mathcal{R} u_\rho](\mathbf{r}) &= \int_0^\pi d\varphi \int_{-a}^a dp \delta(p \cos \varphi - \mathbf{r} \cdot \mathbf{n}(\varphi)) \int d\mathbf{r}' u(\mathbf{r}') \delta(p \cos \varphi - \mathbf{r}' \cdot \mathbf{n}(\varphi)) \\ &= \frac{1}{|\rho|} \int_0^\pi d\varphi \int_{-a}^a dp \delta(p \cos \varphi - \mathbf{r} \cdot \mathbf{n}(\varphi)) e^{j2\pi\rho p\cos\varphi} \delta(\xi - \varphi) \\ &= \frac{1}{|\rho|} \int_{-a}^a dp \delta(p \cos \xi - \mathbf{r} \cdot \mathbf{n}(\xi)) e^{j2\pi\rho p\cos\xi} \\ &= \begin{cases} \frac{e^{j2\pi\boldsymbol{\rho}\cdot\mathbf{r}}}{|\rho\cos\xi|} = \frac{u_\rho(\mathbf{r})}{|\rho\cos\xi|} & \text{if } -a \cos\xi \leq \mathbf{r} \cdot \mathbf{n}(\xi) \leq a \cos\xi \\ 0 & \text{otherwise.} \end{cases}\end{aligned}\quad (\text{E.8})$$

Thus the eigenvalue for  $\mathcal{R}^\dagger \mathcal{R}$  corresponding to  $u_\rho$  is given by

$$\mu_\rho = \begin{cases} \frac{1}{|\rho\cos\xi|} & \text{if } -a \cos\xi \leq \mathbf{r} \cdot \mathbf{n}(\xi) \leq a \cos\xi \\ 0 & \text{otherwise.} \end{cases}\quad (\text{E.9})$$

The corresponding eigenvalue  $\kappa_\rho$  of the pseudoinverse  $(\mathcal{R}^\dagger \mathcal{R})^+$  is given by

$$\kappa_\rho = \begin{cases} |\rho\cos\xi| & \text{if } -a \cos\xi \leq \mathbf{r} \cdot \mathbf{n}(\xi) \leq a \cos\xi \\ 0 & \text{otherwise.} \end{cases}\quad (\text{E.10})$$

The eigenfunction of the image space is defined as  $v_\rho(\mathbf{s}) = \sqrt{\kappa_\rho} \mathcal{R} u_\rho(\mathbf{r})$ , which is calcu-

lated as follows.

$$\begin{aligned}
v_{\boldsymbol{\rho}}(\mathbf{s}) &= \sqrt{\kappa_{\boldsymbol{\rho}}} \int d\mathbf{r} e^{j2\pi\boldsymbol{\rho}\cdot\mathbf{r}} \delta(p\cos\varphi - \mathbf{r}\cdot\mathbf{n}(\varphi)) \\
&= \sqrt{\kappa_{\boldsymbol{\rho}}} \int d\mathbf{r} e^{j2\pi\boldsymbol{\rho}\cdot\mathbf{r}} \int dt e^{j2\pi t(p\cos\varphi - \mathbf{r}\cdot\mathbf{n}(\varphi))} \\
&= \sqrt{\kappa_{\boldsymbol{\rho}}} \int dt e^{j2\pi t p \cos\varphi} \delta(\boldsymbol{\rho} - t\mathbf{n}(\varphi)) .
\end{aligned} \tag{E.11}$$

Applying (E.5) to (E.11), we find

$$v_{\boldsymbol{\rho}}(\mathbf{s}) = v_{\boldsymbol{\rho}}(p, \varphi) = \frac{\sqrt{\kappa_{\boldsymbol{\rho}}}}{|\rho|} e^{j2\pi p \cos\varphi} \delta(\xi - \varphi) . \tag{E.12}$$

Consequently, the pseudoinverse operator  $\mathcal{R}^+$  is

$$[\mathcal{R}^+](\mathbf{r}) = \int d\boldsymbol{\rho} \sqrt{\kappa_{\boldsymbol{\rho}}} u_{\boldsymbol{\rho}}(\mathbf{r}) v_{\boldsymbol{\rho}}^\dagger(\mathbf{s}) = \int d\boldsymbol{\rho} \frac{\kappa_{\boldsymbol{\rho}}}{|\rho|} e^{j2\pi\boldsymbol{\rho}\cdot\mathbf{r}} e^{-j2\pi p \cos\varphi} \delta(\xi - \varphi), \tag{E.13}$$

and therefore

$$\begin{aligned}
\hat{h}(\mathbf{r}) &= [\mathcal{R}^+ g](\mathbf{r}) \\
&= \int_0^\pi d\varphi \int_{-a}^a dp \int d\boldsymbol{\rho} |\cos\xi| e^{j2\pi\boldsymbol{\rho}\cdot\mathbf{r}} e^{-j2\pi p \cos\varphi} \delta(\xi - \varphi) g(p, \varphi) \\
&= \int_0^\pi d\varphi \int d\rho |\rho| e^{j2\pi\rho\mathbf{r}\cdot\mathbf{n}(\varphi)} |\cos\varphi| \int_{-a}^a dp e^{-j2\pi p \cos\varphi} g(p, \varphi) ,
\end{aligned} \tag{E.14}$$

if  $-a \cos\varphi \leq \mathbf{r}\cdot\mathbf{n}(\varphi) \leq a \cos\varphi$ . If this condition is not satisfied,  $\kappa_{\boldsymbol{\rho}} = 0$  which leads to  $\hat{h}(\mathbf{r}) = 0$ .

# APPENDIX F

## PEER-REVIEWED PUBLICATIONS AND CONTRIBUTED TALKS

Appendix F include a book chapter, journal papers, conference proceedings papers, and presentations on topics related to the dissertation work. These are listed below.

### F.1 Book chapter

1. **Nghia Q. Nguyen**, Craig K. Abbey, and Michael F. Insana, “Task-based design and evaluation of ultrasonic imaging systems” in *Ultrasonic Imaging and Therapy*, A. Fenster, and J. Lacefield, Eds. American Association of Physicists in Medicine, New York, NY: Routledge, 2012 (in press, invited).

### F.2 Journal papers

1. **Nghia Q. Nguyen**, Craig K. Abbey, and Michael F. Insana, “Objective assessment of sonographic quality. I. Task information,” submitted to *IEEE Transactions on Medical Imaging*,, 2012 (under review)
2. **Nghia Q. Nguyen**, Craig K. Abbey, and Michael F. Insana, “Objective assessment of sonographic quality. II. Acquisition information spectrum,” submitted to *IEEE Transactions on Medical Imaging*, 2012 (under review)
3. Craig K. Abbey, **Nghia Q. Nguyen**, and Michael F. Insana, “Effects of frequency and bandwidth on diagnostic information transfer in ultrasonic B-Mode imaging,” accepted to *IEEE Transactions on Ultrasonics, Ferroelectrics, and Frequency Control*, 2012.
4. **Nghia Q. Nguyen**, Craig K. Abbey, and Michael F. Insana, “An adaptive filter to approximate the Bayesian strategy for sonographic beamforming,” *IEEE Transactions on Medical Imaging*, vol. 30, no. 1, pp. 28-37, 2011.

5. Craig K. Abbey, **Nghia Q. Nguyen**, and Michael F. Insana, “Optimal beamforming in ultrasound using the ideal observer,” *IEEE Transactions on Ultrasonics, Ferroelectrics, and Frequency Control*, vol. 57, no. 8, pp. 1782-1796, 2010.

### F.3 Conference proceedings

1. **Nghia Q. Nguyen**, Craig K. Abbey, and Michael F. Insana, “Acquisition information spectrum for evaluating sonographic quality,” submitted to *International Conference of the IEEE Engineering in Medicine and Biology Society*, San Diego, CA, August 2012.
2. Craig K. Abbey, **Nghia Q. Nguyen**, William D. O’Brien Jr., and Michael F. Insana, “An ideal observer approach to mechanical limits in B-Mode ultrasound imaging,” submitted to *International Conference of the IEEE Engineering in Medicine and Biology Society*, San Diego, CA, August 2012.
3. Craig K. Abbey, **Nghia Q. Nguyen**, and Michael F. Insana, “Frequency, bandwidth, and information transfer in B-Mode imaging,” in *Proceedings SPIE Medical Imaging: Ultrasonic Imaging, Tomography, and Therapy*, pp 83200I.1-8, 2012.
4. **Nghia Q. Nguyen**, Craig K. Abbey, and Michael F. Insana, “Analysis of minimum-variance and Wiener-filtered beamforming strategies,” *Proceedings of the IEEE Ultrasonics Symposium*, 2011 (in press).
5. **Nghia Q. Nguyen**, Craig K. Abbey, and Michael F. Insana, “Detectability index describes the information conveyed by a sonographic image,” *Proceedings of the IEEE Ultrasonics Symposium*, 2011 (in press).
6. **Nghia Q. Nguyen**, Craig K. Abbey, and Michael F. Insana, “Robustness of beamforming in the Bayesian observer approach,” *Proceedings of the IEEE Ultrasonics Symposium*, pp. 995-998, 2010.
7. Craig K. Abbey, **Nghia Q. Nguyen**, and Michael F. Insana, “Cystic resolution and task performance in beamforming,” *Proceedings of the IEEE Ultrasonics Symposium*, pp. 1747-1750, 2010.
8. **Nghia Q. Nguyen**, Craig K. Abbey, Rebecca D. Yapp, and Michael F. Insana, “Tomographic reconstruction of the pulse-echo spatial temporal impulse response,”

in *Proceedings SPIE Medical Imaging: Ultrasonic Imaging and Signal Processing*, pp 7629-14.1-11, 2010.

9. **Nghia Q. Nguyen**, Craig K. Abbey, and Michael F. Insana, “Ultrasonic array beamforming with iterative spatial filters,” in *Proceedings SPIE Medical Imaging: Ultrasonic Imaging and Signal Processing*, pp 7265-0A.1-12, 2009.
10. Craig K. Abbey, **Nghia Q. Nguyen**, and Michael F. Insana, “An ideal observer approach to beamforming,” in *Proceedings SPIE Medical Imaging: Ultrasonic Imaging and Signal Processing*, pp 6920-06.1-8, 2008.

## F.4 Presentations

1. **Nghia Q. Nguyen**, Craig K. Abbey, and Michael F. Insana, “Analysis of minimum-variance and Wiener-filtered beamforming strategies,” presented at *IEEE International Ultrasonics Symposium*, Orlando, Florida, October, 2011.
2. **Nghia Q. Nguyen**, Craig K. Abbey, and Michael F. Insana, “Detectability index describes the information conveyed by a sonographic image,” presented at *IEEE International Ultrasonics Symposium*, Orlando, Florida, October, 2011.
3. **Nghia Q. Nguyen**, Craig K. Abbey, and Michael F. Insana, “Ultrasonic array beamformers that maximize diagnostic information,” presented at *Digital Signal Processing Seminar*, Department of Electrical and Computer Engineering, University of Illinois at Urbana-Champaign, December 1, 2010.
4. **Nghia Q. Nguyen**, Craig K. Abbey, and Michael F. Insana, “Ultrasonic array beamforming with iterative spatial filters,” presented at *SPIE Medical Imaging Conference*, Orlando, Florida, 2009.
5. **Nghia Q. Nguyen** and Michael F. Insana, “Information theoretic approaches to ultrasonic system design,” presented at *Bioacoustics Research Lab Seminar*, Department of Electrical and Computer Engineering, University of Illinois at Urbana-Champaign, December 2, 2008.
6. **Nghia Q. Nguyen**, Craig K. Abbey, and Michael F. Insana, “Information theoretic approaches to ultrasonic system design: Beamforming with iterative spatial filters,” presented at *156th Meeting of the Acoustical Society of America*, Miami, Florida, October, 2008.

## REFERENCES

- [1] American Cancer Society, *Cancer Facts & Figures 2010*. Atlanta, GA: American Cancer Society, 2010.
- [2] E.Y.K. Ng and N.M. Sudharsan, "Modeling of female breast tumor detection with dynamic/active approach: A thermal analysis," in *Emerging Technologies in Breast Imaging and Mammography*, J.S. Suri, R.M. Rangayyan, and S. Laxminarayan, Eds. Stevenson Ranch, CA: American Scientific Publishers, 2008, pp. 365-401.
- [3] S.A. Feig, "Estimation of currently attainable benefit from mammographic screening of women aged 40-49 years," *Cancer*, vol. 75, no. 10, pp. 2412-2419, 1995.
- [4] J.F. Greenleaf, A. Johnson, and R.C. Bahn, "Quantitative cross-sectional imaging of ultrasound parameters," *Ultrasonics Symposium*, pp. 989-995, 1977.
- [5] P.L. Carson, C.R. Meyer, A.L. Scherzinger, and T.V. Oughton, "Breast imaging in coronal planes with simultaneous pulse echo and transmission ultrasound," *Science*, vol. 214, no. 4525, pp. 1141-1143, 1981.
- [6] E.A. Sickles, "Breast imaging: From 1965 to the present," *Radiology*, vol. 215, no. 1, pp. 1-16, 2000.
- [7] L. Watson, "The role of ultrasound in breast imaging," *Radiologic Technology*, vol. 71, no. 5, pp. 441-459, 2000.
- [8] H.H. Barrett and K.J. Myers, *Foundations of Image Science*. Hoboken, NJ: John Wiley & Sons, 2004.
- [9] D.M. Green and J.A. Swets, *Signal Detection Theory and Psychophysics*. New York, NY: Wiley, 1966.
- [10] J.A. Swets, "ROC analysis applied to the evaluation of medical imaging techniques," *Investigative Radiology*, vol. 14, no. 2, pp. 109-120, 1979
- [11] J.A. Swets and R.M. Pickett, *Evaluation of Diagnostic Systems: Methods from Signal Detection Theory*. New York, NY: Academic Press, 1982.
- [12] R.F. Wagner and D.G. Brown, "Unified SNR analysis of medical imaging systems," *Physics in Medicine and Biology*, vol. 30, no. 6, pp. 489-518, 1985.

- [13] R.F. Wagner, "Low contrast sensitivity of radiologic, CT, nuclear medical, and ultrasound medical imaging systems," *IEEE Transactions on Medical Imaging*, vol. MI-2, no. 3, pp. 105-121, 1983.
- [14] H.H. Barrett, "Objective assessment of image quality: Effects of quantum noise and object variability," *Journal Optical Society of America A*, vol. 7, no. 7, pp. 1266-1278, 1990.
- [15] H.H. Barrett, C.K. Abbey, and E. Clarkson, "Objective assessment of image quality. III. ROC metrics, ideal observers, and likelihood-generating functions," *Journal of the Optical Society of America A*, vol. 15, no. 6, pp. 1520-1535, 1998.
- [16] R. Shaw, "Evaluating the efficiency of imaging processes," *Reports on Progress in Physics*, vol. 41, pp. 1104-1155, 1978.
- [17] H.H. Barrett, J.L. Denny, R.F. Wagner, and K.J. Myers, "Objective assessment of image quality. II. Fisher information, Fourier crosstalk, and figures of merit for task performance," *Journal of the Optical Society of America A*, vol. 12, no. 5, pp. 834-852, 1995.
- [18] K.J. Myers, L.S. Kyprianou, and S. Park, "Wagner's unified theory of image quality: Three decades later," in *Advances in Medical Physics*, A.B. Wolbarst, A. Karellas, E.A. Krupinski, and W.R. Hendee, Eds. Madison, WI: Medical Physics Publishing, 2010, pp. 143-157.
- [19] R.F. Wagner, S.W. Smith, J.M. Sandrik, and H. Lopez, "Statistics of speckle in ultrasound B-scans," *IEEE Transactions on Ultrasonics, Ferroelectrics, and Frequency Control*, vol. 30, no. 3, pp. 156-163, 1983.
- [20] S.W. Smith, R.F. Wagner, J.M. Sandrik, and H. Lopez, "Low contrast detectability and contrast/detail analysis in medical ultrasound," *IEEE Transactions on Sonics and Ultrasonics*, vol. 30, no. 3, pp. 164-173, 1983.
- [21] R.F. Wagner, M.F. Insana, and S.W. Smith, "Fundamental correlation lengths of coherent speckle in medical ultrasonic images," *IEEE Transactions on Ultrasonics, Ferroelectrics, and Frequency Control*, vol. 35, no. 1, pp. 34-44, 1988.
- [22] G.E. Trahey, J.W. Allison, S.W. Smith, and O.T. Von Ramm, "A quantitative approach to speckle reduction via frequency compounding," *Ultrasonic Imaging*, vol. 8, no. 3, pp. 151-164, 1986.
- [23] J.M. Thijssen, B.J. Oosterveld, and R.F. Wagner, "Gray level transforms and lesion detectability in echographic images," *Ultrasonic Imaging*, vol. 10, no. 3, pp. 171-195, 1988.
- [24] T.J. Hall, M.F. Insana, L.A. Harrison, N.M. Soller, and K.J. Schlehr, "Ultrasound contrast-detail analysis: a comparison of low-contrast detectability among scanhead designs," *Medical Physics*, vol. 22, no. 7, pp. 1117-1125, 1995.

- [25] S.S. Brunke, M.F. Insana, J.J. Dahl, C. Hansen, M. Ashfaq, and H. Ermert, "An ultrasound research interface for a clinical system," *IEEE Transactions on Ultrasonics, Ferroelectrics, and Frequency Control*, vol. 53, no. 10, pp. 198-210, 2007.
- [26] C.K. Abbey, R.J. Zemp, J. Liu, K.K Lindfors, and M.F. Insana, "Observer efficiency in discrimination tasks simulating malignant and benign breast lesions with ultrasound," *IEEE Transactions on Medical Imaging*, vol. 25, no. 2, pp. 198-209, 2006.
- [27] N.Q. Nguyen, C.K. Abbey, and M.F. Insana, "Detectability index describes the information conveyed by sonographic images," in *Proceedings of IEEE Ultrasonics Symposium*, Orlando, FL, 2011 (in press).
- [28] N.Q. Nguyen, C.K. Abbey, and M.F. Insana, "Acquisition information spectrum for evaluating sonographic quality," submitted to *IEEE Engineering in Medicine and Biology Society*, San Diego, CA, August, 2012.
- [29] N.Q. Nguyen, C.K. Abbey, and M.F. Insana, "Robustness of the Wiener filter in Bayesian observer approach," in *Proceedings of IEEE Ultrasonics Symposium*, San Diego, CA, October, pp. 995 - 998, 2010.
- [30] N.Q. Nguyen, C.K. Abbey, and M.F. Insana, "An adaptive filter to approximate the Bayesian strategy for sonographic beamforming," *IEEE Transactions on Medical Imaging*, vol. 30, no. 1, pp. 28-37, 2011
- [31] C.K. Abbey, N.Q. Nguyen, and M.F. Insana, "Optimal beamforming in ultrasound using the ideal observer," *IEEE Transactions on Ultrasonics, Ferroelectrics, and Frequency Control*, vol. 57, no. 8, pp. 1782-1796, 2010
- [32] N.Q. Nguyen, C.K. Abbey, and M.F. Insana, "Analysis of minimum-variance and Wiener-filtered beamforming strategies," in *Proceedings of IEEE Ultrasonics Symposium*, Orlando, FL, 2011 (in press).
- [33] N.Q. Nguyen, C.K. Abbey, R.D. Yapp, and M.F. Insana, "Tomographic reconstruction of the pulse-echo spatiotemporal impulse response" in *Proceedings of Society of Photo-Optical Instrumentation Engineers (SPIE)*, vol. 7629, pp. 76290F.1-11, 2010.
- [34] C.W. Patrick Jr., "Breast tissue engineering" *Annual Review of Biomedical Engineering*, vol. 6, pp. 109-130, 2004.
- [35] M. Insana and M. Oelze, "Advanced ultrasonic imaging techniques for breast cancer research," in *Emerging Technologies in Breast Imaging and Mammography*, J.S. Suri, R.M. Rangayyan, and S. Laxminarayan, Eds. Stevenson Ranch, CA: American Scientific Publishers, 2008, pp. 141-160.
- [36] T. Tot, "General morphology of benign and malignant breast lesions: Old parameters in new perspectives," in *Emerging Technologies in Breast Imaging and Mammography*, J.S. Suri, R.M. Rangayyan, and S. Laxminarayan, Eds. Stevenson Ranch, CA: American Scientific Publishers, 2008, pp. 1-23.

- [37] American College of Radiology, *Breast Imaging Reporting and Data System Atlas*. Reston, VA: American College of Radiology, 2003.
- [38] S. Field and F. Dunn, "Correlation of echographic visualizability of tissue with biological composition and physiological state," *Journal of the Acoustical Society of America A*, vol. 54, no. 3, pp. 809-812, 1973.
- [39] R.F. Wagner, M.F. Insana, and D.G. Brown, "Statistical properties of medical ultrasound with applications to medical imaging," *Journal Optical Society of America A*, vol. 4, no. 5, pp. 910-922, 1987.
- [40] M.F. Insana and D.G. Brown, "Acoustic scattering theory applied to soft biological tissues," in *Ultrasonic Scattering in Biological Tissues*, K.K. Shung and G.A. Thiemes, Eds. Boca Raton, FL: CRC Press, 1993.
- [41] R.J. Zemp, C.K. Abbey, and M.F. Insana, "Linear system model for ultrasonic imaging: Application to signal statistics," *IEEE Transactions on Ultrasonics, Ferroelectrics, and Frequency Control*, vol. 50, no. 6, pp. 642-654, 2003.
- [42] R.S.C. Cobbold, *Foundations of Biomedical Ultrasound*. New York, NY: Oxford University Press, 2006.
- [43] J.A. Jensen and N.B. Svendsen, "Calculation of pressure fields from arbitrarily shaped, apodized, and excited ultrasound transducers," *IEEE Transactions on Ultrasonics, Ferroelectrics, and Frequency Control*, vol. 39, no. 2, pp. 262-267, 1992.
- [44] J.A. Jensen, "Field: A program for simulating ultrasound systems," *Medical and Biological Engineering and Computing*, vol. 34, Supplement 1, Part 1, pp. 351-353, 1996.
- [45] G.H. Golub and C.F. Van Loan, *Matrix Computations*, 3rd ed. Baltimore, MD: The Johns Hopkins University Press, 1996.
- [46] H.V. Poor, *An Introduction to Signal Detection and Estimation*, 2nd ed. New York, NY: Springer-Verlag, 1994.
- [47] W.P. Tanner and T.G. Birdsall, "Definition of  $d'$  and  $\eta$  as psychophysical measures," in *Signal Detection and Recognition by Human Observer: Contemporary Readings*, J.A Swets, Ed. New York, NY: Wiley, 1964, pp. 147-163.
- [48] D. Middleton, *An Introduction to Statistical Communication Theory*. Los Altos, CA: Peninsula Publishing, 1987.
- [49] J.A. O'Sullivan, R.E. Blahut, and D.L. Snyder, "Information-theoretic image formation," *IEEE Transactions on Information Theory*, vol. 44, no. 6, pp. 2094-2122, 1998.
- [50] S. Kullback, *Information Theory and Statistics*. New York, NY: Dover, 1997.

- [51] C.E. Shannon, "A mathematical theory of communication," *Bell System Technical Journal*, vol. 27, pp. 379-423, 1948.
- [52] S. Kullback and R.A. Leibler, "On information and sufficiency," *The Annals of Mathematical Statistics*, vol. 22 no. 1, pp. 79-86, 1951.
- [53] K. Fukunaga, *Introduction to Statistical Pattern Recognition*, 2nd ed. New York, NY: Academic Press, 1990.
- [54] B.A.J. Angelsen, *Ultrasound Imaging Waves, Signals, and Signal Processing*. Trondheim, Norway: Emantec, 2000.
- [55] R.J. Zemp, M.D. Parry, C.K. Abbey, and M.F. Insana, "Detection performance theory for ultrasound imaging systems," *IEEE Transactions on Medical Imaging*, vol. 24, no. 3, pp. 300-310, 2005.
- [56] K. E. Thomenius, "Evolution of ultrasound beamformers," *Proceedings of the IEEE Ultrasonics Symposium.*, pp. 1615-1622, 1996.
- [57] Y. Wan and E.S. Ebbini, "A post-beamforming 2-D pseudoinverse filter for coarsely sampled ultrasound arrays," *IEEE Transactions on Ultrasonics, Ferroelectrics, and Frequency Control*, vol. 56, no. 9, pp. 1988-1902, 2009.
- [58] O. Michailovich and A. Tannenbaum, "Blind deconvolution of medical ultrasound images: A parametric inverse filtering approach," *IEEE Transactions on Image Processing*, vol. 16, no. 12, pp. 3005-3019, 2007.
- [59] T.C. Aysal and K.E. Barner, "Rayleigh maximum-likelihood filtering for speckle reduction of ultrasound images," *IEEE Transactions on Medical Imaging*, vol. 26, no. 5, pp. 712-727, 2007.
- [60] D. Boukerroui, O. Basset, N. Guerin, and A. Baskurt, "Multiresolution texture based adaptive clustering algorithm for breast lesion segmentation," *European Journal of Ultrasound*, vol. 8, no. 2, pp. 135-144, 1998.
- [61] G. Xiao, M. Brady, J.A. Noble, and Y. Zhang, "Segmentation of ultrasound B-mode images with intensity inhomogeneity correction," *IEEE Transactions on Medical Imaging*, vol. 21, no. 1, pp. 48-57, 2002.
- [62] T.N. Pappas, "An adaptive clustering algorithm for image segmentation," *IEEE Transactions on Signal Processing*, vol. 40, no. 4, pp. 901-914, 1992.
- [63] B.J. Besag, "On the statistical analysis of dirty pictures," *Journal of the Royal Statistical Society: Series B*, vol. 48, no. 3, pp. 259-302, 1986.
- [64] J.S. Geman and D. Geman, "Stochastic relaxation, Gibbs distribution and the Bayesian restoration of images," *IEEE Transactions on Pattern Analysis and Machine Intelligence*, vol. 6, no. 6, pp. 721-741, 1984.

- [65] E.A. Ashton and K.J. Parker, "Multiple resolution Bayesian segmentation of ultrasound images," *Ultrasonic Imaging*, vol. 17, no. 4, pp. 291-304, 1995.
- [66] M.F. Insana and T.J. Hall, "Visual detection efficiency in ultrasonic imaging: A framework for objective assessment of image quality," *Journal of the Acoustical Society of America A*, vol. 95, no. 4, pp. 2081-2090, 1994.
- [67] A. Burgess and H. Ghandeharian, "Visual signal detection. I. Ability to use phase information," *Journal of the Optical Society of America A*, vol. 1, no. 8, pp. 900-905, 1984.
- [68] H.L. Van Trees, *Detection, Estimation, and Modulation Theory, Part IV, Optimum array processing*. New York, NY: Wiley, 2002.
- [69] D.H. Johnson and D.E. Dudgeon, *Array Signal Processing: Concepts and Techniques*. Englewood Cliffs, NJ: Prentice-Hall, 1993.
- [70] Z. Wang, J. Li, and R. Wu, "Time-delay- and time-reversal-based robust Capon beamformers for ultrasound imaging," *IEEE Transactions on Medical Imaging*, vol. 24, pp. 1308-1322, 2005.
- [71] J.-F. Synnevåg, A. Austeng, and S. Holm, "Adaptive beamforming applied to medical ultrasound imaging," *IEEE Transactions on Ultrasonics, Ferroelectrics, and Frequency Control*, vol. 54, no. 8, pp. 1606-1613, 2007.
- [72] J.-F. Synnevåg, A. Austeng, and S. Holm, "Benefits of minimum-variance beamforming in medical ultrasound imaging," *IEEE Transactions on Ultrasonics, Ferroelectrics, and Frequency Control*, vol. 56, no. 9, pp. 1868-1979, 2009.
- [73] F. Vignon and M.R. Burcher, "Capon beamforming in medical ultrasound imaging with focused beams," *IEEE Transactions on Ultrasonics, Ferroelectrics, and Frequency Control*, vol. 55, no. 3, pp. 619-628, 2008.
- [74] F. Lingvall and T. Olofsson, "On time-domain model-based ultrasonic array imaging," *IEEE Transactions on Ultrasonics, Ferroelectrics, and Frequency Control*, vol. 54, no. 8, pp. 1623-1633, 2007.
- [75] R. Lavarello, F. Kamalabadi, and W. D. O'Brien Jr., "A regularized inverse approach to ultrasonic pulse-echo imaging," *IEEE Transactions on Medical Imaging*, vol. 25, no. 6, pp. 712-722, 2006.
- [76] J. Li and P. Stoica, *Robust Adaptive Beamforming*. Hoboken, NJ: Wiley-Interscience, 2005.
- [77] D.A. Guenther and W.F. Walker, "Robust finite impulse response beamforming applied to medical ultrasound," *IEEE Transactions on Ultrasonics, Ferroelectrics, and Frequency Control*, vol. 56, no. 6, pp. 1168-1188, 2009.

- [78] J. Capon, "High-resolution frequency-wavenumber spectrum analysis" in *Proceedings of the IEEE*, vol. 57, no. 8 pp. 1408-1418, 1969.
- [79] B. Hajek, *An exploration of random processes for engineers*. Class notes for ECE 534, Department of Electrical and Computer Engineering, University of Illinois at Urbana-Champaign, Spring 2006.
- [80] C.-I. C. Nilsen and S. Holm, "Wiener beamforming and the coherence factor in ultrasound imaging," *IEEE Transactions on Ultrasonics, Ferroelectrics, and Frequency Control*, vol. 57, no. 6, pp. 1329-1346, 2010.
- [81] O.L. Frost, III, "An algorithm for linearly constrained adaptive array processing" in *Proceedings of the IEEE*, vol. 60, no. 8 pp. 926-935, 1972.
- [82] K. Gerlach, "Convergence rate of an SMI canceler in nonstationary noise," *IEEE Transactions on Aerospace and Electronic Systems*, vol. 30, no. 2, pp. 599-604, 1994.
- [83] M.W. Ganz, R.L. Moses, and S.L. Wilson, "Convergence of the SMI and the diagonally loaded SMI algorithms with weak interference," *IEEE Transactions on Antennas and Propagation*, vol. 38, no. 3, pp. 394-399, 1990.
- [84] Y. Bresler, S. Basu, and C. Couvreur, *Hilbert spaces and least squares methods for signal processing*. Class notes for ECE 513, Department of Electrical and Computer Engineering, University of Illinois at Urbana-Champaign, Spring 2008.
- [85] S.W. Smith, H. Lopez, and W.J. Bondine Jr., "Frequency independent ultrasound contrast-detail analysis," *Ultrasound in Medicine and Biology*, vol. 11, no. 3, pp. 467-477, 1985.
- [86] A.C. Kak and M. Slaney, *Principles of Computerized Tomographic Imaging*. Philadelphia, PA:SIAM, 1999.
- [87] A.H. Andersen, "Algebraic reconstruction in CT from limited views," *IEEE Transactions on Medical Imaging*, vol. 8, no. 1, pp. 50-55, 1989.
- [88] R. Gordon, R. Bender, and G.T. Herman, "Algebraic reconstruction techniques (ART) for three-dimensional electron microscopy and X-ray photography," *Journal of Theoretical Biology*, vol. 29, no. 3, pp. 471-481, 1970.
- [89] B.E. Oppenheim, "Reconstruction tomography from incomplete projections," in *Reconstruction Tomography in Diagnostic Radiology and Nuclear Medicine*, M.M. Ter-Pogossia *et al.* Eds. Baltimore, MD: University Park Press, 1977.
- [90] G.T. Herman, *Image Reconstruction from Projections: The Fundamentals of Computerized Tomography*, New York: Academic, 1980.
- [91] M. Nassi, W.R. Brody, B.P. Medoff, and A. Macovski, "Iterative reconstruction-reprojection: An algorithm for limited data cardiac-computed tomography," *IEEE Transactions on Biomedical Engineering*, vol. BME-29, no. 5, pp. 333-341, 1982.

- [92] B.P. Medoff, W.R. Brody, M. Nassi, and A. Macovski, "Iterative convolution back-projection algorithms for image reconstruction from limited data," *Journal of the Optical Society of America A*, vol. 73, no. 11, pp. 1493-1500, 1983.
- [93] J.H. Kim, K.Y. Kwak, S.B. Park, and Z.H. Cho, "Projection space iteration reconstruction-reprojection," *IEEE Transactions on Medical Imaging*, vol. MI-4, no. 3, pp. 139-143, 1985.
- [94] R.K. Mallik, "On multivariate Rayleigh and exponential distributions," *IEEE Transactions on Information Theory*, vol. 49, no. 6, pp. 1499-1515, 2003.
- [95] M.P. Eckstein, A.J. Ahumada, and A.B. Watson, "Visual signal detection in structured backgrounds, II. Effect of contrast gain control, background variations and white noise," *Journal of the Optical Society of America A*, vol. 14, no. 9, pp. 2406-2419, 1997.
- [96] A.E. Burgess and B. Colborne, "Visual signal detection. IV. Observer inconsistency," *Journal of the Optical Society of America A*, vol. 5, no. 4, pp. 617-627, 1988.
- [97] A.E. Burgess and H. Ghandeharian, "Visual signal detection. II. Signal-location identification," *Journal of the Optical Society of America A*, vol. 1, no. 8, pp. 906-910, 1984.
- [98] D.G. Pelli, "Uncertainty explains many aspects of visual contrast detection and discrimination," *Journal of the Optical Society of America A*, vol. 2, no. 9, pp. 1508-1532, 1985.
- [99] H. Hotelling, "The generalization of student's ratio," *The Annals of Mathematical Statistics*, vol. 2, no. 3, pp. 360-378, 1931.
- [100] R.D. Fiete, H.H. Barrett, and K.J. Myers "Hotelling trace criterion and its correlation with human observer performance," *Journal of the Optical Society of America A*, vol. 4, no. 5, pp. 945-953, 1987.